**Department of Physics and Astronomy**

**University of Heidelberg**

Master's thesis

in Physics

2017

submitted by

Tanja B. C. Behrle

born in Friedrichshafen

# Simulation and Measurements of Single and Coupled Coaxial Qubits

This Master's thesis has been carried out by

**Tanja B. C. Behrle**

at the

Clarendon Laboratory, **University of Oxford**

under the supervision of

Prof. Fred Jendrzejewski (University of Heidelberg)

and

Dr. Peter Leek (University of Oxford)

**Simulation and Measurements of Single and Coupled Coaxial Qubits**

Superconducting circuits are promising candidates to serve as a platform for the development of quantum computing. A new coaxial circuit QED architecture, the coaxmon, is presented in which qubit and resonator are fabricated on opposing sides of a single chip while control and readout wiring are provided by coaxial wiring running perpendicular to the chip plane. This thesis focuses on the simulation of these devices with the aim of estimating all important qubit and resonator parameters such as frequency, lifetime, anharmonicity and coupling strength. Two different simulation approaches are used. The first method is using the finite element solver High Frequency Structure Simulator (HFSS) in combination with the black-box quantization theory (Nigg et al. [2012]). Alternatively, the Hamiltonian can be derived from the lumped element model of the circuit. Good agreement with the experiment is achieved in both cases, hence demonstrating that optimisation of the device can be achieved at the design stage. This results in the fabrication of a single coaxmon, which experimental characterisation is published in (Rahamim et al. [2017]). Finally, exploiting these techniques allows to propose the design of the first two-qubit device with the desired qubit-qubit coupling to enable the Cross-Resonance gate. In this thesis, the experimental characterisation of the very first coupled coaxmons is presented and discussed showing a promising future for the coaxmon architecture.

**Simulation und Messung einzelner und gekoppelter coaxialer Qubits**

Supraleitende Schaltkreise sind vielversprechende Kandidaten zur Entwicklung von Quantencomputern. Eine neue koaxiale Schaltkreis-Quantenelektrodynamik Architektur, das Coaxmon, wird vorgestellt. In dieser werden Qubit und Resonator auf den zwei gegenüberliegenden Seiten eines Saphir-Chips aufgebaut. Die Kontroll- und Ausleseanschlüsse werden durch Koaxialkabel senkrecht zum Chip realisiert. Der Schwerpunkt dieser Arbeit liegt auf der Simulation dieser Schaltungen, mit dem Ziel alle wichtigen Qubit- sowie Resonatoreigenschaften wie Frequenz, Lebensdauer, Anharmonizität und Kopplungsstärke vorherzusagen. Für die Simulation werden zwei Ansätze verfolgt. Dem ersten Anstatz liegt die Finite-Elemente Software für Hochfrequenzen in Kombination mit der Black-Box Quantisierung nach (Nigg et al. [2012]) zu Grunde. Im zweiten Fall wird der Hamiltonian für die elektrische Schaltung unter Annahme konzentrierter Schaltelemente berechnet. Die Ergebnisse beider Simulationen zeigen gute Übereinstimmung mit den experimentellen Messungen, sodass diese bereits in der Designphase eine Optimierung des Coaxmons ermöglichen. Dies erlaubt die Herstellung eines Coaxmons, dessen experimentelle Charakterisierung in (Rahamim et al. [2017]) beschrieben ist. Außerdem erlauben die Simulationen den Entwurf des ersten zwei-Qubit Elements dieser Bauart, wobei die Qubit-Qubit Kopplung für das Cross-Resonance Gatter ausgelegt wird. Die experimentellen Messungen des ersten gekoppelten Coaxmons werden beschrieben und diskutiert. Sie zeigen die vielversprechende Eignung der Coaxmon-Architektur für künftige Anwendungen in Quantencomputern.

# Contents


**1 Introduction** **1**

**2 Motivation** **5**
2.1 Motivating the Coaxmon . . . . . 5
2.2 State of the Art: Superconducting Qubits . . . . . 7

**3 Superconducting Qubit Theory** **11**
3.1 Quantum Bits . . . . . 11
3.2 The Josephson Junction . . . . . 13
3.3 The Cooper Pair Box . . . . . 14
3.4 The Transmon . . . . . 15
3.5 Noise and Decoherence . . . . . 16
3.6 Circuit QED . . . . . 17
3.7 Black-Box Quantisation Theory . . . . . 18
3.7.1 Single Junction Device . . . . . 18
3.7.2 Multi-Junction Device . . . . . 22

**4 Optimising the Single Coaxmon** **25**
4.1 The Coaxmon Design . . . . . 25
4.2 The Coaxmon Electric Circuit . . . . . 27
4.3 Simulating the Coaxmon . . . . . 28
4.3.1 Ansys Electronics Desktop . . . . . 29
4.3.2 The Coaxmon Design in Ansys . . . . . 30
4.4 Derivation of the Qubit Properties . . . . . 35
4.5 Variation of the Design . . . . . 36
4.5.1 Resonator Width . . . . . 37
4.5.2 Resonator Length . . . . . 38
4.5.3 Control Pin Distance . . . . . 39
4.5.4 Sample Holder . . . . . 42
4.6 Quantifying the Simulation Error . . . . . 43
4.7 The Lumped Element Model . . . . . 46
4.8 The Network Analysis . . . . . 48
4.9 Comparison to Experiment . . . . . 50

**5 Design and Simulation of Two Coupled Coaxmons** **53**
5.1 Two Qubit Gate Theory . . . 53
5.1.1 MAP Gate . . . 54
5.1.2 Cross-Resonance Gate . . . 55
5.2 Simulation of the Cross-Resonance Gate . . . 57
5.2.1 The Master Equation . . . 58
5.2.2 The CR Gate Hamiltonian . . . 59
5.2.3 Gate Simulation Results . . . 60
5.2.4 Optimising the Gate Fidelity . . . 66
5.3 The Coupled Coaxmon Design . . . 66
5.3.1 The Lumped Element Model for the Coupled Coaxmon . . . 68
5.3.2 The Qubit-Qubit Coupling Strength . . . 69
5.4 Selectivity . . . 69

**6 Experiments on the Coupled Coaxmons** **71**
6.1 Fabrication . . . 71
6.2 The Measurement Setup . . . 73
6.3 Basic Characterisation of the Coupled Coaxmons . . . 74
6.4 Qubit-Qubit Coupling Strength . . . 82
6.4.1 Measurements . . . 82
6.4.2 Comparison to Simulation . . . 83
6.5 Selectivity . . . 84
6.5.1 The Experiment . . . 85
6.5.2 Comparison to Simulation . . . 87
6.6 Conclusion on the Experiments . . . 87

**7 Conclusion and Outlook** **89**

**Appendix: Publication** **95**

**Lists** **101**
List of Figures . . . 101
List of Tables . . . 103

**Bibliography** **105**

**Deposition** **111**

# 1 Introduction

> Nature isn't classical, dammit, and if you want to make a simulation of nature, you'd better make it quantum mechanical, and by golly it's a wonderful problem, because it doesn't look so easy.
>
> *Simulating Physics with Computers*
> *Richard P. Feynman*

Superconducting circuits are well established as a strong candidate to build a quantum computer. In the last few years, superconducting quantum bits (qubits) have advanced to systems consisting of five to ten qubits operating at high enough fidelities for quantum computing. Several research groups are working hard to improve on different architectures and their performances. In April 2017, John Martinis announced that his group working on superconducting quantum bits would achieve quantum supremacy by the end of the year. This means that these devices will be able to perform calculations that are impossible on a classical computer in reasonable time. This would be a milestone in the field of quantum computing which was initiated at the end of the $20^{th}$ century by physicists such as Charles H. Bennet from IBM, Paul A. Bienoff of Argonne National Laboratory in Illinois, David Deutsch of the University of Oxford and Richard Feynman of the California Institue of Technology (see Feynman [1982]). At that time, (Shor [1999]) discovered that quantum algorithms can solve certain problems exponentially faster than the best known classical counterpart. This potential revolution of information processing has motivated physicists to work on the realisation of quantum computing devices ever since. The prospect of high computational power as well as of the decryption of today's secure RSA (Rivest, Shamir and Adleman) keys used in finance and private security, motivates governments and industry to provide the necessary research money.

Various approaches towards quantum computing devices have been undertaken since then. The quantum mechanical counterpart of the classical bit, the qubit, is a two-state quantum system, which cannot only be zero or one but also a superposition of both. In general, there are two different approaches to realise a qubit: the use of real

atoms versus 'artificial atoms' engineered in solid-state devices. An example for real atoms are trapped ions that exploit two selected hyperfine-states as their two-level quantum bit and are controlled and manipulated by laser light and radio frequency microwave. These types of qubits so far exhibit the longest coherence times and highest gate fidelities but do not easily scale to larger systems with more than one qubit and fast switching rates because of the small dipole moment of atoms. In contrast, quantum electric circuits enable the creation of an 'artificial atom' the parameters of which can be tailored arbitrarily. The advantage of high dipole moments and consequently fast switching rates stand in contrast to smaller coherence times. Nevertheless, due to the promising scalability of these quantum circuits plus the sophisticated semi-conductor technology industry, superconducting qubits are promising candidates for quantum computing devices. The work of this thesis has been carried out on such superconducting quantum circuits.

It could be stated that the field of superconducting quantum computing started in 1999 when (Nakamura et al. [1999]) showed for the first time that a single Cooper-Pair box qubit could be coherently controlled. Five years later, in 2004, (Wallraff et al. [2004]) proved that a single photon in a resonator could be strongly coupled to a superconducting qubit. The first successful coupling of two qubits was demonstrated by (Sillanpaa et al. [2007]). Since then, many different architectures have been explored. High fidelity control and lifetimes up to a few hundreds microseconds have been realised in a single qubit device (see Ofek et al. [2016]). For future quantum computing devices, combination of scalable designs with long lifetimes and high fidelities of two or more qubit operations (also referred to as gates) is still required.

In the group of Dr. Peter Leek at the University of Oxford this challenge is tackled with a new coaxial transmon architecture, named the coaxmon, which is simple to fabricate, exploits only capacitive coupling and implements qubit control and readout entirely out of the plane of the qubit. The motivation for this design and a comparison to state of the art superconducting qubits is given in Chapter 2. In Chapter 3, basic superconducting qubit theory relevant for this thesis is explained. An introduction into quantum bits is given and the Josephson junction, the Cooper-pair box and the transmon (Koch et al.

[2007]) are presented. Furthermore, the black-box superconducting circuit quantisation (Nigg et al. [2012]) is explained in Section 3.7. Based on this theory, coaxmon simulation and estimation of the important device parameters such as qubit and resonator frequency, lifetime, anharmonicity, dispersive shift and resonator-qubit coupling are carried out.

The explicit design of the single coaxmon is then presented in Chapter 4. For the single cell, simulations with the High Frequency Structure Simulator (HFSS) are performed and all important system parameters are determined. Based on these numbers, the single coaxmon design is optimised. A second method to calculate the device parameters, the so called lumped element method, is presented afterwards. In Section 4.9, comparison of both methods to experimental data shows good agreement and the experimental results of the optimised single coaxmon are published in (Rahamim et al. [2017]). This publication can be found in the appendix.

Since the first single superconducting charge qubit (Nakamura et al. [1999]), almost two decades have passed and now many architectures have realised addressable coherent qubits. Today's challenge lies in coupling many single cells and carrying out high fidelity control on those. In Chapter 5, the focus is on the coupling of two single coaxmon cells. Different methods for performing two qubit gates are studied and their suitability for the coaxmon architecture are discussed. Two promising candidates, the Cross-Resonance (CR) gate (Chow et al. [2011]) and the microwave-activated conditional phase (MAP) gate (Chow et al. [2013]) are presented in Section 5.1. In order to fully understand the dynamics and working principle of the favoured CR gate, the gate is simulated with a Master Equation in Section 5.2. Effects of lifetimes and imperfect selectivity are studied and the CR gate time for these cases is optimised. Following this, the necessary device parameters for the favoured CR gate are determined and the double coaxmon design is accordingly adjusted in Section 5.3 using the lumped element method for the coupled coaxmons. In particular, an additional capacitance in between two single coaxmon cells is introduced. For two qubit gates the addressability of a single qubit is important; this means the ability to drive a single qubit without affecting the other. This qubit drive selectivity is calculated in Section 5.4 and the simulated selectivity for the proposed coupled coaxmon design is about 2%.

With the newly determined device parameters for the coupled coaxmon, the first coupled coaxmon was fabricated and measured. The measurements are presented in Chapter 6. At first, the coupled coaxmons are treated separately and each of them is characterised. Afterwards, their interaction is explored and coupling strength and selectivity measurements are performed and compared to simulation.

The work of this thesis suggests the exciting future of the coaxmon. Coherence times are shown to be of the order of leading superconducting qubit research groups. A summary and future prospects for the coaxmon are discussed in the final Chapter 7.

# 2 Motivation

The first successful superconducting qubit was built almost two decades ago (Nakamura et al. [1999]). Since then several different architectures have been investigated and improved. Today, the challenge lies no longer in making a single cell work but to achieve long enough qubit lifetimes and to realise high fidelity single and multi-qubit gates. In addition, the focus lies on achieving these combined with the requirement of scalability for future quantum computers with thousands of unit cells. So far, all of these requirements have been fulfilled, but not yet in the same architecture. For example, transmons in 3D cavities exhibit long lifetimes of almost $0.1\,\mathrm{ms}$ (Rigetti et al. [2012]) but are difficult to scale due to the large bulky 3D cavity itself. In contrast to that, 2D micro-fabricated devices are easier to scale to the tens of qubits, but suffer from lower coherence and wiring complexity and larger scale. Therefore, new architectures are still being investigated. In this Chapter, the coaxmon is presented as a possible new candidate architecture for quantum computing that would satisfy all requirements. Following in Section 2.2, a review of the current state of the art in superconducting qubits, that are similar to the coaxmon, is given.

## 2.1 Motivating the Coaxmon

The name 'coaxmon' is composed of two shortcuts. The first part 'coax' refers to the coaxial geometry of the circuit, whereas 'mon' corresponds to the transmon regime in which the device is set. The combination of a coaxial geometry with the advantages of the transmon regime provides various benefits as explained in the following and as illustrated in Figure 4.3. For a detailed introduction into the transmon regime (Koch et al. [2007]) please refer to Section 3.4. Here, only the properties of such a regime will be addressed.

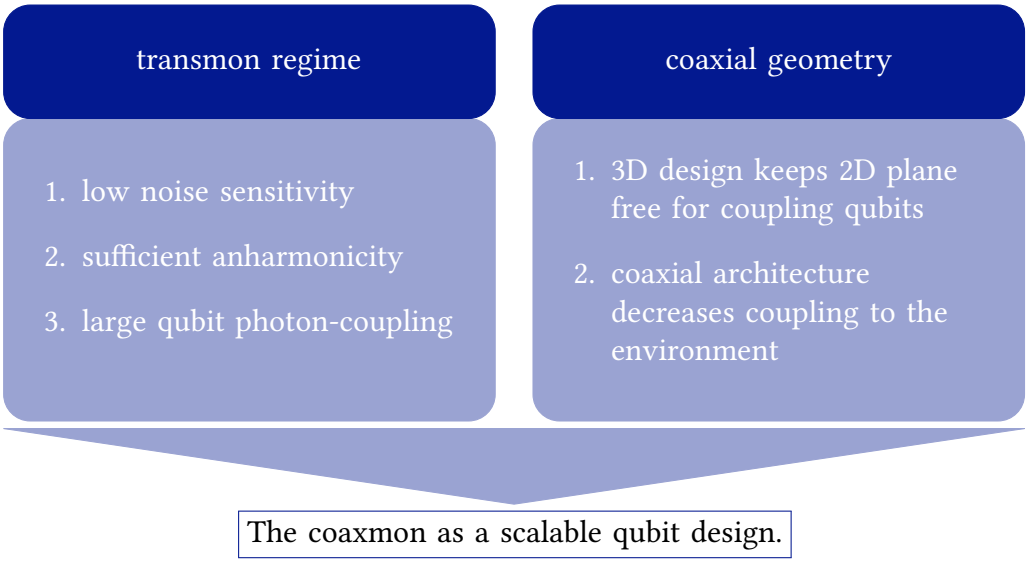


Figure 2.1: Advantages of the transmon regime and the coaxial geometry combined in the scalable coaxmon architecture.

The transmon regime offers the following advantages. First of all, very low charge noise sensitivity is provided while a sufficient anharmonicity of the energy levels is maintained to be able to address individual transitions. Furthermore, a strong qubit-photon coupling is offered by this regime. Exploiting the transmon regime already showed that lifetimes of nearly $0.1\,\mathrm{ms}$ can be achieved (Rigetti et al. [2012]). In this explicit example, the downside is the scalability of 3D cavities. The coaxial geometry of the coaxmon as follows in Chapter 4 tries to overcomethis issue.

The coaxmon, as will be explained more detailed in Section 4.1, consists of a qubit fabricated on one side of a sapphire chip with a through chip coupled resonator on the other side of the chip. With coaxial addressing pins from the top and the bottom of the chip, the resonator and the qubit are addressed in the off-plane dimension. Hence, this frees up the chip plane to use for later scaling to multi qubits since no wiring is needed here anymore. Furthermore, the qubit, the resonator as well as the addressing pins are all coaxial, hoping to reduce unwanted electromagnetic coupling to the nearby environment. At the design state of the coaxmon this only is an assumption. Nevertheless, simulation in Section 5 validate this assumption.

Finally, the coaxmon design will be fixed in frequency. No magnetic fields are intended to tune the qubit's frequency, which gives a stable platform for the new architecture. All in all, the presented architecture promises to combine important advantages to obtain a scalable qubit device.

## 2.2 State of the Art: Superconducting Qubits

This Section focuses on the qubit designs close or in competition to the coaxmon architecture. The coaxmon architecture neither is the only one making use of coaxial geometries nor the first geometry using the third dimension for readout and control. The question whether one can learn from them and which lifetime and scalability have to be achieved to keep up with the current state of the art is addressed in the following. Therefore, a summary of selected state of the art experiments on superconducting charge qubits is given below.

Coaxial geometries in superconducting qubits can be found in other qubit architectures besides the coaxmon. On one hand (Brecht et al. [2017]) present a coaxial transmon qubit coupled to a 3D micro-machined cavity as it is illustrated in Figure 2.2 (b). In this case, the advantage of large coherence times in 3D cavities is exploited but scaling requires development of a hybrid network of qubits and cavities. On the other hand in Figure 2.2 (c), (Braumüller et al. [2016]) show a 2D approach, the so-called concentric transmon qubit. The coaxial transmon qubit can be frequency tuned via a flux bias line in the qubit plane. The readout resonator is placed just next to the qubit in the same 2D plane. Even though the transmon qubit resembles the coaxmon qubit, the third off-chip plane dimension is not used in this example and therefore loses space for scalability. A coaxial cavity is implemented in (Axline et al. [2016]) and shown in Figure 2.2 (a). Multiple transmons can be coupled within the same coaxial cavity. The qubit states are read out via coupled microwave resonators and readout pins in the off-chip plane. Progress on this has already been achieved with four transmon qubits coupled to the same 3D cavity enabling implementation and characterisation of the devices (Blumoff et al. [2016]). Even though a 3D cavity is used, a multi qubit arrangement was successfully designed.

There are further scalable transmon architectures that are worth looking at. One scalable approach is a transmon placed in a multilayer whispering gallery mode resonator which couples to a neighbouring whispering gallery mode resonator above and/or below (Minev et al. [2016]). Another approach of combining a multi-qubit arrangement and 3D cavities is shown in Figure 2.2 (d) (Paik et al. [2016]). Four transmons are mounted such that they are coupled to their own readout resonator cavity as well as to one common resonator bus. This setup allows the resonator-induced phase gates to entangle multi qubits with an overall gate fidelity of $97\%$. Architectures with more than a few coupled qubits with a focus on scalability are presented in (Kelly et al. [2015]) and (Versluis et al. [2016]). In the first paper, an array of nine qubits is used to demonstrate state preservation by repetitive error detection. This demonstrates a step towards the 2D surface code scheme. In the second paper, a scalable quantum circuit and control for a superconducting surface code (Fowler et al. [2012]) is presented. Flux-tunable transmon qubits with nearest neighbour coupling are implemented and eight qubits are used to form a unit cell.

In conclusion, these examples show the many exploitable degrees of freedom in superconducting qubit architectures. However, the aim of simultaneously achieving scalability and high multi-qubit gate fidelities is difficult to reach. With the coaxmon architecture, a new idea to tackle these challenges is to come.

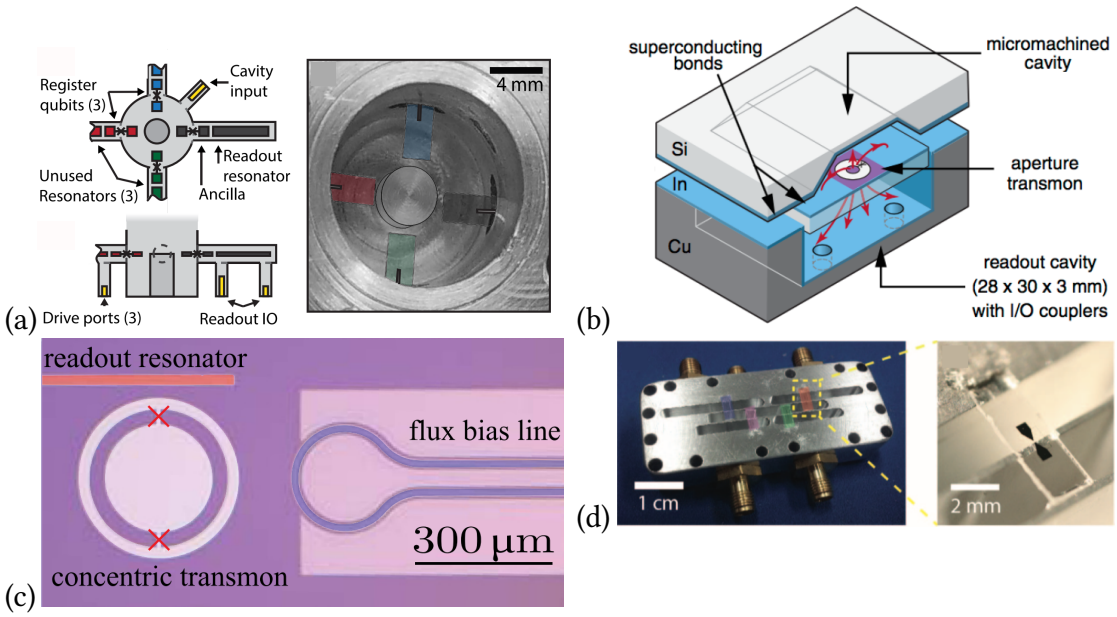


Figure 2.2: State of the art transmon architectures. (a) (Blumoff et al. [2016]) Four transmons coupled to a 3D cavity. (b) (Brecht et al. [2017]) Coaxial transmon in 3D cavity. (c) (Braumüller et al. [2016]) Concentric transmon with flux-bias line and readout resonator in plane. (d) (Paik et al. [2016]) Four transmon qubits each with its own readout cavity coupled to a common cavity in the middle.

# 3 Superconducting Qubit Theory

This Chapter introduces the necessary superconducting qubit theory required to understand this thesis. A short introduction to quantum bits, their motivation, purpose and their requirements, is given in Section 3.1. Here, it will become clear that Josephson junctions and their lossless non-linear behaviour is essential for a superconducting qubit. The physics of a Josephson junction is explained in Section 3.2. The predecessor of charge qubits is the so-called Cooper-pair box (CPB) (Nakamura et al. [1999]) and is presented in Section 3.3. A detailed insight into the transmon regime is then given in Section 3.4 followed by a general introduction into noise and decoherence in Section 3.5 and into circuit Quantum Electrodynamics (cQED) in Section 3.6. The focus of this thesis is on the simulation of the coaxmon design. In order to obtain the desired qubit and resonator parameters, the black-box quantisation theory (Nigg et al. [2012]) has to be applied to the outcomes of the simulation. Section 3.7 explains this theory in detail.

## 3.1 Quantum Bits

Quantum bits (qubits) are the quantum mechanical counterparts of classical bits. While classical bits can represent the states 0 and 1, a quantum bit can be in a superposition of both states. A pair of qubits can be in any superposition of four quantum states, three qubits in any superposition of eight quantum states. For a n qubit system, this results in a possible superposition of $2^n$ states simultaneously, compared to a classical computer, which can only store one of these states at any one point.

Quantum algorithms benefiting from quantum bits are proven to solve certain problems much faster than known algorithms on classical computers. Examples are the Deutsch

algorithm (Deutsch and Jozsa [1992]) or the Shor algorithm (Shor [1999]). Deutsch's algorithm speeds up certain problems exponentially while the Shor algorithm solves factorization of large integer numbers in polynomial time. Today's public-key cryptography is most commonly based on the RSA (Rivest, Shamir and Adleman) scheme, attributable to the problem of prime factorization problems. Keys for decryption are simply made long enough to make decryption without the key not achievable on classical computers in short time. In contrast, a working quantum computer implementing Shor's algorithm would be able to solve them in a reasonable time. However, experts argue in which time frame the quantum computer will be feasible. The current record of factorisation using Shor's algorithm was achieved in 2012 by (Martin-Lopez et al. [2012]). For the first time the number 21 was factorized. Progress in fault-tolerant quantum computing on many qubit devices is needed to achieve the next milestone. Nevertheless, there are other applications of quantum computers that are more reasonably in the near future, problems that could already benefit from small quantum computers. Simulating molecules and chemical reaction for example, which could help improving for examples batteries or electronics, see (Simonite).

The requirements of such a quantum bit device are as follows. The ideal quantum bit is an isolated two-level system without any dissipation that can be controlled and read out fast and accurately. First of all, the system should be dissipationless. A suitable candidate therefore are superconducting circuits. This automatically implies the use of superconducting materials such as aluminium. Furthermore, thermal noise should not be able to excite the qubit transitions at frequency $\omega/(2\pi)$, hence $\hbar\omega \gg k_B T$ is required. This means that for frequencies in the GHz range, temperatures of a few millikelvin are needed. Therefore, all experiments have to be performed within a dilution refrigerator well below the critical temperature for aluminium to be superconducting. Secondly, the two-level system should be isolated. In an harmonic oscillator, the energy between the ground and first excited state equals the transition energy of the first to the second excited state. This makes selectively driving one transition impossible. To avoid this, an anharmonic oscillator can be exploited as a qubit. The larger the anharmonicity, the better the isolation to further transitions. To create an anharmonic energy level structure,

a nonlinear superconducting element is needed. The only known one is the so-called Josephson junction, which will be introduced in Section 3.2. Readout of the qubit state can be realised for example via a coupled resonator. The frequency of the resonator depends on the state of the qubit allowing one to deduce the qubit's state by measuring the resonator frequency. The control of the qubit and resonator can be simply achieved by microwave control lines coupled to the qubit and resonator.

## 3.2 The Josephson Junction

A Josephson junction consists of two superconductors coupled by a weak link, for example a thin insulating barrier as illustrated in Figure 3.1. The equations exhibiting the dynamics of the Josephson junction can be derived by a simple ansatz with the coupled Schrödinger equations of the wave functions on the left and right hand side of the barrier

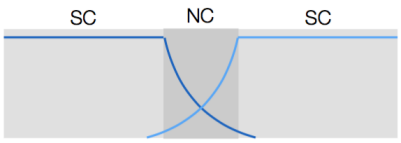


Figure 3.1: A Josephson junction consisting of a superconductor (SC) coupled by a weak non-conductor (NC) link.

$$i\hbar\frac{\partial\Psi_R}{\partial t} = \lambda_R\Psi_R + c\Psi_L, \qquad i\hbar\frac{\partial\Psi_L}{\partial t} = \lambda_L\Psi_L + c\Psi_R. \tag{3.1}$$

Here, $\Psi_{R(L)}$ is the wave function on the right (left) side, $\lambda_{R(L)}$ the eigenenergy of the wave function for the superconductors and $c$ the coupling energy of the two wave functions. With the following ansatz for the left and right wave function, the dynamics can be obtained

$$\Psi_L = \sqrt{\rho_L}e^{i\Phi_L}, \qquad \Psi_R = \sqrt{\rho_R}e^{i\Phi_R}. \tag{3.2}$$

In this case $\rho_{L(R)}$ stands for the current density on either side of the junction and $\Phi$ represents the phase difference across the junction. Plugging Equations 3.2 into the

coupled Equations 3.1, the two Josephson equations follow

$$U = \frac{\hbar}{2e}\frac{\partial \Delta\Phi}{\partial t} = \frac{\Phi_0}{2\pi}\frac{\partial \Delta\Phi}{\partial t}, \qquad I = I_C \sin(\Delta\Phi). \tag{3.3}$$

The voltage $U$ across the junction depends on the derivative of the phase difference. The current $I$ through the junction is proportional to the critical current $I_C$ and it oscillates with frequency given by the phase difference, which results in a time dependent oscillation. Solving the first Equation in 3.3 for $\Delta\Phi$ and plugging it into the current expression, the time dependent, nonlinear Josephson current relation is obtained

$$I = I_C \sin\left(\frac{2\pi U}{\Phi_0}t\right). \tag{3.4}$$

This nonlinearity allows the tailoring of an anharmonic potential suitable for a two-level quantum system, the qubit. In combination with the superconductivity and low noise at low temperatures, all requirements as discussed in Section 3.1 are fulfilled.

## 3.3 The Cooper Pair Box

The artificial two-level systems can be created in either the charge, phase or flux space. A very good introduction to the different types of qubits is given in (You and Nori [2005]). Here, the focus lies on the the Cooper-pair box (CPB), a type of charge qubit. It is the predecessor of charge qubits nowadays and based on it the transmon regime (see Section 3.4) was discovered.

The electric circuit of the CPB is sketched in Figure 3.2 (a). The CPB itself is indicated by the blue box. It is driven by the applied gate voltage $V_g$ to induce an offset charge $n_g$ through the gate capacitor with capacitance $C$. The Josephson junction is denoted by a cross through which Cooper pairs can tunnel in and out of the box. The electrostatic energy and the Hamiltonian of the CPB (You and Nori [2005]) are given by

$$\hat{H} = E_C(\hat{n} - n_g)^2 - E_J \cos\left(\hat{\Phi}\right), \tag{3.5}$$

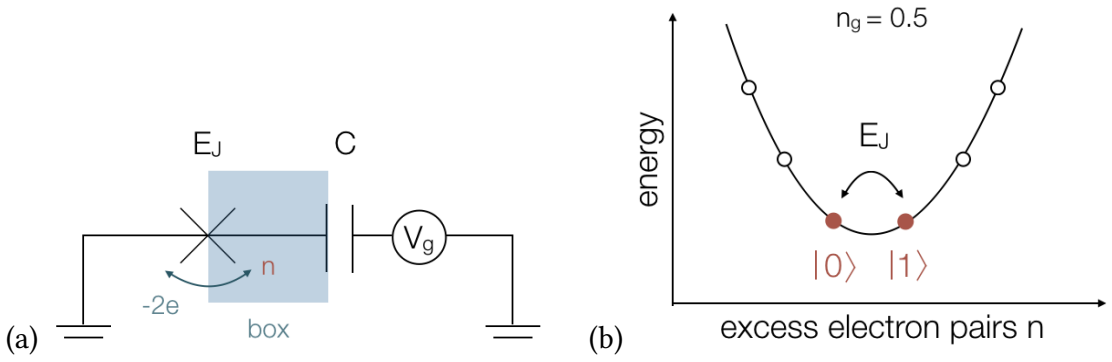


Figure 3.2: (a) The CPB is driven by the applied voltage $Vg$ to induce an offset charge $n_g$ through the gate capacitor $C$. Cooper pairs tunnel through the Josephson junction depicted as the cross. (b) The electrostatic energy diagram for $n_g = 0.5$ for which the two lowest states are degenerate. Drawings adopted from (You and Nori [2005]).

$$E = E_C(n - n_g)^2 = \frac{(2e)^2}{2C}(n - n_g)^2 \tag{3.6}$$

with the charging energy $E_C$, the Josephson energy $E_J$ and the phase difference $\Phi$ across the junction.

The energy is plotted in Figure 3.2 (b). In the case of $n_g = 0.5$, the two lowest energy states are used as the qubit states. These are coupled via the Josephson energy $E_J = \Phi_0 I_C/(2\pi)$ of the junction that controls the tunnelling between them. Here, $I_C$ stands for the critical current of the junction. The full Hamiltonian of the system is given by equation 3.5. In the low-charging regime $E_C \gg E_J$, the energy level diagram is as illustrated in Figure 3.2 (b) and the system of the lowest states can be described with the reduced Hamiltonian $\hat{H} = \epsilon(n_g)\hat{\sigma}_z - \frac{1}{2}E_J\hat{\sigma}_x$, where $\epsilon(n_g) = E_C(n_g - 1/2)$ and $\sigma_{x/z}$ are the Pauli matrices. Since $E_J$ is a property of the Josephson junction, it can be tailored with the fabrication of the junction area and hence adjusted as needed.

## 3.4 The Transmon

The transmon qubit is presented in (Koch et al. [2007]). Unlike the CPB, the transmon is designed to operate in a regime with a significantly increased ratio of Josephson energy to charging energy $E_J/E_C$. In this regime where $E_J/E_C \geq 20$, the energy levels flatten

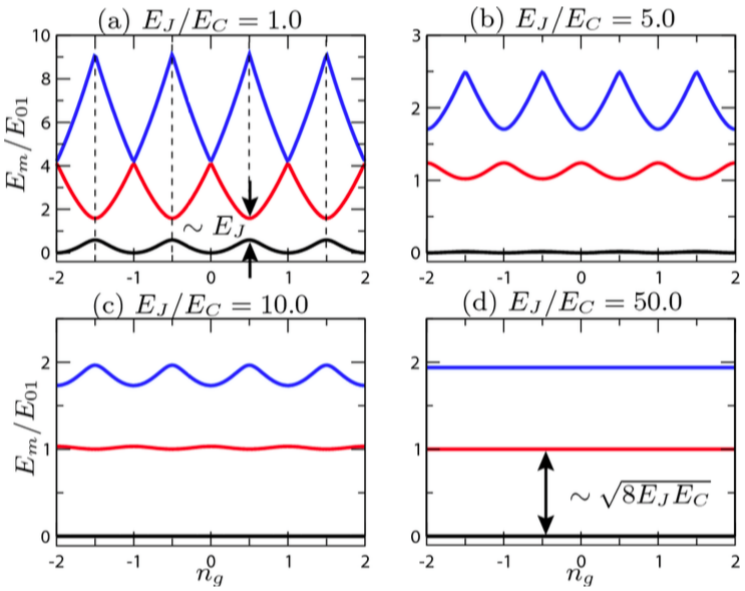


Figure 3.3: The eigenenergy as a function of the effective offset charge for different ratios of $E_J/E_C$. Large ratios lead to low noise sensitivity. Figure taken from (Koch et al. [2007]).

as illustrated in Figure 3.3 such that they become insensitive to the charge $n_g$, in contrast to the CPB. The energy level flatten exponentially but the anharmonicity only decreases with a low power law such that sufficient anharmonicity remains. The coherence time $T_2$, which is associated to the presence of noise, increases significantly in comparison to the CPB.

## 3.5 Noise and Decoherence

The qubit's lifetime is a crucial parameter allowing one to perform operations on it. In general, there are two measures of decoherence in a quantum system, $T_1$ and $T_2$. $T_1$ is the characteristic time in which the qubit decays from its first excited state to the ground state. The time $T_1$ of a qubit can be measured by initializing the qubit in the excited state and then measure the population of the excited state as a function of time. $T_2$ is the phase-coherence of the system and measures the relaxation. This $T_2$ can be measured by a Ramsey experiment. Applying two $\frac{\pi}{2}$-pulses with a time delay in

between allows one to measure the decay of the Ramsey fringes referring to the phase coherence of the system. The dephasing time $T_{\text{pure}}$ in absence of deexcitation is then given by

$$\frac{1}{T_{pure}} = \frac{1}{T_2} - \frac{1}{2T_1}, \tag{3.7}$$

as derived in (Zagoskin [2011]). This means that in general $2T_1 \geq T_2$, the relaxation time $T_2$ is limited by the decay time $T_1$.

## 3.6 Circuit QED

The physics of a two-level system coupled to an harmonic oscillator, here a resonator with frequency $\omega_r$, is described by the Jaynes-Cummings Hamiltonian (Walls and Milburn [2008])

$$\hat{H} = \hbar\omega_r \left(\hat{a}^\dagger \hat{a} + \frac{1}{2}\right) + \frac{\hbar}{2}\omega_{01}\hat{\sigma}_z + g\hbar\left(\hat{a}^\dagger\hat{\sigma}^- + \hat{a}\hat{\sigma}^+\right) \tag{3.8}$$

with the qubit-resonator coupling strength $g$. The operators $\hat{a}^\dagger$ and $\hat{a}$ create and annihilate a photon in the resonator and $\hat{\sigma}^+/\hat{\sigma}^-$ excite or de-excite the qubit. The frequency $\omega_{01}$ refers to the ground to first excited state transition of the qubit and $g$ is the resonator-qubit coupling. The first term describes the resonator Hamiltonian, the second the qubit, and the third describes their interaction. In the dispersive limit, where the qubit is far detuned from the resonator $g \ll \Delta = \omega_{01} - \omega_r$, the rotating wave-approximation can be applied to transfer the Hamiltonian into the rotating frame (Bianchetti et al. [2009]). The Hamiltonian then becomes

$$\hat{H}_{\text{disp}} = \hbar\left(\omega_r + \chi\hat{\sigma}_z\right)\hat{a}^\dagger\hat{a} + \frac{\hbar}{2}\left(\omega_{01} + \chi\right)\hat{\sigma}_z \qquad \text{where} \qquad \chi = \frac{g^2 E_C}{\Delta(\Delta - E_C)} \tag{3.9}$$

where $\chi$ is referred to as the dispersive shift. From this Hamiltonian it becomes clear that the resonator frequency shifts by $2\chi$ if the qubit is excited compared to the ground state since the eigenvalues of $\sigma_z$ are $\pm 1$. The same is true for the qubit's frequency as each photon in the resonator shifts the qubit's frequency by $2\chi$. This shift is essential to perform dispersive readout. By measuring the frequency of the resonator, one can deduce

the qubit's state as will be demonstarted in Section 6.3. As discussed, the transmon qubit behaves as an anharmonic oscillator. In order to treat the qubit as a two-level system, the anharmonicity $\alpha \approx -E_C$ (Koch et al. [2007]) needs to be sufficiently large compared to the linewidth of the qubit transition.

## 3.7 Black-Box Quantisation Theory

The main aim of this thesis is to simulate the single and coupled coaxmon architecture. The fabrication of superconducting qubit devices is time consuming and very expensive. Therefore, it is desirable to be able to predict all qubit parameters beforehand. The interesting parameters are the qubit and resonator frequency, the dispersive shift, the charging energy $E_J$, the Josephson energy $E_J$, the qubit-resonator coupling as well as the qubit lifetime. The architecture can be simulated with the Ansys HFSS software, a finite element solver for electric fields inside an arbitrary structure. Ansys software, as it will be introduced in Section 4.3.1, does not directly give all the interesting parameters of a system. For example, it does not inlcude any quantum mechanics responsible for the nonlinear behaviour of the Josephson junction, the key element of a superconducting qubit. Therefore, solutions of the simulation software have to be post-processed to give the user the parameters of interest. Specifically, quantisation has to be manually introduced. How this evaluation is performed is explained by the black-box quantisation theory published by (Nigg et al. [2012]). In this Section this theory is explained following closely this mentioned paper. For simplicity, the single junction case is treated first in order to apply it to a single coaxmon. In Section 3.7.2, the multi-junction case is introduced with focus on the application on two coupled qubits.

### 3.7.1 Single Junction Device

In the single junction case one Josephson junction is in parallel to a linear electric environment consisting of arbitrary linear circuit elements. With the junction denoted

as a red cross, this circuit is shown in Figure 3.4 (a). Note that in the following any dissipation is neglected. In this case, the physics of this system is described by Equation 3.5. In the transmon regime at $E_J \gg E_C$, the fluctuation in phase $\Phi$ is small compared to $\pi$. Therefore, it is reasonable to expand around $\Phi$ such that the circuit is approximately represented as shown in 3.2 b) with the linear junction inductance $L_J = \Phi_0^2/E_J$, the junction capacitance $C_J = e^2/(2E_C)$ and with the reduced flux quantum $\Phi_0 = \hbar/(2e)$. The energy associated to the nonlinear component of the junction is given by $E_{nl} = -\Phi_0^2\phi^4/(24L_J)$ and is illustrated as the red spider symbol. All linear parts of the junction can now be combined with the environment. They are then represented by the impedance at the junction as shown in Figure 3.4 (c). According to Forster's theorem, the equivalent circuit can be constructed from a series of parallel LRC-circuits as illustrated in Figure 3.4 (d). The total impedance is given by

$$Z(\omega) = \sum_{p=1}^{M} \left( j\omega C_p + \frac{1}{j\omega L_p} + \frac{1}{R_p} \right)^{-1} \tag{3.10}$$

where M is the number of modes. The resonance frequencies of these linear modes are the real parts of the poles of $Z(\omega)$. Alternatively, since $Y(\omega) = 1/Z(\omega)$, the modes are given by the real part of the zeros of the linear admittance spectrum. The total admittance spectrum is the sum of the admittance of the environment and the junction admittance

$$Y(\omega) = Y_E(\omega) + Y_{JJ}(\omega) \tag{3.11}$$

where the linearised admittance of the junction is given by $Y_{JJ} = j\omega C_J + 1/(j\omega L_J)$. Note that this will become important for the following evaluation of the admittance spectrum given by HFSS. In the software, the admittance from the point of view of the junction will only include the admittance of the environment $Y_E$. This means, the linearised admittance of the junction has to be added manually before calculating further properties using the total admittance $Y(\omega)$.

For weak dissipation $R_p \gg \sqrt{L_p/C_p}$, it can be shown (Spring [2016]) that the frequency of mode $p$ is given by $\omega_p = (L_pC_p)^{-1/2}$, the resistance by $R_p = 1/\mathrm{Re}Y(\omega_p)$ and the

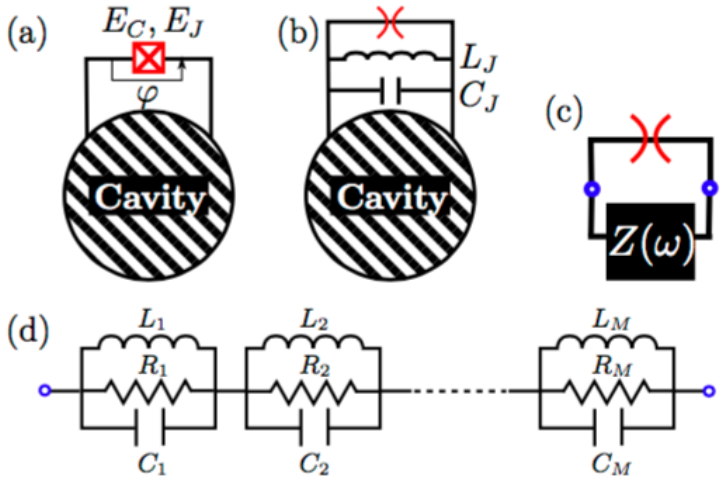


Figure 3.4: The black-box quantisation model. (a) A Josephson junction coupled to a linear environment can be split up (b) into its linear junction inductance and junction capacitance and its nonlinear part here in red. (c) The environment combined with the linear parts of the junction is represented by the impedance $Z(\omega)$. According to Foster's theorem, the impedance has an equivalent circuit consisting of many coupled LCR-circuits. Figure taken from (Nigg et al. [2012]).

capacitance by $C_p = (1/2)\mathrm{Im}Y'(\omega_p)$. Here and in the following, all primes stand for the derivative with respect to the frequency $\omega$. With these, one can now determine the quality factor of each mode, which is given by

$$Q = \omega \frac{\text{Energy stored}}{\text{Power loss}}. \tag{3.12}$$

The energy stored in a parallel LC-circuit is $CV^2$ with an averaged squared voltage, and there is no power loss in the ideal case. In contrast to this, the resistor has an average power loss of $V^2/R$ and it does not store energy. With use of the approximation of weak dissipation the quality factor of the modes can be calculated:

$$Q_p = \frac{\omega_p}{2} \frac{\mathrm{Im}Y'(\omega_p)}{\mathrm{Re}Y(\omega_p)}. \tag{3.13}$$

Following from that, the lifetime of mode $p$ is given by

$$T_p = \frac{Q_p}{\omega_p} = \frac{1}{2}\frac{\mathrm{Im}Y'(\omega_p)}{\mathrm{Re}Y(\omega_p)}. \tag{3.14}$$

This gives an estimate for the Purcell limited lifetime $T_p$ (the lifetime due to spontaneous emission into the electromagnetic environment) of the mode $p$ since the environment with the resonator is included in the admittance spectrum.

Note that until now the treatment was purely classical and nonetheless the frequencies of the modes and their quality factor or lifetime could be estimated. To proceed further and to obtain desired values for the anharmonicity $\alpha$ and the dispersive shift $\chi$, the system has to be quantised. First, the circuit is assumed to be dissipationless, meaning $R_p \to \infty$. Then, the classical Hamiltonian of Equation 3.5 is quantised in the canonical way. The Hamiltonian including the Josephson junction is given by $\hat{H} = \hat{H}_0 + \hat{H}_{nl}$ where $\hat{H}_0 = \sum_p \hbar\omega_p \hat{a}_p^\dagger \hat{a}_p$ is the Hamiltonian of the harmonic oscillators and $\hat{H}_{nl}$ is the nonlinear part of the Josephson junction. Treating this nonlinear contribution as a perturbation leads to the anharmonic Hamiltonian of the system

$$\hat{H} = \hat{H}_0' + \frac{1}{2}\sum_{pp'} \chi_{pp'} \hat{n}_p \hat{n}_{p'} \tag{3.15}$$

where $\hat{n}_p = \hat{a}_p^\dagger \hat{a}_p$ is the bosonic number operator and $\hat{H}_0' = \hat{H}_0 + \sum_p \Delta_p \hat{n}_p$ is the unperturbed Hamiltonian $H_0$ plus a the Lamb shift $\Delta_p$ given by

$$\Delta_p = \frac{-e^2}{2L_J}\left[\frac{2}{\omega_p \mathrm{Im}Y'(\omega_p)}\sum_q \frac{2}{\omega_q \mathrm{Im}Y'(\omega_q)} - \frac{2}{\omega_p \mathrm{Im}Y'(\omega_p)^2}\right]. \tag{3.16}$$

Here, $L_J$ is the junction inductance and $\chi_{pp'}$ is the generalised $\chi$-shift between the modes $p$ and $p'$. For example, $\chi_{pp'}$=$\chi_{p'p}$ with $p \neq p'$ is the so called cross-Kerr shift of mode $p$ due to a single excitation in mode $p'$. In circuit QED, the $\chi$-shift often refers to the shift of the resonator (mode $p$) due to an excited qubit (mode $p'$) as it was already introduced in Section 3.6. For $p = p'$, $\chi_{pp}$ is the self-Kerr shift representing the anharmonicity $\alpha \equiv \chi_{pp}$.

The self- and cross-Kerr shift are given by

$$\chi_{pp'} = -2\sqrt{\chi_{pp}\chi_{p'p'}} \quad \text{and} \quad \chi_{pp} = -\frac{L_p}{L_J}\frac{C_J}{C_p}E_C. \tag{3.17}$$

And $\chi_{pp}$ can be written as

$$\chi_{pp} = -8\left[\frac{e^2}{\hbar\omega_p \mathrm{Im}Y'(\omega_p)}\right]^2 E_J. \tag{3.18}$$

From Equation 3.15, the Lamb shifted resonator and qubit frequencies can be determined. For each mode, its frequency is given by

$$hf_p = \hbar\omega_p + \Delta_p + \frac{\chi_{pp}}{2} \tag{3.19}$$

with the Lamb shift $\Delta_p$. For a complete description of the qubit-resonator system one needs to estimate the coupling strength g between both elements. As derived in (Bianchetti et al. [2009]), this coupling can be calculated as

$$g = \sqrt{\frac{-\chi\Delta(\Delta+\alpha)}{-\alpha}}, \tag{3.20}$$

where $\Delta = \omega_{01} - \omega_r$ is the qubit-resonator detuning, $\alpha = \chi_{pp}$ and $\chi = \chi_{qr}/\hbar$. This allows estimation of $g$ from the results of the simulation.

At this point, the necessary theoretical background knowledge is given to simulate a single coaxmon device. Solving the fields and knowing the admittance spectrum from the point of view of the junction combined with the just described black-box quantisation theory allows one to fully characterise any qubit-resonator system before fabrication.

### 3.7.2 Multi-Junction Device

As a next step, the theory is generalised for a multiple junction case as it is desired to simulate multi-qubits as well. The necessary black-box quantisation theory is also described in (Nigg et al. [2012]). In the general case for $n$ qubits, in lowest order perturbation and

in approximation of $\Phi^4$, the anharmonicity, self- and cross-Kerr shift are found to be

$$\chi_{qp} = -24\beta_{qqpp'} \quad \text{for } q \neq p, \text{ and} \quad \alpha_p = -12\beta_{pppp} \tag{3.21}$$

with the Lamb-shift $\Delta_p = 6\beta_{pppp} - 12\sum_q \beta_{qqpp}$ where $\beta$ and $\xi$ are defined as

$$\beta_{qq'pp'} = \sum_{s=1}^{N} \frac{e^2}{24 L_J^{(s)}} \xi_{sq}\xi_{sq'}\xi_{sp}\xi_{sp'} \tag{3.22}$$

$$\xi_{sp} = \frac{Z_{s1}(\omega_p)}{Z_{11}(\omega_p)} \sqrt{Z_{1p}^{\text{eff}}} \tag{3.23}$$

and $L_J^{(s)}$ is the junction inductance of qubit $s$, $Z_{kp}^{\text{eff}} = 2/[\omega_p \text{Im} Y_k'(\omega_p)]$ and $k = 1$ is chosen as a reference port.

Narrowing down the search for a two junction case ($N = 2$) simplifies these expressions significantly. Careful rewriting leads to the cross-Kerr shift and the anharmonicity as a function of the impedance $Z(\omega)$

$$\chi_{qp} = -e^2 Z_{1p}^{\text{eff}} Z_{1q}^{\text{eff}} \left[ \frac{1}{L_J^{(1)}} + \frac{1}{L_J^{(2)}} \left( \frac{Z_{21}(\omega_q)}{Z_{11}(\omega_q)} \frac{Z_{21}(\omega_p)}{Z_{11}(\omega_p)} \right)^2 \right] \tag{3.24}$$

$$\alpha_p = -\frac{e^2}{2} \left( Z_{1p}^{\text{eff}} \right)^2 \left[ \frac{1}{L_J^{(1)}} + \frac{1}{L_J^{(2)}} \left( \frac{Z_{21}(\omega_p)}{Z_{11}(\omega_p)} \right)^4 \right]. \tag{3.25}$$

To insert the admittance spectra from simulation, it is useful to rewrite the impedance with the reactance. From $[Y] = [Z]^{-1}$ it follows that

$$Y^{-1} = \frac{1}{|Y|} \begin{bmatrix} Y_{22} & -Y_{12} \\ -Y_{21} & Y_{11} \end{bmatrix} = \begin{bmatrix} Z_{11} & Z_{12} \\ Z_{21} & Z_{22} \end{bmatrix} = Z. \tag{3.26}$$

Using this relation, Equations 3.24 and 3.25 can be rewritten as

$$\chi_{qb} = -e^2 \frac{2}{\omega_p \text{Im} Y_1'(\omega_p)} \frac{2}{\omega_q \text{Im} Y_1'(\omega_q)} \left[ \frac{1}{L_J^{(1)}} + \frac{1}{L_J^{(2)}} \left( \frac{Y_{21}(\omega_q)}{Y_{22}(\omega_q)} \frac{Y_{21}(\omega_p)}{Y_{22}(\omega_p)} \right)^2 \right] \tag{3.27}$$

$$\alpha_p = \frac{-2e^2}{(\omega_p \mathrm{Im} Y_1'(\omega_p))^2} \left[ \frac{1}{L_J^{(1)}} + \frac{1}{L_J^{(2)}} \left( \frac{Y_{21}(\omega_p)}{Y_{22}(\omega_p)} \right)^4 \right]. \tag{3.28}$$

In addition to the Lamb-shift, all necessary device parameters are then theoretically given to characterise a two qubit device from simulation. One would then be able to fully characterise the device prior to fabrication. However, simulations for a multi-qubit device exceeds the for this thesis available computation power.

# 4 Optimising the Single Coaxmon

With all necessary knowledge about qubit theory and the black-box quantisation, this Chapter introduces the single coaxmon architecture. First of all, the coaxmon design is presented in detail in Section 4.1. To better understand the working principle of the coaxmon device, the equivalent electrical circuit is explained in Section 4.2. Since the focus of this thesis is the simulation of the coaxmon device, Section 4.3.1 introduces the software 'Ansys Electronics Desktop', which is then used to simulate the coaxmon in Section 4.3.2. Following that, the derivation of all important properties is presented in Section 4.4. Section 4.5 shows how simulations allow optimisation of the coaxmon parameters. Here, changes in the resonator width and length as well as changes in the pin distance, sample holder and the qubit position relative to the centre are discussed. Given all simulation results, their error and accuracy is discussed in Section 4.6. In Section 4.8, another approach besides HFSS to derive the qubit-resonator coupling, the network analysis, is described. This method will later also allow the derivation of the selectivity in a multi qubit device as well as the qubit-qubit couplings. Finally, in Section 4.9 experimental data is compared to the simulations.

## 4.1 The Coaxmon Design

The coaxmon design is shown in Figure 4.1. This illustration is taken from the Ansys HFSS simulation, which is later described in Section 4.3. Two coaxial cables are addressing either side of a C- cut sapphire chip of dimensions $(5 \times 5 \times 0.5)\mathrm{mm}^3$. The inner conductor is a copper pin (brown) and the outer conductor is the aluminium sample holder depicted in Figure 4.4 (a). The micro-machined aluminium sample holder has a recess for the chip and a hollow is machines such that the pins do not touch it. The coaxmon itself consists

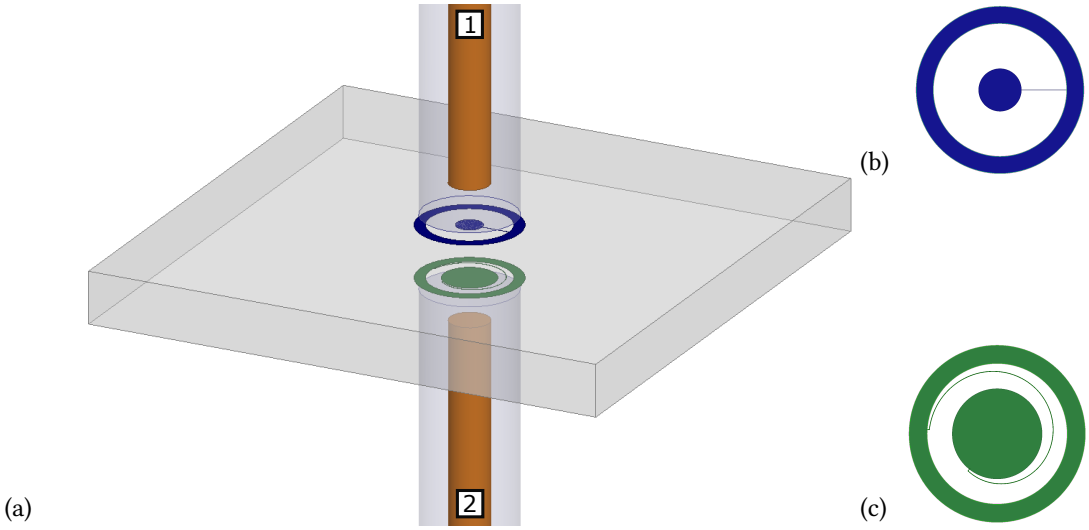


Figure 4.1: (a) Single coaxmon design. Illustration taken from the HFSS simulation. Two copper pins (brown) address the qubit (blue) at the top of the sapphire chip (grey) and the LC resonator (green) at the bottom. Aluminium sample holder not shown here. The Figure is drawn to scale, with a square sapphire chip of $(5 \times 5 \times 0.5)\mathrm{mm}^3$. (b) The qubit consists of a capacitively coupled inner and outer aluminium island which are connected through a thin line including a Josephson junction in the middle. (c) The resonator is formed by capacitively coupled inner and outer islands connected by an inductor spiral.

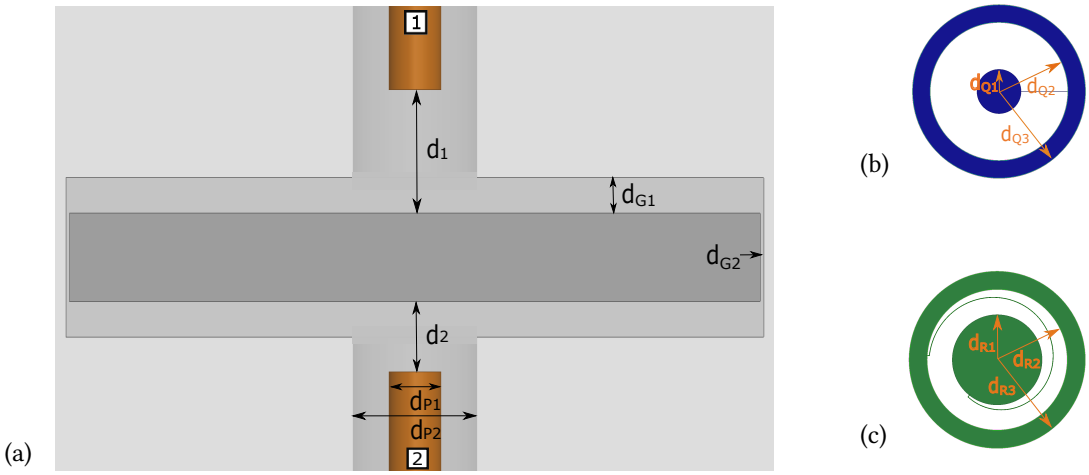


Figure 4.2: The single coaxmon dimensions. (a) The sapphire chip (dark grey) in the sample holder. View from the side. Line 1 refers to the qubit pin and line 2 to the resonator pin. The distance of each pin to the qubit and resonator is $d_1$ and $d_2$ respectively. The distance $d_{G1}$ is the distance between chip and sample holder at the top and bottwom, $d_{G2}$ refers to the distance between chip and sample holder at the sides. $d_{P1}$ and $d_{P2}$ are the thicknesses of the copper pin and its hollow. (b) The qubit dimensions. (c) The resonator dimensions. All values after optimisation are listed in Table 4.1.

of a transmon qubit (blue) on one side of the chip and the resonator (green) fabricated on the opposite side of the chip. The qubit is built out of two capacitively coupled 80nm thick aluminium islands, which are connected by a Josephson junction. The qubit is fabricated on top of the chip. The LC-resonator is fabricated on the opposite side of the chip coaxially aligned to the qubit. As for the qubit, the capacitance is realised by the two island pads and the thin spiral forms the inductance of the resonator. All elements are coupled capacitively with each other. A simplified electric circuit is given in Section 4.2. The single coaxmon device parameters as they result after optimisation described in Section 4.5 are given in Table 4.1. To emphasise the motivation and novelty of this architecture, one has to revisit the geometrical advantage of this architecture: addressing the qubit and resonator from either side of the chip without the need of wiring frees up the 2D plane around the qubit for future coupling to other qubits in multi qubit devices. Exploitation of this advantage in coupling two coaxmons was achieved for the first time within this project, see Chapter 5.

The aimed parameters for the single coaxmon follow the common range of 2D circuit QED architectures. This means, that the qubit-resonator detuning $\Delta$ and the qubit-resonator coupling $g$ are chosen such that the dispersive limit $g \ll \Delta$ is satisfied, but the resulting $\chi$-shift (Equation 3.9) remains big enough to allow dispersive readout as later shown in Section 6.3. Furthermore, to be in the transmon regime, the target value for the ratio of Josephson energy $E_J$ and charging energy $E_C$ is $50 - 100$. A common value for the anharmonicity $\alpha$ is about $300\,\mathrm{MHz}$. Due to a $8\,\mathrm{GHz}$ to $12\,\mathrm{GHz}$ band pass filter on the output line in the experiment setup (see Section 6.2), resonator frequencies are aimed to be within this range. The qubit frequency is chosen to be smaller than the resonator frequency such that the higher levels of the qubit have even smaller frequency transitions and do not interfere with the resonator.

## 4.2 The Coaxmon Electric Circuit

In order to better understand the coaxmon architecture it is useful to look at the effective electric circuit shown in Figure 4.3. Left to right corresponds top to bottom in Figure 4.1.

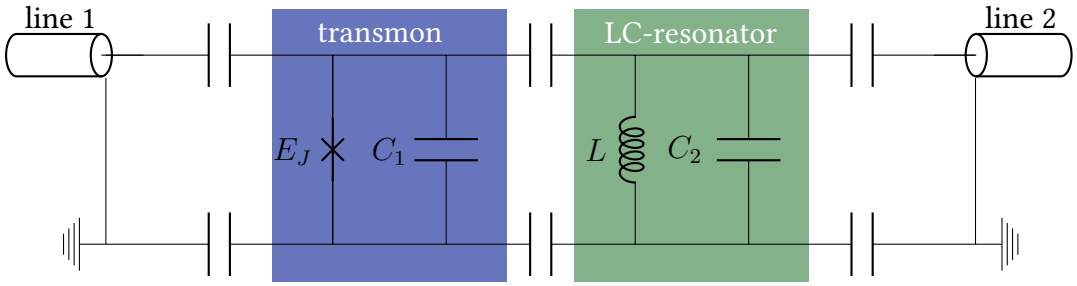


Figure 4.3: The simplified electric circuit representing the single coaxmon. The transmon qubit consists of the Josephson junction with energy $E_J$ and a capacitance $C_1$ in parallel. It is capacitively coupled to line 1, the coaxial qubit cable consisting of qubit pin and ground. The LC-resonator on the other side of the chip is capacitively coupled to the qubit and to the resonator coaxial cable, line 2.

The inner conductor of the coaxial line 1 on the left hand side is capacitively coupled to the transmon, the outer conductor represents ground. Next, the transmon consisting of a Josephson junction with energy $E_J$ and capacitance $C_J$ is in parallel to the capacitance $C_1$ between the inner and outer island of the qubit. The qubit then is capacitively coupled through the sapphire chip to the LC resonator which can be controlled by the capacitively coupled coaxial line 2. It is important to mention that this diagram shows the effective circuit. Note that not all the capacitances are drawn in order to preserve simplicity. Specifically, a capacitance between every two elements had to be drawn. In fact, there are seven potential islands resulting in a complete 7x7 capacitance matrix. Capacitances such as the input pin to resonator capacitance are not drawn but combined in the effective equivalent. In Sections 4.8 and 4.7, the complete capacitance matrix will play an important role and a simulation software is used to simulate and solve the complete circuit.

## 4.3 Simulating the Coaxmon

Since fabrication is costly and time consuming, it is desirable to simulate the presented coaxmon architecture prior to fabrication. Preferably, a device with an optimised geometry is directly fabricated. The software Ansys HFSS offers the possibility to solve for high frequency fields and for example find the admittance spectra. Given the latter, the

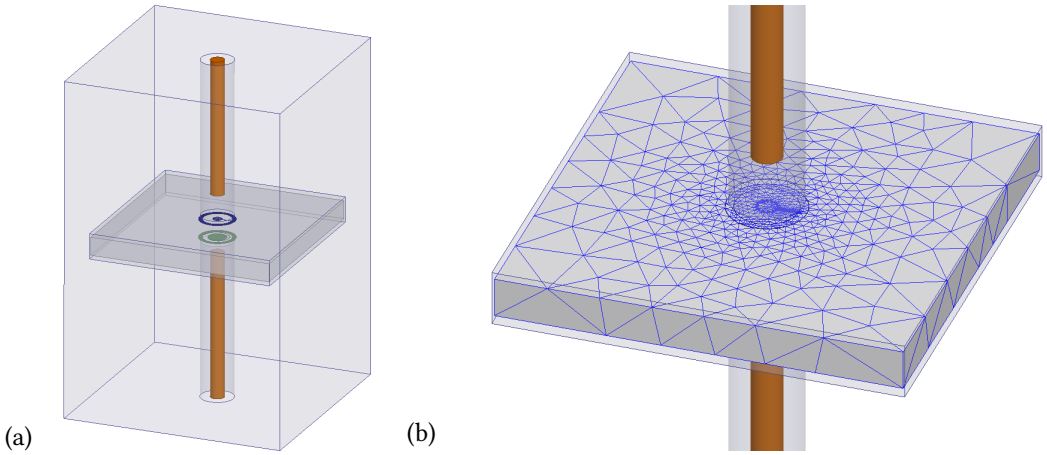


Figure 4.4: Single coaxmon. (a) Design including the sample holder. (b) Illustration of the finite mesh on the chip created with Ansys HFSS.

black box quantisation theory, presented in Section 3.7, delivers the necessary theory to calculate all desired qubit and resonator parameters. At first, the mentioned softwares Ansys HFSS and Maxwell are introduced in Section 4.3.1. Following in Section 4.3.2, it is explained how the coaxmon is constructed using Ansys. The application of the black-box quantisation onto the results from these simulations is then described in Section 4.4.

### 4.3.1 Ansys Electronics Desktop

The software Ansys Electronics Desktop enables electromagnetic analysis, circuit and system simulation. It includes a High Frequency Structure Simulator (HFSS) as well as a static solver called Maxwell for electrostatic or magneto-static problems besides other solution types. Here, we will focus on the first two. In all cases, the solver is based on the finite element method. A mesh consisting of triangles is spanned across the system and the fields are solved within each triangle. This mesh can be seen in Figure 4.4 (b). Its size is decreased stepwise until the solution converges according to manually selected convergence criteria. In the following, the solution types HFSS and Maxwell are explained in more detail. It is worth mentioning at this point that Ansys software and especially HFSS require a large amount of random access memory capacity. To perform the simulations described in this thesis, cluster capacity of up to $256\,\mathrm{GB}$ memory was necessary.

#### HFSS

The High Frequency Structure Simulator (HFSS) solves high frequency electromagnetic problems. Any arbitrary system can be constructed in the program by intuitive handling. To each object within the system a material and boundary conditions are assigned. All common elements and their electric properties are listed in a library and custom made materials can be added. Furthermore, wave ports and lumped ports allow excitations to be introduced to the system. In order to ensure all objects of different length scales are taken care of when running the simulation, mesh restrictions on selected objects can be added. Note, that this will become of importance when refining solutions. Finally, once manually chosen convergence criteria are defined, the simulation can be run. If no mesh restrictions are implemented, the first mesh size orientates itself along the entered solution frequency. The solutions of the HFSS simulations give electromagnetic fields, transmission, reflection and impedance spectra, and a lot more.

#### Maxwell

Ansys Maxwell is constructed analogously to HFSS. In contrast to HFSS, Maxwell is a static solver for either magneto-static or electrostatic problem. The design can be constructed exactly in the same way and objects can even be copied from one to the other solution type. In addition, materials and boundary conditions need to be defined. The types of excitation are different from HFSS's ones. Instead of wave ports, static current or voltage excitations can be added. Furthermore, the mesh and convergence criteria can be handled as discussed for HFSS. After a completed simulation, fields or for example the coupling capacitances between selected objects can be plotted.

### 4.3.2 The Coaxmon Design in Ansys

The coaxmon architecture constructed in Ansys is shown in Figures 4.1 and 4.4. All objects of the design, as discussed in Section 4.1, are drawn to scale by using rectangles, circles, cylinders, cubes. All important lengths are defined as variables in the setup to allow easy variation and sweeps of those quantities at a later stage.

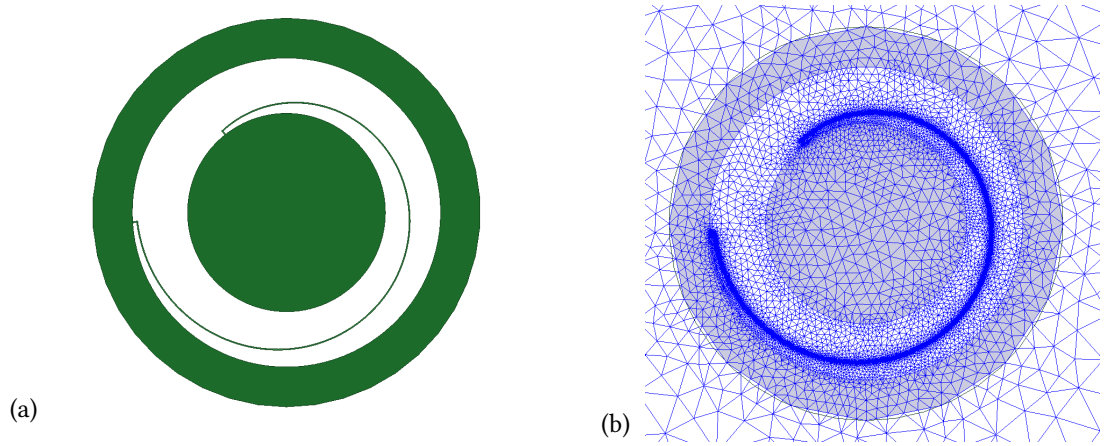

(a) (b)

Figure 4.5: Resonator (a) without and (b) with mesh. The mesh size is restricted to $1\,\mu m$ on the resonator to account for the thin inductor spiral.

### Resonator Spiral

The resonator inductor is formed by a central island connected to an outer ring by an Archimedean spiral defined as $r = a + b\theta$ with $a, b \in \mathbb{R}$ and the angle $\theta$. Here, a represents the offset from the centre and b is the spiral parameter. The spiral does not directly start at the centre island or outer ring, on both ends it is connected by a straight $10\,\mu m$ connection. A close look in Figure 4.7 (a) shows this. In the following, the length of the spiral serves as reference. The length $L$ is calculated as:

$$L(f) = \int_{\theta_1}^{\theta_2} |f'(\theta)| d\theta = \int_{\theta_1}^{\theta_2} \sqrt{(1+\theta^2)b^2} dt = \int_{r_1}^{r_2} \sqrt{(1+r^2)/b^2} dr \tag{4.1}$$

with the spiral function $f : [\theta] \to \mathbb{R}^2 \quad \text{with} \quad \theta \to (b\theta\cos\theta, b\theta\sin\theta)$ where $\theta_{1/2} = \frac{r_{1/2}}{b}$ are the start and end angles of the spiral with the start and end radius $r_{1/2}$.

### Materials

The copper pins and the vacuum parts are defined with the copper and vacuum values from Ansys library. Due to the fact that aluminium becomes a superconductor in the experiment, the aluminium pads of the qubit and resonator as well as the sample holder are assumed to be a perfect conductor in the simulation. This automatically adds perfect

conducting boundaries to these objects. In contrast to this, the sapphire system values need to be modified. First of all, the dielectric loss tangent needs to be corrected to $10^{-7}$ (Kusunoki et al. [2002]) instead of the zero found in the system library. This is important because a parameter of interest is the lifetime of the qubit that strongly depends on the electromagnetic energy loss in the whole system. Besides this, C-sapphire exhibits an anisotropic relative permittivity, which is not included in the system library. Following (The New Value Frontier [2016]) and (Antula [1967]) the relative permittivity is extrapolated to be $7.308$ for the parallel C-axis and $10.100$ for the vertical one at millikelvin temperatures. Simulation shows that the latter influences results strongly, hence should always be included.

### Wave Ports

In this design, two copper pins address the qubit and resonator from either side of the chip. As these are the wave ports, the end surface of the coaxial pins are each assigned to be a wave port. Specifically, the vacuum ring between the copper pin and the sample holder corresponding to ground is assigned. This allows looking at transmission and reflection spectra from the qubit and resonator pin.

### Lumped Port

The essential component of a superconducting qubit is the Josephson junction. However, the quantum mechanical properties of a junction cannot be modelled in a classical simulator such as Ansys HFSS. Nevertheless, as explained in Section 3.7, with the knowledge of the admittance spectrum at the Josephson junction, all characteristic qubit properties can be determined. To simulate the Josephson junction and to obtain its admittance spectrum, a lumped port is defined as follows. The gap in between the fingers reaching from the qubit inner island to the outer island is where the junction is placed in reality. In the simulation, this area is selected and declared to be a lumped element port with a resistance of $50\,\mathrm{G}\Omega$ and zero reactance. This assignment allows the user to later look at

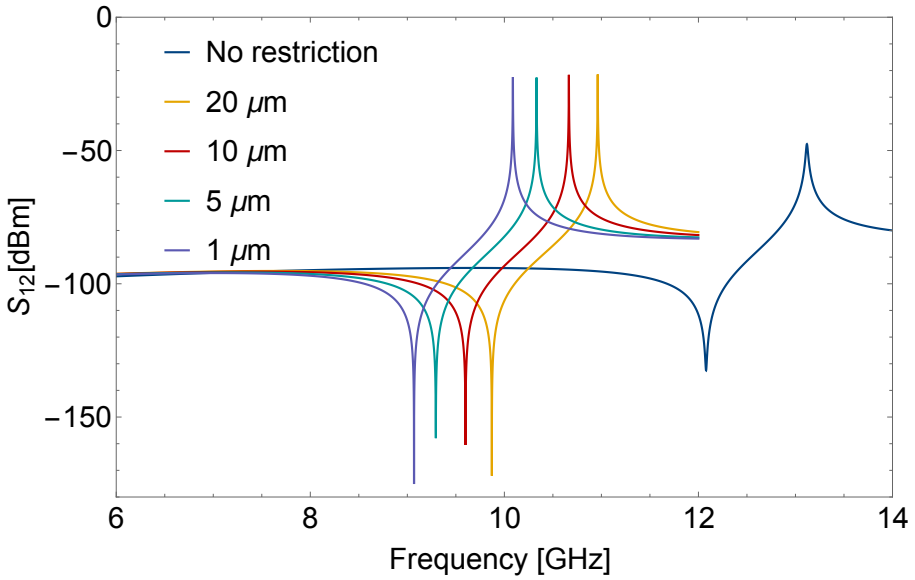


Figure 4.6: Transmission spectrum for different maximal mesh size restrictions on the resonator. The smaller the mesh, the more the transmission peak shifts towards smaller frequencies. It seems as if the peaks converges to a frequency below $10\,\mathrm{GHz}$. Due to the fact that a mesh restriction of $1\,\mu\mathrm{m}$ is the minimum, the simulated resonator frequency is bigger than in experiment for the same resonator length.

the admittance or reactance spectrum at this point, providing all necessary information to apply the black-box quantisation theory.

### The Mesh

Building the architecture with length scales of mainly millimetres automatically sets the unit of the simulation to millimetre. According to this length scale and the selected solution frequency of a simulation, the first mesh is created. The size is then reduced in every iteration step. This works well as long as no objects are much smaller than the unit length scale. However, the resonator spiral in the coaxmon architecture with a width of $1\,\mu\mathrm{m}$ to $5\,\mu\mathrm{m}$ is much smaller than most of the other features in the design. When plotting the mesh after a simulation, one soon realises that the automatic mesh is not at all taking care of the small spiral inductor. In this case, it is necessary to manually define the mesh size on the small objects. A maximal mesh size can be set and hereby

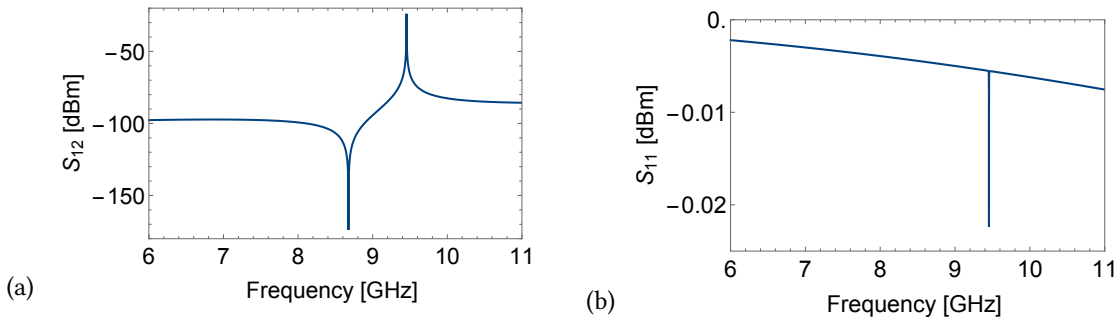


Figure 4.7: Transmission and reflection spectra. (a) Transmission spectrum from resonator pin to qubit pin. (b) Reflection spectrum at qubit pin.

the mesh cannot miss the small object anymore. For a mesh restriction to $20\,\mu\mathrm{m}$, the mesh is plotted in Figure 4.7. Furthermore, refining the mesh size in general results in a significant change of the simulation results. Figure 4.6 shows the transmission spectra for the same coaxmon but different mesh size restrictions on the resonator and qubit. The transmission frequency decreases with a smaller mesh and seems to converge. Whereas the change in frequency from no mesh restriction to $20\,\mu\mathrm{m}$ is still about $2\,\mathrm{GHz}$, it only changes a fraction of that when refining the mesh from $5\,\mu\mathrm{m}$ to $1\,\mu\mathrm{m}$. Unfortunately, even $256\,\mathrm{GB}$ memory are not sufficient to further decease the mesh size. Requesting only one converging pass, a $1\,\mu\mathrm{m}$ mesh restriction results already in $10^6$ solved elements. This is why all following simulations will be performed with this $1\,\mu\mathrm{m}$ mesh restriction. Note, that this is further discussed in Sections 4.6 and 4.9 when quantifying simulation errors and comparing results to experiment. Since the thickness of both resonator and qubit is about $80\,\mathrm{nm}$ and it is much smaller than the smallest possible mesh size, simulation shows no difference for a 2D or 2D design.

### Convergence Criteria

When adding a frequency sweep for a simulation several options are offered. First of all, the solution frequency has to be set according to which the initial size is chosen. In addition, a maximum and minimum number of passes, a minimum number of converged mesh refinement passes, a percentage mesh refinement per pass and a maximum $\Delta S$ for the solution accuracy can be set. The latter is the maximum error in the model based

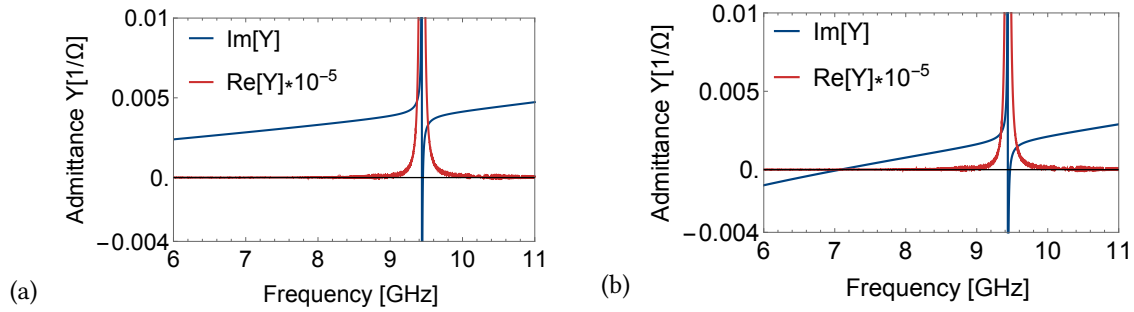


Figure 4.8: Admittance spectra at the Josephson junction. (a) From HFSS without the junction properties. Only the resonance of the resonator at about $9.5\,\mathrm{GHz}$ is evident. (b) After adding the admittance of the junction, a second zero crossing appears. This one refers to the qubit frequency.

calculated S-parameters. The smaller the $\Delta S$, the more converged passes are required and the more accurate the simulation is. But again, more costly are the simulations in terms of times and memory capacity. In this thesis for good simulation results, the solution frequency is set to the expected resonator frequency and the mesh refinement per pass is left at its default setting of 30%. A maximum number of passes of 20 and a number of converged passes of up to two and a $\Delta S$ in the range of $0.001 - 0.1$ was chosen. These convergence criteria for the coaxmon design, which showed to give reasonable results, need a RAM capacity of $32\,\mathrm{GB}$ to $256\,\mathrm{GB}$ and therefore are performed on an external cluster. Performing simulations while sweeping a parameter of interest might take two to twenty hours of calculation time. Once a simulation is finished, it should always be checked that the results are sensible. Two checks should always be performed. Firstly, the simulation should converge according to the set criteria. Secondly, plotting the mesh along the objects shows whether the mesh is reasonable also along small features.

## 4.4 Derivation of the Qubit Properties

Following a successful simulation, evaluation of the results comes next. The transmission and reflection spectra presented in Figure 4.7 exhibit a first indication of the system behaviour. Figure 4.7 (a) shows the simulated transmission spectrum corresponding to a resonator frequency of about $9.5\,\mathrm{GHz}$. In Figure 4.7 (b), the simulated reflection

spectrum is shown. The reflection signal stays close zero as long as the excitation is detuned from the resonator frequency. In case of zero detuning, the reflected signal decreases where the transmission increases. From these graphs, one can draw the conclusion that the resonator works as expected and the resonator frequency can be determined.

In order to evaluate all important qubit and resonator parameters, the black-box quantisation must be applied. Therefore, the admittance spectrum obtained from HFSS is required and plotted in Figure 4.8. The imaginary and real part are plotted separately. The admittance as obtained from HFSS is shown in Figure (a). Only the resonator mode can be seen, which refers to the zero crossing of the imaginary part of the admittance (see Nigg et al. [2012]). Manually adding the junction properties as described in Section 3.7, shifts the admittance spectrum such that a second zero crossing of the imaginary part appears and this refers to the qubit frequency. From this data, $\mathrm{Im}[Y(\omega_p)]$ and $\mathrm{Re}[Y(\omega_p)]$ of both qubit and resonator mode as well as from their derivatives, all qubit-resonator parameters can be calculated.

Note, that the derivative of the imaginary part of the admittance at the resonator frequency is strongly dependent on the accuracy of the simulation and especially on the number of frequency points. It is therefore important to choose the frequency step size as small as possible. For accurate simulations it therefore might be useful to take a very fine sweep just around the resonator to obtain the accurate derivative.

## 4.5 Variation of the Design

The very first characterisation of the single coaxmon was made in (Spring [2016]). Starting from this design, further variations with the aim of optimisation are of interest. Furthermore, the experimental results shall be compared to simulations. For further optimisation, the spiral parameters length, thickness and the connection to the inner and outer resonator pad are investigated in simulations. Since the experiment exhibits much smaller lifetimes than simulation, investigations on how to improve lifetimes are made. In addition, the sample holder material and geometry is varied. Finally, experimental

| Qubit and Resonator | [mm] | Sample Holder | [mm] |
|---|---|---|---|
| $d_{Q1}$ | 0.125 | $d_{P1}$ | 0.38 |
| $d_{Q2}$ | 0.3895 | $d_{P2}$ | 0.90 |
| $d_{Q3}$ | 0.49 | $d_{G1}$ | 0.20 |
| $d_{R1}$ | 0.25 | $d_{G2}$ | 0.025 |
| $d_{R2}$ | 0.3895 | $d_1$ | 0.70 |
| $d_{R3}$ | 0.49 | $d_2$ | 0.40 |
| Spiral Length | 1.70 | Sapphire Chip | $5 \times 5 \times 0.5$ |
| Spiral Width | $3 \times 10^{-3}$ | | |
| Pad Thickness | $80 \times 10^{-6}$ | | |

Table 4.1: Single coaxmon parameters after optimisation and resulting in the qubit-resonator values as presented in Section 4.9 and in (Rahamim et al. [2017]). The definition of parameters follows Figure 4.2.

and simulation results are compared and found to agree well. All variations and their results are presented and discussed in the following. The varied parameters refer to the labelling in Figure 4.2.

### 4.5.1 Resonator Width

The first resonator design proposed by (Spring [2016]) has a width of $1\,\mu\mathrm{m}$ and a length of $1.5\,\mathrm{mm}$. However, the spiral as well as the qubit and resonator pads are supposed to be fabricated using photolithography. The length scale limit of this technique is exactly one micrometer. It is therefore preferably to increase the width slightly to $3\,\mu\mathrm{m}$ to not work at this limit.

For this reason, variations and their effect on the resonator frequency are investigated. Apart from this, the connection of the spiral to the islands was changed slightly to improve fabrication steps. A vertical connection of $10\,\mu\mathrm{m}$ length and of same thickness as the spiral is added between the islands and the spiral start and end respectively. The adjusted spiral is shown in Figure 4.7. In general, a superconducting inductor exhibits two types of inductance, namely the self inductance and the kinetic inductance. However, only the self inductance can be estimated without the knowledge of the current in the

| Spiral Width | 1 µm | 2 µm | 3 µm |
|---|---|---|---|
| $f_{\text{res}}$ (1.7 mm length) | 10.70 | 11.30 | 11.72 |
| $f_{\text{res}}$ (2.2 mm length) | 9.38 | 9.90 | 10.24 |

Table 4.2: Resonator width variations for two resonator spiral lengths of $1.7\,\text{mm}$ and $2.2\,\text{mm}$.

inductor. The dependence of the spiral self inductance on its dimensions is

$$L_{self}(l,w,t) = 2l \times \left(\ln\left(\frac{2l}{w+t}\right) + 0.5 + 0.2235\frac{w+t}{l}\right) \times 10^{-7} H \tag{4.2}$$

with width $w$, length $l$ and thickness $t$, each given in millimetre (Wadell [1991]). For widths of the order of a few micrometres, the logarithmic term dominates when the width is varied. Therefore, when broadening the spiral a decrease in the self inductance is expected. Since the resonator frequency is $\omega_r = \sqrt{\frac{1}{LC}}$, with the assumption that $L \propto L_{\text{self}}$, an increase in frequency is expected. Simulations verify this assumption and the obtained frequencies are presented in Table 4.2. As the aim is again to have a resonator frequency close to $10\,\text{GHz}$, a second sweep for a longer spiral is performed in order to compensate the increase in frequency due to the spiral widening. More about variations of the length follow in the next section.

### 4.5.2 Resonator Length

Changing the resonator width changes the resonator frequency. In order to readjust the frequency, the length is varied. One has to keep in mind that for later multi-qubits experiments different resonator frequencies are needed. Therefore, the effect of different resonators lengths is studied and the results are plotted in Figure 4.9. The values obtained from simulation are the blue data points. Using Equation 4.1 and $\omega_r = \sqrt{\frac{1}{LC}}$ allows one to fit the data as shown by the blue curve. As expected, increasing the length increases the inductance resulting in a decrease in frequency. The spiral length is calculated as described in equation 4.1. Start and end point are the spiral start and end, adding the $10\,\mu\text{m}$ connection to the islands gives the total resonator length The length is varied such

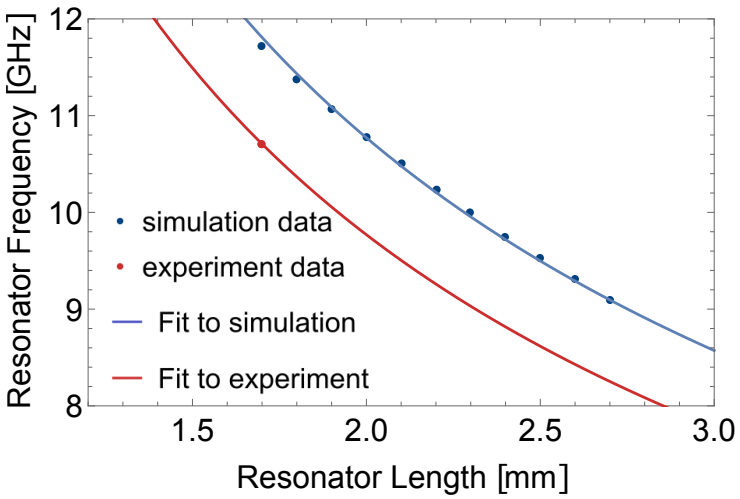


Figure 4.9: Resonator length variation. Blue are simulation data points fitted by the blue line. The obtained fit is then shifted to go through the experiment data point in red. The offset of simulation and experiment is caused by the limit in mesh size. All values for a $3\,\mu\mathrm{m}$ wide spiral, the resonator pin at $0.4\,\mathrm{mm}$ and the qubit pin at $0.7\,\mathrm{mm}$. (b) Table with the values listed. Error bars discussed in Section 4.6.

that frequencies between $9\,\mathrm{GHz}$ to $12\,\mathrm{GHz}$ are obtained. Band pass filters from $8\,\mathrm{GHz}$ to $12\,\mathrm{GHz}$ limit the range being used in the experiment. However, comparison to experiment shows that the experimental resonator frequency is smaller than in simulation. This is in agreement with the assumption made in Section 4.3.2, that the frequency is expected to converge to even smaller values for a finer mesh. Under the assumption that a finer mesh would only shift the resulting frequency to smaller values, the experimental data point is used to shift the fitted curve to the left, through the experimental data point in red. This way, the simulated behaviour can be projected onto the real experimental values. This allows one to estimate the frequencies for future resonators.

### 4.5.3 Control Pin Distance

Apart from dielectric loss, the control pins are expected to be the main contribution to loss. Varying the distance between the qubit and the control pin next to it shows a very strong dependence on the qubit lifetime $T_1$ in simulation. Table 4.3 shows all parameters dependent on the distance $d_1$ between qubit and qubit control pin. Here,

| $d_1$ mm | $f_{res}$ [GHz] | $f_{01}$ [GHz] | $\Delta$ [GHz] | $\chi$ [MHz] | g [MHz] | $\alpha$ [MHz] | $E_J$ [GHz] | $T_1$ [µs] |
|---|---|---|---|---|---|---|---|---|
| 0.1 | 10.19 | 7.11 | 3.08 | 5.53 | 438 | 302 | 20.15 | 1.90 |
| 0.2 | 10.20 | 7.23 | 2.97 | 7.38 | 482 | 311 | 20.15 | 7.3 |
| 0.3 | 10.21 | 7.21 | 3.0 | 7.53 | 491 | 309 | 20.15 | 21.2 |
| 0.4 | 10.21 | 7.21 | 3.0 | 7.63 | 495 | 309 | 20.15 | 50.0 |
| 0.5 | 10.21 | 7.21 | 3.0 | 7.67 | 497 | 309 | 20.15 | 103.9 |
| 0.6 | 10.21 | 7.21 | 3.0 | 7.64 | 496 | 309 | 20.15 | 159.1 |
| 0.7 | 10.21 | 7.20 | 3.1 | 7.59 | 496 | 308 | 20.15 | 206.5 |
| 0.8 | 10.21 | 7.20 | 3.1 | 7.68 | 498 | 308 | 20.15 | 205.2 |
| 0.9 | 10.21 | 7.21 | 3.0 | 7.69 | 497 | 309 | 20.15 | 203.4 |
| 1.0 | 10.21 | 7.21 | 3.0 | 7.72 | 489 | 309 | 20.15 | 199.1 |

Table 4.3: Qubit pin distance $d_1$ variation and the effect on the qubit-resonator parameters. Resonator pin at $0.4\,\mathrm{mm}$.

$f_{res}$ is the resonator frequency, $f_{01}$ the qubit frequency from ground to first excited state, $\Delta$ the qubit-resonator detuning, $\chi$ the dispersive or Stark shift representing the resonator shift when the qubit is excited or in the ground state, g the resonator-qubit coupling, $\alpha$ the anharmonicity of the qubit, $E_J$ the Josephson energy, $E_J/E_C$ the ratio of Josephson and capacitance energy and $T_1$ the qubit lifetime. None except the qubit lifetime seems to be dependent on the distance. One exception is at the closest pin distance of $0.1\,\mathrm{mm}$. At this distance, the pin is exactly at the same height as the sample holder. For all other cases, the pin vanishes slightly into the control pin cylinder in the sample holder. It might be, that here, the capacitances between the pin and the qubit and resonator islands are more effected by the change, resulting in a change in qubit and resonator frequency and hence slightly different qubit and resonator behaviour.

In Figure 4.10, $T_1$ is plotted as a function of the pin distance. Clearly, the qubit lifetime increases when pulling the pin away from the chip. This shows that the qubit pin seems to be a major contribution as a loss channel. However, at a distance of $0.7\,\mathrm{mm}$ the lifetime levels out at $200\,\mu\mathrm{s}$. At this point, it seems that another loss channel overcomes. This might be the resonator pin, as it is $0.65\,\mathrm{mm}$ distant from the qubit with the sapphire chip in between. In order to investigate this, the resonator pin distance $d_2$ is varied as well,

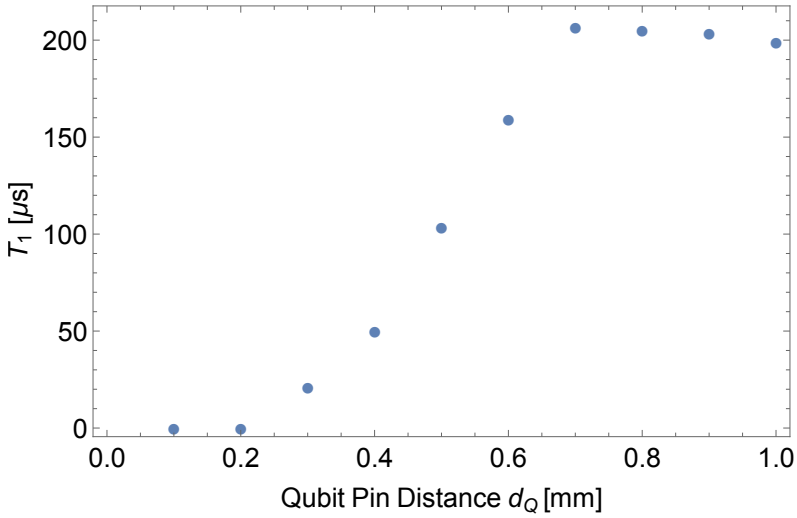


Figure 4.10: Qubit lifetime $T_1$ as a function of qubit pin distance $d_1$. Up to $0.7\,\mathrm{mm}$., the larger the distance the higher $T_1$. For $d_1 > 0.7\,\mathrm{mm}$ levels out at $200\,\mu\mathrm{s}$.

| $d_2$ mm | $f_{res}$ [GHz] | $f_{01}$ [GHz] | $\Delta$ [GHz] | $\chi$ [MHz] | g [MHz] | $\alpha$ [MHz] | $E_J$ [GHz] | $E_J/E_C$ - | $T_1$ [µs] |
|---|---|---|---|---|---|---|---|---|---|
| 0.2 | 10.19 | 7.22 | 2.97 | 6.89 | 475 | 311 | 20.15 | 65 | 107.5 |
| 0.3 | 10.22 | 7.22 | 3.00 | 6.92 | 474 | 311 | 20.15 | 65 | 201.9 |
| 0.4 | 10.24 | 7.19 | 3.05 | 6.72 | 473 | 308 | 20.15 | 65 | 193.0 |
| 0.5 | 10.24 | 7.23 | 3.01 | 7.00 | 471 | 310 | 20.15 | 65 | 194.7 |
| 0.6 | 10.24 | 7.22 | 3.02 | 6.95 | 464 | 311 | 20.15 | 65 | 189.7 |

Table 4.4: Resonator pin distance $d_2$ variation and the effect on the qubit-resonator parameters. Qubit pin at $0.7\,\mathrm{mm}$.

while the qubit pin is kept fixed. Table 4.4 shows the results. Here, it looks like the qubit lifetime is not effected by it as long as the resonator pin is at least $0.3\,\mathrm{mm}$ away from the resonator. From this, the conclusion can be drawn, that at least $0.3\,\mathrm{mm}$ resonator pin distance and $0.7\,\mathrm{mm}$ qubit pin distance should be kept, such that the experiment lifetime is not limited by the pins. To check this, a test experiment could be performed without any qubit control pin at all and solely driving the qubit and resonator though the resonator control pin.

### 4.5.4 Sample Holder

The sample holder is another object that can be optimised. One question is whether a different material or different size of the hole for the sapphire chip affects the qubits' properties. At first, investigations of the effect of copper instead of aluminium for the sample holder are made. Whereas the qubit and resonator frequencies do not seem to change at all, a change in the qubit's lifetime can be observed. The simulation was performed for two different qubit pin distances. For both cases the lifetime for a copper sample holder did not reach 35% of the same simulation with aluminium instead. The assumption is, that copper as a non-superconductor allows the electromagnetic fields to penetrate relatively far into the material compared to the Landau penetration depth of a superconductor such as aluminium. A bigger loss is therefore expected and the results can be seen in the qubits' lifetimes.

Another question is, whether the distance $d_{G1}$ between sapphire chip and sample holder plays a role for the qubit lifetimes. Eventually, a larger distance reduced the fraction of fields within the dielectric sapphire and hence reduces dielectric loss resulting in an increasing qubit lifetime. This is tested with simulation. The results are listed in Table 4.5. Widening the gap $d_{G1}$ does only seem to have an effect on the qubit lifetime at very close distances. Once it is $0.1\,\mathrm{mm}$ away, there is no systematic increase in the lifetime anymore. Therefore, the distance is recommended to be at least $0.1\,\mathrm{mm}$ wide.

| $d_{G1}$ mm | $f_{res}$ [GHz] | $f_{01}$ [GHz] | $\Delta$ [GHz] | $\chi$ [MHz] | g [MHz] | $\alpha$ [MHz] | $E_J$ [GHz] | $E_J/E_C$ - | $T_1$ [µs] |
|---|---|---|---|---|---|---|---|---|---|
| 0.05 | 10.21 | 7.24 | 2.97 | 7.61 | 492 | 307 | 20.37 | 66 | 166 |
| 0.10 | 10.24 | 7.22 | 3.02 | 6.70 | 467 | 307 | 20.37 | 66 | 193 |
| 0.15 | 10.24 | 7.27 | 2.97 | 6.81 | 462 | 311 | 20.37 | 66 | 180 |
| 0.20 | 10.23 | 7.27 | 2.96 | 6.75 | 458 | 311 | 20.37 | 66 | 170 |
| 0.25 | 10.23 | 7.28 | 2.95 | 6.77 | 458 | 312 | 20.37 | 66 | 189 |
| 0.30 | 10.23 | 7.26 | 2.97 | 6.68 | 458 | 310 | 20.37 | 66 | 184 |

Table 4.5: Sample holder optimisation: Distance variation between chip and sample holder $d_{G1}$.

## 4.6 Quantifying the Simulation Error

In this Section, the error of the simulation is quantified. A quantification of the statistical error as well as of a systematic error is given in the following.

In general, the convergence criteria and accuracy of the simulation are set in HFSS manually. The convergence criteria is determined by the value $\Delta S$, which describes the change in the calculated S-matrix of the system. In case of the coaxmon simulation, this is set to $\Delta S = 0.001$, the smallest possible value allowing the simulations to still run on the external cluster. From this error, it is not feasible to determine the errors resulting on the qubit and resonator parameters. The error of the S-matrix would have to be transferred on to the admittance spectrum and this error would then have to be propagated through the black-box quantisation calculations. Another more reasonable way to find a statistical error of the simulation is given by the following. As experience with HFSS shows, the error on the simulation results is strongly given by the mesh. As already noticed in Section 4.3.2, the mesh is the crucial factor determining the accuracy of the simulation values such as the resonator frequency. This is why, in order to find the statistical uncertainty of the simulation results a slightly different mesh is enforced by slightly varying the geometry. For relatively small variation, the simulation should result in negligible differences in the physical values, but instead give an idea of the statistical error. The standard deviation of these variations is calculated and is taken as a statistical error due to the mesh.

| | $f_{res}$ [GHz] | $f_{01}$ [GHz] | $\Delta$ [GHz] | $\chi$ [MHz] | g [MHz] | $\alpha$ [MHz] | $E_J/E_C$ - | $T_1$ [µs] |
|---|---|---|---|---|---|---|---|---|
| $\sigma$ [%] | 0.04 | 0.08 | 0.2 | 0.5 | 0.2 | 0.2 | 0.2 | 4.0 |

Table 4.6: Statistical simulation errors on the qubit-resonator parameters obtained from HFSS simulation.

For example, to find the standard deviation for the simulation results of the resonator variations at $3\,\mu m$, the width is very slightly varied to be $2.98\,mm$, $2.99\,mm$, $3.00\,mm$, $3.01\,mm$ and $3.01\,mm$. From this change of less than 1%, only a small change in the results is expected but variation of the results then give a chance to estimate the statistical simulation error for the resonator width caused by the mesh. The standard deviation of the five numbers is then calculated and given in percentage of the mean value of the resonator frequency. This testing was performed for all optimisation procedures described in this Chapter. For example, for the qubit pin distance, simulation results of a qubit pin distance of $0.698\,mm$, $0.699\,mm$, $0.700\,mm$, $0.701\,mm$ and $0.702\,mm$ are taken to calculate a standard deviation. Analogously, this was done at the qubit pin distance of $0.4\,mm$. It turns out, that the errors for the different types of optimisations do not vary, hence one set of statistical errors is given here for all simulations. The hereby obtained errors in percentage of all qubit-resonator parameters are given in Table 4.6. The statistical error in most cases is fairly small, below 1%. Only the qubit lifetime shows a slightly larger error of 4%.

However, the assumption is, that the overall error is dominated not by the statistical error but by a systematic one. As discussed in Section 4.3.2, the resonator frequency can not be simulated accurately due to a limit in mesh size. Since all qubit-resonator parameters are strongly dependent on a correct resonator frequency, a calibration is performed to correct for this offset in the resonator frequency. In specific, the resonator spiral in the simulation is intentionally increased such that the resonator frequency attained from simulation with a mesh size of $1\,\mu m$ corresponds to the experimentally determined value. This calibration to experiment matches with an approximate extrapolation of the frequency, to which the transmission peak in Figure 4.6 converges to. In order to now

| | $1\,\mu m$ mesh | $5\,\mu m$ mesh | deviation [%] |
|---|---|---|---|
| $f_{res}$ [GHz] | 10.23 | 10.23 | 0.0 |
| $f_{01}$ [GHz] | 7.23 | 7.23 | 0.0 |
| $\Delta = (f_{01} - f_{res})$ [GHz] | -3.00 | -3.0 | 0.0 |
| $\chi/(2\pi)$ [MHz] | -6.70 | -6.90 | 3.0 |
| $E_J$ [GHz] | 20.31 | 21.7 | 6.8 |
| $E_C$ [MHz] | 309 | 286 | 7.5 |
| $E_J/E_C$ | 65.8 | 75.9 | 15.4 |
| $g/(2\pi)$ [MHz] | 467 | 486 | 4.1 |
| $T_1$ [µs] | 210 | 332 | 58 |

Table 4.7: Systematic error derivation of the single coaxmon parameters by comparing simulation results of $1\,\mu m$ and $5\,\mu m$ mesh size.

obtain the systematic error due to the limited mesh size the following comparison is made. Plotting the obtained resonator frequency as a function of mesh size, gives an idea of the frequency to which simulation converges to. The obtained frequency of a simulation with a $1\,\mu m$ mesh is then approximately $1\,GHz$ larger than the convergence value. In the other direction, a $1\,GHz$ difference in the simulated resonator frequency is also obtained by setting the mesh length to $5\,\mu m$. For this reason, simulation of $1\,\mu m$ mesh length and $5\,\mu m$ for the resonator frequency of $10.23\,GHz$ are compared and the difference is taken as the systematic error due to the limited mesh size. The resulting values from this are listed in Table 4.7 for comparison with experiment and the HFSS results. The obtained values clearly show that the assumption is correct, that this error overcomes the statistical one. The qubit and resonator frequencies are calibrated to match, hence their deviation is zero. The other values show an error of a percent. A large systematic error is found for the $E_J/E_C$ ratio and the qubit lifetime, stating that these values have to treated carefully.

Besides the derived statistical and systematic error of the simulation, more error sources have to be named of which no quantification is possible. For example, there are additional errors resulting from the neglection of the third dimension of the aluminium pads in the simulation. Additionally, imperfect material properties of sapphire, aluminium and copper such as dirty chip surfaces are not considered. Also imperfections in fabrication of the circuit remain neglected. Furthermore, the values taken for the anisotropy of the

sapphire are extrapolation values, hence resulting in a simulation error as well. These additional error sources cannot be quantified easily but should be kept in mind when comparing simulations to experimental results.

## 4.7 The Lumped Element Model

Another approach to calculate the coaxmon properties is to exploit the lumped element method. For any lumped element electric circuit the quantised Hamiltonian can be found. Applying perturbation theory onto the obtained Hamiltonian allows determination of parameters such as the qubit-resonator coupling strength and cross- and self-Kerr shift between circuit components. This method is described in (Zagoskin [2011]). Here, the steps to derive the Hamiltonian for the single coaxmon are discussed. The detailed description of how to effectively solve for it in mathematica will be described in the future thesis (Patterson [2018]). Using this theory allows one to derive all qubit-resonator parameters dependent on the capacitances of the system. Inserting these from Maxwell, all parameters can be calculated and compared to HFSS simulations and experiments.

First of all, the Lagrangian $\mathcal{L} = T - U$ with the kinetic energy $T$ and potential energy $U$ of any circuit can be derived. The contribution of common circuit elements are $\Delta\mathcal{L} = \frac{1}{2}C\dot{\Phi}^2$ for a capacitor C and node voltage $\dot{\Phi}$, $\Delta\mathcal{L} = -\frac{\Phi^2}{2L}$ for the inductor L, and $\Delta\mathcal{L} = E_J \cos\frac{2\pi\Phi}{\Phi_0}$ for a Josephson junction with energy $E_J$ and the flux quantum $\Phi_0$. The Lagrangian $\mathcal{L} = \mathcal{L}(\Phi, \dot{\Phi})$ is then a function of the node fluxes $\Phi$ and voltages $\dot{\Phi}$ where the flux is the integral in time of the potential difference across one circuit element. Introducing the canonical momentum conjugate $\Pi$ to the variable $\Phi_a$ allows one to write the Hamiltonian of the circuit as:

$$\mathcal{H}(\Pi, \Phi) = \sum_a \Pi_a \dot{\Phi}_a - \mathcal{L}(\Phi, \dot{\Phi}) \quad \text{with} \quad \Pi_a = \frac{\partial \mathcal{L}}{\partial \dot{\Phi}_a}. \tag{4.3}$$

For the single coaxmon circuit the resulting Hamiltonian is:

$$\mathcal{H}_{\mathrm{C}}(\Pi, \Phi) = L\left(\Phi_1 - \Phi_2\right)^2 + E_J \cos\frac{2\pi(\Phi_3 - \Phi_4)}{\Phi_0} + \sum_i \sum_j 2C_{ij}\left(\Pi_i - \Pi_j\right)^2. \tag{4.4}$$

The first term describes the inductor with a flux difference $\Phi_1 - \Phi_2$, the second represents the Josephson junction across which the flux difference is $\Phi_3 - \Phi_4$, and the last term sums up all contributions due to the capacitances between the nodes $i, j$ where $\Pi_i - \Pi_j$ is the charge difference across a capacitance between the nodes $i$ and $j$.

So far, the Hamiltonian is purely classical. However, before performing the second quantisation, a new set of coordinates should be chosen such that the later introduced ladder operators then have a clear physical meaning as for example the creation or annihilation of a photon in the resonator. To do so, the flux and charge differences in Equation 4.4 are redefined with $\tilde{\Phi}_i = \Phi_i - \Phi_j$ and $\tilde{\Pi}_i = \Pi_i - \Pi_j$ respectively. Now, the second quantisation can be performed with the introduction of the creation operator $a^\dagger$ and annihilation operator $a$:

$$\hat{\tilde{\Phi}}_i = \frac{\hat{a}_i + \hat{a}_i^\dagger}{2}\Lambda, \quad \hat{\tilde{\Pi}}_i = \hbar\frac{\hat{a}_i - \hat{a}_i^\dagger}{i\Lambda}. \tag{4.5}$$

In this case, $\Lambda$ is an arbitrary constant. Taking $[\hat{a}, \hat{a}^\dagger] = 1$, the commutation relation $[\hat{\tilde{\Phi}}, \hat{\tilde{\Pi}}] = i\hbar$ is satisfied. With the new set of coordinates, $\hat{a}_1$ and $\hat{a}_1^\dagger$ now describes creating and annihilating a photon in the resonator. Further, expanding the cosine in Equation 4.4 to fourth order in $\Phi$ allows one to take the anharmnicity of the Josephson junction into account. Finally, choosing $\Lambda$ such that the first order anharmonic term drops out allows one to bring the Hamiltonian into the common form, where the resonator is harmonic and its frequency is proportional to $\hat{a}^\dagger\hat{a}$. All interesting qubit-and resonator parameters can be calculated from the obtained Hamiltonian. The harmonic resonator frequency can be found by looking at the term proportional to $\hat{a}^\dagger\hat{a}$. The anharmonicity is given by the $\hat{a}^\dagger\hat{a}\hat{a}^\dagger\hat{a}$ term as this is equal to $\hat{n}^2$. Furthermore, the qubit-resonator coupling strength is refers to the coefficient of the term $\hat{a}_i^\dagger\hat{a}_j + \hat{a}_j^\dagger\hat{a}_i$, where $i, j$ stand for the qubit and resonator. At last, the qubit-qubit coupling in the case of a multi-coaxmons circuit is given by the term $\hat{a}_i^\dagger\hat{a}_j + \hat{a}_j^\dagger\hat{a}_i$ where $i, j$ are qubit one and two.

Using Maxwell, the complete capacitance matrix of the single coaxmon can be evaluated and substituted into Equation 4.4. The capacitances for the optimised single coaxmon can be found in Table 4.8. With the additional knowledge of the Josephson energy $E_J$

| | In | Out | $Q_{\text{inner}}$ | $Q_{\text{outer}}$ | $R_{\text{inner}}$ | $R_{\text{outer}}$ | Ground |
|---|---|---|---|---|---|---|---|
| In | - | $3.34 \times 10^{-5}$ | 0.1409 | 0.1579 | 0.02577 | 0.02846 | 587.5 |
| Out | $3.34 \times 10^{-5}$ | - | 0.01235 | 0.04838 | 1.355 | 0.4706 | 605.4 |
| $Q_{\text{inner}}$ | 0.1409 | 0.01235 | - | 20.83 | 11.83 | 9.036 | 9.830 |
| $Q_{\text{outer}}$ | 0.1579 | 0.04838 | 20.83 | - | 26.87 | 63.38 | 143.1 |
| $R_{\text{inner}}$ | 0.02578 | 1.355 | 11.83 | 26.87 | - | 59.35 | 25.05 |
| $R_{\text{outer}}$ | 0.02846 | 0.4706 | 9.036 | 63.38 | 59.35 | - | 136.9 |
| Ground | 587.5 | 605.4 | 9.830 | 143.1 | 25.05 | 136.9 | - |

Table 4.8: Capacitance matrix for the single coaxmon. All values in femtofarad. Maxwell computes the capacitances to an accuracy of 0.1%.

and the inductance $L$ of the resonator, all circuit parameters can be derived except for the qubit lifetime. The results of the lumped element model are listed in Table 4.9 and further discussed in Section 4.9 when comparing to experiment.

## 4.8 The Network Analysis

An alternative approach to determine the qubit-resonator coupling is done by a simple network analysis. This analysis provides a second theoretical reference and later is essential to calculate multi-qubit selectivities. Here, the analysis is introduced for the case of a single coaxmon. By considering the electric circuit and applying Kirchhoff's laws, a set of coupled equations can be written down and then solved for parameters of interest. The procedure is shown for a simple capacitance network in Figure 4.11. A voltage is applied to two capacitors in series. The voltage drop across each capacitor must sum to the applied voltage $V$. On opposite sides of each capacitor the absolute value of charge is the same but with opposite signs. On the isolated island in between the capacitors, the charge sums to zero. In addition for each capacitor its charge $Q_i$ is equal to $C_i V_i$ Therefore, the set of equations to be satisfied is

$$Q_i = C_i V_i, \quad i = 1, 2 \tag{4.6}$$

$$V = V_1 + V_2, \tag{4.7}$$

$$Q_2 - Q_1 = 0. \tag{4.8}$$

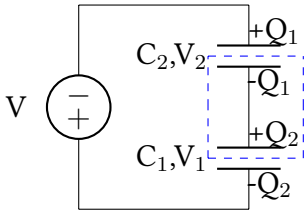


Figure 4.11: Simple circuit example for network analysis. A voltage V is applied to two capacitor in series. The charge on each side of the capacitors is the opposite. The charge on the island in between the capacitors sums up to zero.

Now, for example the voltage drop across the first capacitor can be compared to the applied voltage with the knowledge of the capacitances from Maxwell:

$$\frac{V_1}{V} = \frac{C_2}{C_1 + C_2}. \tag{4.9}$$

Analogously, the coupled equations can be found in case of the coaxmon circuit shown in Figure 4.12. Neglecting the capacitance of the junction ($< 1$ fF) and the resonator spiral, it is possible to compute the voltage drop across the qubit for a given applied voltage across the resonator. The ratio of the these voltages corresponds to the coupling of the resonator to the qubit. According to (Koch et al. [2007]) the qubit resonator coupling then is given by

$$g = \frac{2}{\hbar}\sqrt{\frac{1}{2}}\left(\beta e V_{rms}\right)\left(\frac{E_J}{8E_C}\right)^{\frac{1}{4}} \qquad \text{with} \qquad V_{rms} = \sqrt{\frac{\hbar\omega_r}{2C_r}}. \tag{4.10}$$

Here, $\beta$ refers to the relative voltage drop across the qubit when a voltage is applied to the resonator, $\omega_r$ and $C_r$ are the resonator frequency and capacitance respectively and $E_J$ and $E_C$ the Josephson and charging energy. With the capacitance matrix in Table 4.8, the resonator-qubit coupling strength is calculated to be $g = 488\,\mathrm{MHz}$.

As shown in Table 4.9, the measured coupling strength is $462\,\mathrm{MHz}$. Even though, this simulation was purely static, the Josephson junction is neglected and there is no inductive coupling taken into account, the calculated and measured values are of the same order. Discrepancy to experiment is assumed to be due to the approximations as stated. This analysis not only offers another way to calculate the resonator-qubit coupling strength,

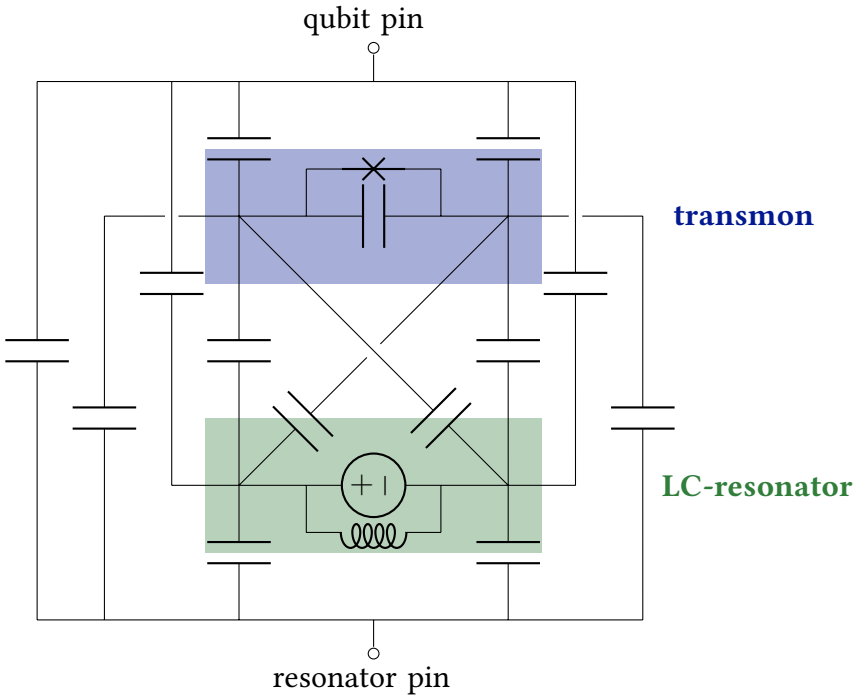


Figure 4.12: The coaxmon electric circuit for the network analysis. The qubit in blue consists of the Josephson juncton in parallel to a capacitor. The resonator in green serves as a imaginary voltage source. All islands are capacitively coupled. Capacitances to ground are not shown.

but also opens the way to estimate the selectivity in a multi-qubit experiment as discussed in Section 5.4.

## 4.9 Comparison to Experiment

The optimised single coaxmon device has been fabricated by another member of the group. Its experimental characterisation is officially presented in (Rahamim et al. [2017]). This publication can be found in the appendix. The qubit and resonator parameters are presented in Table 4.9, both experimentally determined values and the ones resulting from HFSS/black-box quantisation model and the lumped element model are listed. Note, that for the HFSS simulation the inductor was lengthened to achieve the same resonator frequency as in the experiment as the simulations are limited in the mesh size as discussed in Section 4.3.2. The inductance of the spiral and the Josephson energy

are added in the lumped element model such that the frequencies of the resonator and qubit match the experimental ones. In contrast to this, the resonator frequency in the HFSS model comes purely from the simulation, but the qubit frequency is also matched to the experimental one by tuning the Josephson energy which is added in the black-box quantisation. Hence, the frequencies for all three models are nearly identical. The $\chi$-shift is of the same order of magnitude, whereas the HFSS value is closer to experiment than the lumped element model. The same holds true for the Josephson energy $E_J$. Remember that this value is adjusted such that the qubit frequencies match. The discrepancy in the values of $E_J$ demonstrates that in either case the junction is not modelled perfectly. Note that in HFSS and the black-box quantisation model, the system is assumed to be dissipationless. In the lumped element model, only static fields neglecting for example inductive couplings are considered. The capacitance energy $E_C$ shows that the assumptions made in the lumped element model seem to have an higher impact, since the value is off by a third. However, the qubit-resonator coupling again is of the same order and agrees well for HFSS and the experiment. As discussed before, the qubit lifetime in the simulation are a lot greater than in experiment. Further investigations concerning experimental loss channels are under way. The lumped element model does not allow one to calculate the qubit lifetime since no dissipation is taken into account.

The HFSS method demonstrates to be a powerful tool to simulate the single coaxmon device. All qubit parameters can be estimated before fabrication and thus allowing for device optimisation prior to fabrication. However, running these simulations is computationally intense and can take two to twenty-four hours, which is time consuming and costly. Furthermore, the mesh can not be reduced enough to obtain the correct resonator frequency even with $256\,\mathrm{GB}$ memory. Only the knowledge of the systematic shift from comparison to experiment allows one to estimate the frequencies correctly in the future. Nonetheless, the method provides the possibility to make good predictions. In comparison, the lumped element model can be applied fairly easily, since Maxwell simulations can be run within a few minutes. However, since this model makes more rudimental assumptions such as only considering static fields, the estimated values do not agree

| | Experiment | Exp. Error | HFSS | HFSS Error | LEM |
|---|---|---|---|---|---|
| Resonator length [mm] | 1.7 | - | 2.2 | - | - |
| $f_{res}$ [GHz] | 10.22876 | 0.00005 | 10.24 | - | 10.23 |
| $f_{01}$ [GHz] | 7.2297 | 0.0005 | 7.23 | - | 7.23 |
| $\Delta = (f_{01} - f_{res})$ [GHz] | -2.9991 | 0.0005 | -3.01 | - | -3.00 |
| $\chi/(2\pi)$ [MHz] | -6.34 | 0.07 | -6.7 | 2 | -7.79 |
| $E_J$ [GHz] | 24.05 | 0.08 | 20.3 | 1.4 | 16.07 |
| $E_C$ [MHz] | 294 | 1 | 309 | 23 | 406 |
| $E_J/E_C$ | 81.8 | 0.6 | 68 | 10 | 39.6 |
| $g/(2\pi)$ [MHz] | 462 | 2 | 467 | 19 | 416 |
| $T_1$ [µs] | 4.1 | 0.01 | 210 | 122 | - |

Table 4.9: Comparison of experiment to HFSS simulation and the lumped element model (LEM) values. In HFSS, the resonator frequency is calibrated by the resonator length to match experiment. The qubit frequency is adjusted by $E_J$. In the LEM, $E_J$ and $L_J$ are set to give the aimed qubit and resonator frequency. Errors for the LEM result from the assumption of this method such as only considering static fields and therefore cannot be estimated with the same method.

as well as the others predicated by the HFSS model. However, this model will become important for two-qubit simulations as HFSS simulations become too computationally intense.

# 5 Design and Simulation of Two Coupled Coaxmons

In order to perform entangling operations on two qubits, it is necessary to introduce a coupling between them. The next step for the coaxmon is to design such a two-coaxmon device and to implement a two-qubit logic gate. This Chapter starts with the investigation of available two-qubit gates. Two suitable two-qubit gates for the coaxmon architecture are explained and discussed in Section 5.1 and the necessary requirements are determined. According to the desired device parameters, the two coaxmon device has to be designed. The double coaxmon is presented in Section 5.3. In order to adjust the additional coupling capacitance correctly, a lumped element model (Section 5.3.1) is used to calculate the expected qubit-qubit coupling strength. In Section 5.3.2, the capacitance is then iteratively adjusted by using this model and simulating the capacitance matrix via Maxwell. The resulting coupled design then fulfils all gate requirements.

Being able to selectively address each single qubit is also a key requirement for the implementation of a full set of quantum logic gates in a multi-qubit device. The question is how selective the qubits in the coupled coaxmon device can be driven without driving the second qubit as well. This question is answered in Section 5.4 showing that the coupled two coaxmon design achieves highly selective qubit control. Based on these investigations, the first coupled design was fabricated and measured.

## 5.1 Two Qubit Gate Theory

In this Section, two different two-qubit gates are presented. Their working principle is explained and their requirements are determined. Various two-qubit gates have been

discovered but only a few fulfil the requirements given by the coaxmon architecture. A general introduction into quantum gates for superconducting qubits can be found in (Rigettir [2009]). The gate for coaxmons has to be realised with a microwave control setup, fixed frequency qubits and a non-tunable qubit-qubit coupling. Furthermore, we are limited in the precision of the fabrication of the devices, especially of their qubit frequency, which can only be fabricated with an accuracy of $\pm 1\,\mathrm{GHz}$. The Cross-Resonance (CR) gate in (Chow et al. [2011]) and the microwave-activated conditional phase (MAP) gate in (Chow et al. [2013]) fulfil these requirements and are therefore taken into closer consideration.

### 5.1.1 MAP Gate

The microwave-activated conditional phase (MAP) gate relies on a specific energy level alignment. For the MAP gate, the qubit transitions $|12\rangle$ and $|03\rangle$ are designed to be degenerate. This is shown in Figure 5.1. Here, the first number represents the state of qubit one and the second the state of qubit two. In this case, the interaction between them causes a shift to new eigenfrequencies. With the original degenerate energy levels, the transition frequencies $|11\rangle \rightarrow |12\rangle$ and $|01\rangle \rightarrow |02\rangle$ have the same energy $E_A$. Due to the coupling of the degenerate states, this is not the case for the shifted energy levels, and the transition energy $E_B$ for $|11\rangle \rightarrow |12\rangle$ is different to $E_A$. Hence, this artificially introduced coupling of two states causes a difference in the transition frequency for qubit two to go from the first to the second excited state dependent on the state of qubit one. If qubit one is in its ground state, the frequency is $E_A/h$. If qubit one is excited, the frequency is $E_B/h$ with $E_A \neq E_B$. This state dependent difference for the transition frequency can be exploited to realise the state dependent gate. An off resonant drive on $|11\rangle$ gives rise to a different phase compared to the other states in the computational basis, denoted in grey in Figure 5.1. The MAP gate acts as a controlled NOT gate. This means, that the state of qubit two is changed if and only if the qubit one is excited.

To summarise the requirements, the MAP gate works due to the degeneracy of the energy levels $|12\rangle$ and $|03\rangle$. This allows the introduction of the state dependent transition

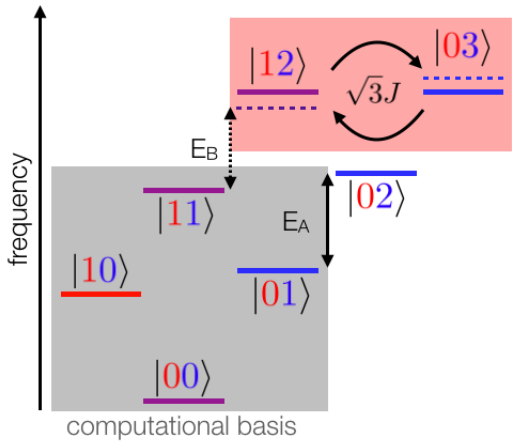


Figure 5.1: MAP gate working principle. The red numbers indicate the state of qubit one whereas blue represents qubit two. The qubits are designed such that the frequencies $|12\rangle$ and $|03\rangle$ are the same. Due to new shifted eigenenergies, the ground to excited state transition of qubit two is dependent on the state of qubit one. If this is in its ground state, the energy $E_A$ is needed to excite qubit two, otherwise it is shifted to $E_B$. Figure is adapted from (Chow et al. [2013]).

frequency used for the gate. Furthermore, the weak coupling limit $J \ll |\omega_2 - \omega_1| = \Delta$ where $J$ is the qubit-qubit coupling and $\Delta$ the detuning of the qubit frequencies, is required as well as a small drive strength $\Omega \ll \Delta$. If J is of the same order of the detuning or larger a resonant coupling would yield into a continuous swapping of the two qubits' states. If the drive is too large, the second qubit is driven off-resonantly and not due to the gate.

Due to the fact, that fabrication has an uncertainty of $\pm 1$ GHz on the qubit frequencies, the degeneracy of the transitions $|12\rangle$ and $|03\rangle$ is very difficult to achieve. This is why the focus will lie on the following Cross-Resonance gate. However, if this specific alignment of the qubit energies is realised, the MAP gate offers an elegant way to perform a two-qubit gate and is listed here as a possible two-qubit gate for the coaxmon architecture.

### 5.1.2 Cross-Resonance Gate

Another two-qubit gate for fixed-frequency and non tunable qubit-qubit coupling devices is the Cross-Resonance (CR) gate as presented in (Chow et al. [2011], Rigetti and Devoret

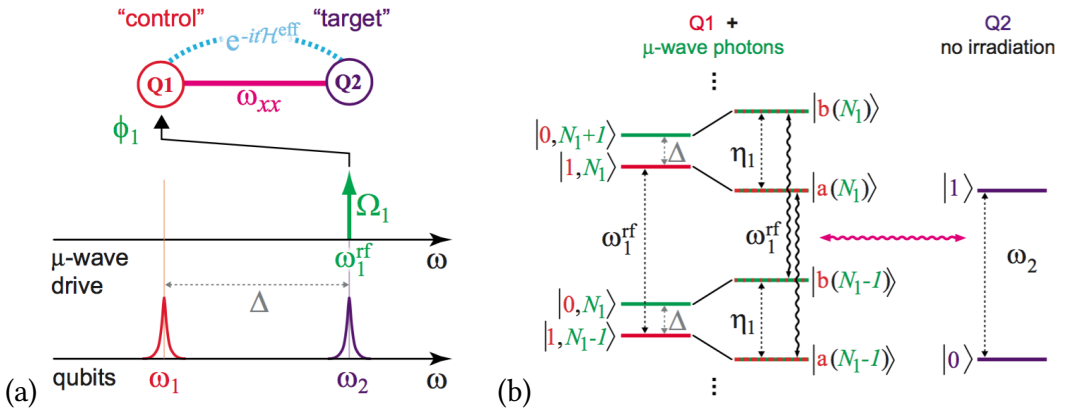


Figure 5.2: The Cross-Resonance working principle. (a) The target qubit's frequency is applied to the control qubit. (b) The dressed state picture of the qubits' states. The applied frequency causes a shift of the energy levels such that the transitions $|b(N1)\rangle \rightarrow |b(N1-1)\rangle$ and $|a(N1)\rangle \rightarrow |a(N1-1)\rangle$ have exactly the splitting of the applied, which is the target qubit's frequency, allowing to excite the target qubit through spontaneous emission. A phase dependence on the control qubit state is acquired and shown when deriving the effective drive Hamiltonian in Equation 5.1. Pictures taken from (Rigetti and Devoret [2010]).

[2010]). The principle of the CR gate is depicted in Figure 5.2. The dressed state picture used here allows one to understand its basic working principle. For a full understanding, including the phase dependence of the gate, the Hamiltonian has to be derived as done in (Rigetti and Devoret [2010]). Here, only the resulting drive Hamiltonian is discussed.

For the CR gate, the control and the target qubit have two different frequencies, see Figure 5.2 (a). Applying a microwave drive to the control qubit with the frequency of the target qubit introduces an effective interaction between the qubits. The dressed state picture of the energy levels is shown in Figure 5.2 (b). The applied drive causes the energy levels to shift and separate by the effective Rabi frequency $\eta = \sqrt{\Omega^2 + \Delta^2}$ with the Rabi frequency $\Omega$ and detuning $\Delta$ of the drive to the qubit frequency. This separation is independent of the state of the control qubit but only depends on the drive strength and its detuning. The transitions $|b(N1)\rangle \rightarrow |b(N1-1)\rangle$ and $|a(N1)\rangle \rightarrow |a(N1-1)\rangle$ have exactly the frequency of the drive, namely the frequency of the target qubit, here denoted as $\omega_1^{rf}$. Assuming that $a(N1)$ or $b(N1)$ decays, the emitted frequency is resonant with the target qubit and can excite it. This means, that by applying

the target qubit's frequency to the control qubit, a qubit-qubit interaction is introduced.

An additional phase is acquired dependent on the state of the control qubit, which is important when implementing the two-qubit gate. This becomes clear when the effective Hamiltonian is derived. The effective drive Hamiltonian (Chow et al. [2011]) is

$$\hat{H}_D = \epsilon(t) \left( \hat{\sigma}_{x,1} + \frac{J}{\Delta_{12}} \hat{\sigma}_{z,1} \hat{\sigma}_{x,2} \right). \tag{5.1}$$

Here, $\epsilon(t)$ is the drive strength, $\Delta_{12}$ the qubit-qubit detuning and $J$ the qubit-qubit coupling strength. The first term describes the direct drive of the control qubit. The second term shows that the target qubit is driven as well with a drive strength that is reduced by the prefactor $J/\Delta_{12}$. Additionally, as noted before the drive of the target qubit acquires a phase which is dependent on the state of the control qubit. $\sigma_{z,1}$, which can be $\pm 1$, changes the effective drive of the target qubit.

The requirements for the CR gate are similar to the MAP gate requirements. A weak coupling limit as well as a small drive is needed for the same reasons. In contrast to the MAP gate, no specific energy level alignment is required. It is important to note that for the CR gate the selectivity plays an significant role. A non-selective drive rotates the second qubit directly without acquiring the same state dependent phase, hence making it harder to see the cross-resonance interaction.

## 5.2 Simulation of the Cross-Resonance Gate

By reading the CR papers (Chow et al. [2011], Rigetti and Devoret [2010]) the actual implementation of this gate in the experiment is not obvious, i.e. which pulse sequence is applied. Therefore, the idea here is to simulate the gate and thereby gather more knowledge about its behaviour. The gate fidelity is the crucial value describing the gate performance and therefore should be optimised. It depends on device parameters such as the qubit lifetimes and the selectivity of the system. The latter describes the unwanted drive felt by the second qubit when applying a drive to the first qubit. In order

to understand and later optimise the gate fidelity for the coaxmon for different lifetimes of the qubits and selectivities, the gate can be simulated using the Master Equation.

To do so, the Master Equation introduced in Section 5.2.1 is solved for the CR Hamiltonian described in Section 5.2.2. The simulation results then are presented in Section 5.2.3 and possible optimisation steps are discussed in Section 5.2.4.

### 5.2.1 The Master Equation

The Lindblad form of the Master Equation given in 5.2 describes the dynamics of an open quantum system. With the Markovian assumption that the environment has no memory, the Master Equation 5.2 can be written as

$$\mathcal{L} := \frac{\mathrm{d}\rho}{\mathrm{d}t} = \underbrace{-\frac{i}{\hbar}\left[H, \rho\right]}_{\substack{evolution\ of \\ closed\ system}} + \underbrace{\sum_j h_{n,m}\left[L_j \rho L_j^\dagger - \frac{1}{2}\left\{L_j^\dagger L_j, \rho\right\}\right]}_{\substack{Lindblad\ operators \\ representing\ coupling \\ of\ system\ to\ environment}}. \tag{5.2}$$

The first term represents the simple von Neumann equation, namely the evolution of the density matrix $\rho$ of a closed system with a time-dependent Hamiltonian $H$. The second term with the coefficient matrix $h_{n,m}$ and the Lindblad operators $L_j$ adds any interaction of the system with the environment. For any quantum system, this term allows one to introduce relaxation and dephasing due to interaction with the environment.

With the decay rate $\gamma_1 = 1/T_1$ as coefficient and the Lindblad operator $L_1 = \hat{\sigma}_- = \frac{1}{2}(\hat{\sigma}_x - i\hat{\sigma}_y)$ and $L_1^\dagger = \hat{\sigma}_+ = \frac{1}{2}(\hat{\sigma}_x + i\hat{\sigma}_y)$ the decay of the qubit can be introduced to the dynamics of the system. Analogously, the pure dephasing time $T_{\text{pure}}$ as defined in Equation 3.7 can be added with coefficient $\gamma_2 = 1/T_{pure}$ and Lindblad operator $L_2 = \hat{\sigma}_z = L_2^\dagger$. Hence, the Master equation can be used to describe the dynamics of a multi qubit system including interaction with the environment, relaxation and dephasing of the system.

The Lindblad equation can be converted into a superoperator description as shown in (Cappellar [2012]). If the Hamiltonian $\boldsymbol{H} = -i\left(H \otimes I - I \otimes H\right)$ is time-independent,

using the generator

$$\mathcal{G} = -\sum_{m=0}^{M} \left( \bar{L}_m \otimes L_m - \frac{1}{2} I \otimes \left( L_m^\dagger L_m \right) - \frac{1}{2} \left( \bar{L}_m^\dagger \bar{L}_m \right) \otimes I \right) \tag{5.3}$$

the Lindblad equation turns into a linear equation, namely $\dot{\rho} = (\boldsymbol{H} + \mathcal{G})\rho$. This allows us to solve the Master Equation easily via

$$\rho(t) = exp[(\boldsymbol{H} + \mathcal{G})t]\rho = S(t)\rho. \tag{5.4}$$

Here, $S(t)$ is a linear superoperator on the space of density matrices and describes the evolution of state $\rho(t)$ at any time $t \geq 0$. If the Hilbert space of the system is N-dimensional, $\rho(t)$ is a $N \times N$ matrix and $S(t)$ is a $N \times N \times N \times N$ tensor. In order to simulate the CR gate pulse or even a pulse sequence, the Hamiltonian $H$ describing the pulse as well as the relaxation and dephasing times have to be plugged into Equation 5.4. The CR Hamiltonian is discussed in the following Section. If more than one pulse is applied to the system, the total superoperator can be put together piecewise whereas pulse $i$ is represented by the Hamiltonian $H_i$, which is applied for a time $T_i$

$$S = \prod_i S_i(T_i) = \prod_i exp[(\boldsymbol{H}_i + \mathcal{G})T_i]. \tag{5.5}$$

In this case, the right most superoperator refers to the first pulse applied, and the left most to the last one.

### 5.2.2 The CR Gate Hamiltonian

The two-qubit CR gate is realised by applying microwave excitations resonant with the target qubit's transition frequency directly onto the target qubit. The effective CR gate drive Hamiltonian is (Chow et al. [2011]):

$$\hat{H}_D = \Omega(t) \left( \hat{\sigma}_{x,1} + \frac{J}{\Delta_{12}} \hat{\sigma}_{z,1} \hat{\sigma}_{x,2} \right) \tag{5.6}$$

When applying the microwave with the amplitude $\Omega(t)$, the control qubit is driven off-resonantly around the x-axis. At the same time, the target qubit is driven dependent on the state of the control qubit and it is reduced by the factor of $\frac{J}{\Delta_{12}}$. Here, $J$ is the qubit-qubit coupling and $\Delta_{12}$ the qubit detuning. In the drive frame, the Hamiltonian describing the simple drive of one qubit is

$$\hat{H}'_D = \frac{\Delta}{2}\hat{\sigma}_z + \frac{\Omega_x}{2}\hat{\sigma}_x. \tag{5.7}$$

Here, $\Delta$ is the detuning of the drive from the qubit's frequency and $\Omega_x$ is the applied drive frequency. The detuning causes a rotation around the z-axis whereas the resonant drive rotates the qubit around the x-axis. In this frame, the complete Hamiltonian necessary to describe the CR gate pulse can be written as

$$\hat{H}_{CR,1} = \frac{\Delta_1}{2}\hat{\sigma}_{z,1} + \frac{\Omega_1}{2}\left(\hat{\sigma}_{x,1} + \frac{J}{\Delta_{12}}\hat{\sigma}_{z,1}\hat{\sigma}_{x,2} + S\hat{\sigma}_{x,2}\right). \tag{5.8}$$

A pulse resonant to the target qubit is applied to the control qubit. The detuning to the control qubit is $\Delta_1$. This results in a $\sigma_z$-rotation of the control qubit relative to the target one since the drive is off-resonant. $\Omega_1$ represents the drive strength of the CR pulse resulting in a $\sigma_x$ rotation of the control qubit as well as on the target qubit with a strength reduced by $J/\Delta_{12}$. Since the setup is expected to be imperfect S represents the selectivity, the fraction of drive applied to the control qubit that is also felt by the target. This results into an additional drive of the target qubit directly around the x-axis. In a perfect system with an ideal selectivity one would have no crosstalk and $S = 0$.

### 5.2.3 Gate Simulation Results

To simulate the Cross-Resonance gate, the Master Equation 5.2 can be solved for the derived Hamiltonian in Equation 5.8. Applying the derived formalism allows one to simulate the effect of a given pulse sequence onto an initial input state. By doing so, the behaviour of the CR gate is understood and tested. The total CR pulse sequence results in a $\frac{\pi}{2}$-pulse applied to the target qubit followed by the actual CR pulse applied to the

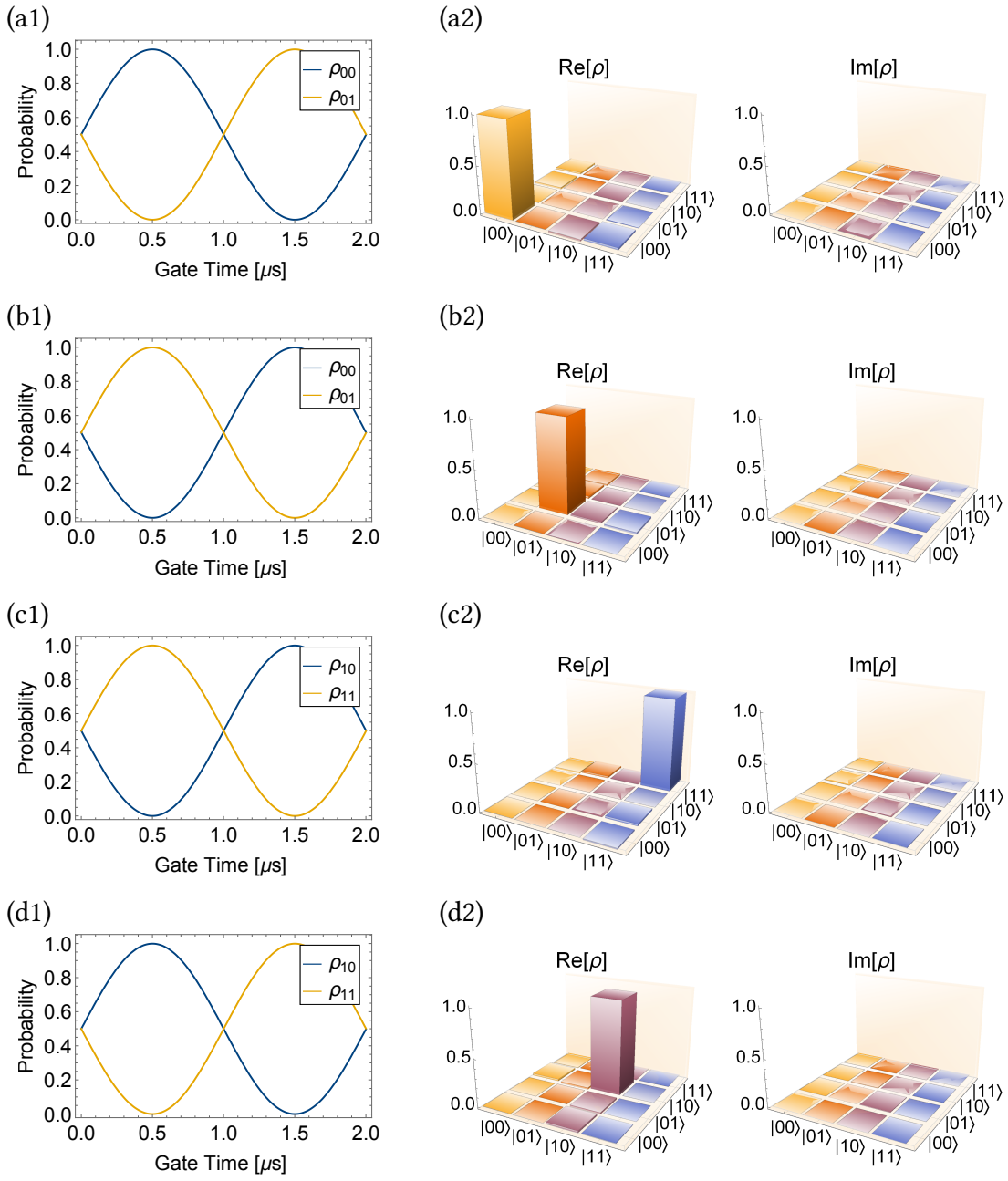


Figure 5.3: CR gate simulation without any dissipation and perfect selectivity. Each letter represents a different initial state: (a) $|00\rangle$ (b) $|01\rangle$ (c) $|10\rangle$ (d) $|11\rangle$. Column shows the probability to end in the depicted state and column 2 shows the resulting density matrices. Here, the gate time is $T_G = 0.5\,\mu s$.

control qubit. The CR pulse is a pulse of the target qubit's frequency applied on the control qubit as discussed in Section 5.1.2. The simulation result of the CR gate pulse sequence onto a two-qubit device is presented in the following.

First of all, the perfect gate is simulated. The perfect gate does not have any crosstalk (S=0) and infinite qubit lifetimes. One expects the gate to be a CNOT type gate, meaning that when the control qubit is in its ground state, the initial state is projected onto itself. In contrast to this, when the control qubit is excited, the state of the target is flipped after the gate is applied.

The results are presented in Figure 5.3.They prove the working principle of the CR gate. For this simulation the coupling J is set to be $40\,\mathrm{MHz}$ and the qubit-qubit detuning is $250\,\mathrm{MHz}$. Each row presents the results of the gate on different input states. In (a), $|00\rangle$ is the input state, (b) refers to $|01\rangle$ as input, (c) to $|10\rangle$ and (d) shows the results for the input $|11\rangle$. In column 1, the probability to end in the labelled state after the gate is plotted as a function of the gate time. Note, that the $\frac{\pi}{2}$-pulse necessary to perform the CR gate is applied beforehand. The second column shows the real and imaginary part of the density matrix at the gate time $T_G$ =0.5 µs. For example, (a1) shows that the target qubit population oscillates. After $0.5\,\mu$s, the state has returned to the ground state, meaning that $|00\rangle$ goes back to $|00\rangle$. In (b1), the input state is $|01\rangle$. After $0.5\,\mu$s, the output is the same as the input. In both cases so far, the control qubit was in its ground state, so the target qubit is expected not to change its state after the gate. In contrast to this, the last two rows show the opposite. Now, the first qubit is excited, so the target qubit is expected to flip. This is proven in (c1), where after the $0.5\,\mu$s gate time, the state then is $|11\rangle$. For the input $|11\rangle$ in (d1), the expected output $|10\rangle$ is verified in the plot. For each input state the output density matrix after the gate time $0.5\,\mu$s again verifies the CNOT behaviour.

The gate fidelity can be determined by the definition of the fidelity

$$\mathcal{F}(\rho,\sigma) = \mathrm{Tr}\left[\sqrt{\sqrt{\rho}\sigma\sqrt{\rho}}\right] \tag{5.9}$$

given two matrices $\rho$ and $\sigma$. This corresponds to a comparison of the two matrices $\rho$ and $\sigma$. In case of $\rho = \sigma$, the fidelity reaches its maximum of 1. To find the fidelity for a given

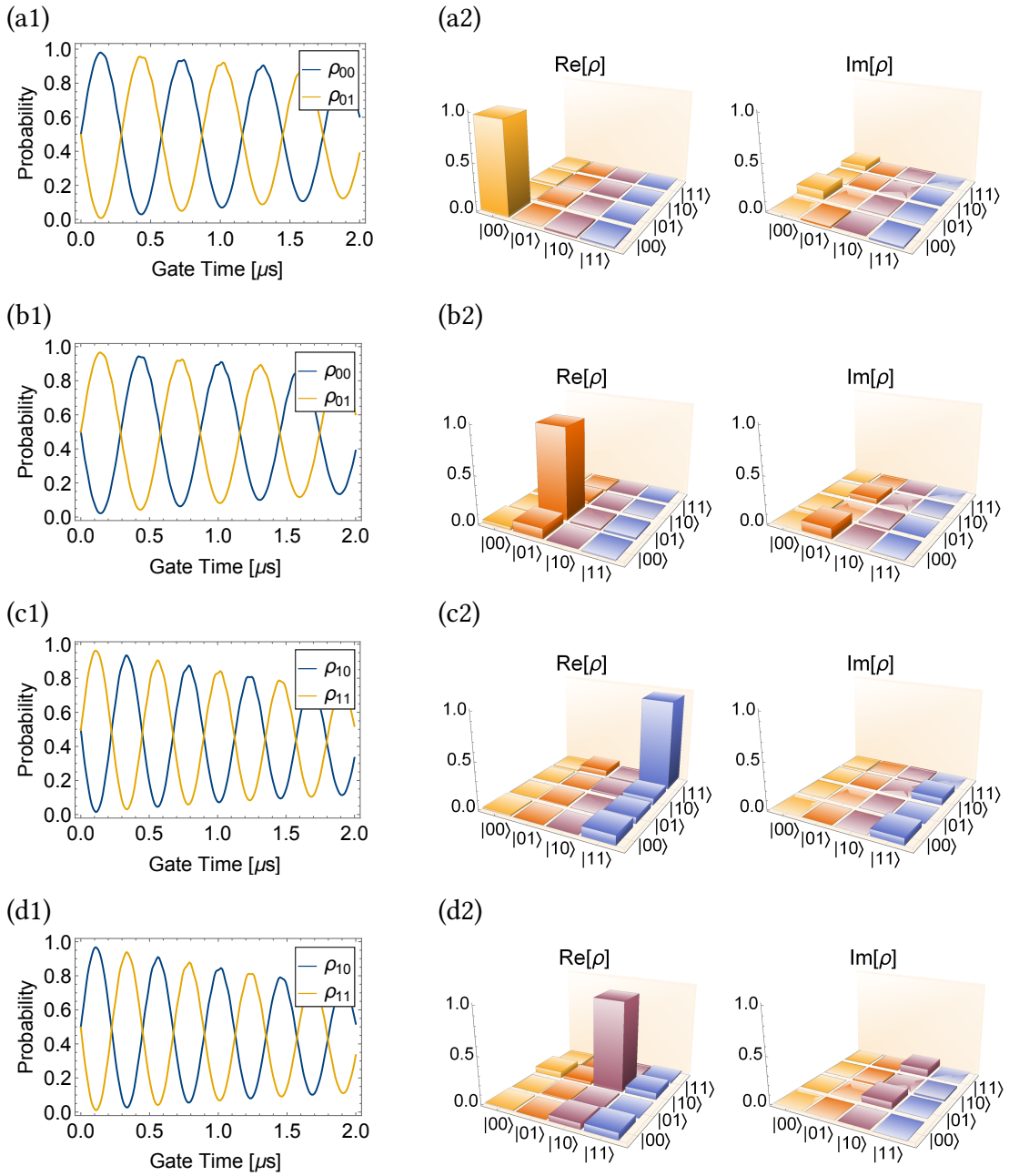


Figure 5.4: CR gate simulation results including dissipation and imperfect selectivity. Each letter represents a different initial state: (a) $|00\rangle$ (b) $|01\rangle$ (c) $|10\rangle$ (d) $|11\rangle$. column 1 shows the probability to end in the depicted state and column 2 shows the resulting density matrices. Here, the gate time is $T_G = 0.125\,\mu s$.

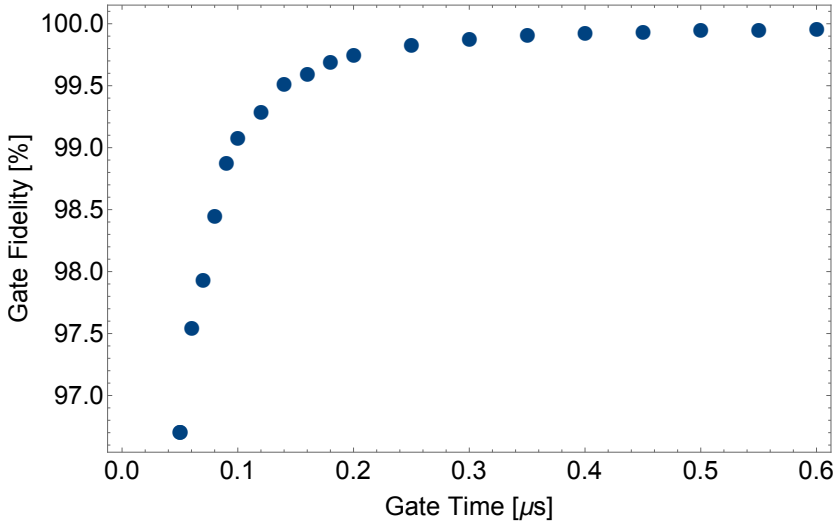


Figure 5.5: CR gate fidelity for the four input states $|00\rangle$, $|01\rangle$, $|10\rangle$ and $|11\rangle$ as a function of gate time for infinite qubit lifetimes and perfect selectivity $S = 0$. Small gate times decrease the fidelity due to a finite drive strength. For longer gate times, the fidelity converges to $\mathcal{F} = 100\%$.

input state, the simulated output matrix has to be compared to its ideal output. For the Cross-Resonance gate as a CNOT type gate, $|00\rangle$ ideally is projected onto itself, same is valid for $|01\rangle$. In contrast to this, the simulated output matrix for the input state $|10\rangle$ has to be compared to $|11\rangle$. This then gives the fidelity for the input state $|10\rangle$. For the case of $|11\rangle$ as input, the ideal output is $|10\rangle$.

Using Equations 5.9, the CR gate fidelity can be calculated for any input state. For the ideal case of perfect selectivity and infinite qubit lifetimes, the fidelities for the four input states $|00\rangle$, $|01\rangle$, $|10\rangle$ and $|11\rangle$ are the same and the result is plotted in Figure 5.5. For small gate times of $T_G < 0.2\,\mu s$, the fidelity rapidly increases and for $T_G > 0.2\,\mu s$ it converges to 100%. The reason of the decrease in fidelity for short gate times is the finite drive speed of the rotation. In this example, a gate time of $T_G = 0.6\,\mu s$ results in a fidelity of $\mathcal{F} = 99.97\%$. A faster drive could allow shorter gate times for the same fidelity. However, as discussed in Section 5.1.2 the small drive limit must remain fulfilled.

So far, this simulation gives a proof of principle. It is more interesting to determine the effect of finite qubit lifetimes and imperfect selectivity onto the gate and its fidelity. Therefore, the lifetimes of the current two-qubit device are used. Qubit 1 has a $T_1 = 13.28\,\mu s$

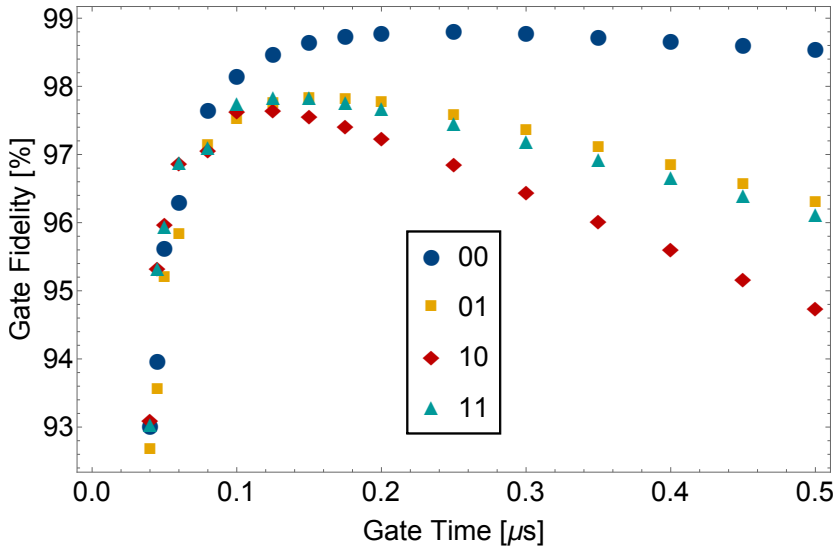


Figure 5.6: CR gate fidelity for the input states $|00\rangle$, $|01\rangle$, $|10\rangle$ and $|11\rangle$ as a function of gate time. The first number represents the state of the control qubit and the second the target qubit. The target qubit lifetimes are $T_1^{(t)} = 13.28\,\mu s$, $T_2^{(t)} = 6.75\,\mu s$ and $T_1^{(c)} = 8.76\,\mu s$, $T_2^{(c)} = 5.1\,\mu s$ for the control qubit, and the selectivity is set to $S = 2\%$. Short gate times exhibit small fidelities due to the finite drive strength of the rotations. The fidelity of long gate times decreases because of the finite qubit lifetimes.

and $T_2 = 6.75\,\mu s$, whereas qubit two exhibits $T_1 = 8.76\,\mu s$ and $T_2 = 5.1\,\mu s$. A selectivity of $S = 2\%$ (Section 5.4) is assumed while the coupling J and the detuning $\Delta_{12}$ were kept the same as in the perfect gate simulation. Again, the results are presented in Figure 5.4. As before, the letter A-D present the different input states $|00\rangle$, $|01\rangle$, $|10\rangle$ and $|11\rangle$. Column 1 shows the probability to end in the labelled state as a function of the gate time. Going through each input and output state as before, it becomes clear, that the CR gate acts as a CNOT gate. The added decoherence damps the state probability as visible in the plots.

Optimisation of the CR gate time can be performed by varying the gate time and maximizing the fidelity. This process is shown in Figure 5.6. For short gate times, the same argument as before applies. A finite speed of $J/\Delta_{12}$ of the target qubit's rotation due to the CR gate limits the fidelity. Fidelities for long gate times decrease due to finite qubit lifetimes. This means that for each drive strength as well as set of qubit lifetimes the gate time has to be optimised individually.

### 5.2.4 Optimising the Gate Fidelity

The gate fidelity can be optimised in several ways. First of all, increasing the qubits' lifetimes and optimising the selectivity increases the gate fidelity. Furthermore, the ratio $J/\Delta_{12}$ could be varied to see whether this results in a better sweet spot when varying the gate times as shown in Figure 5.6. Increasing this ratio in order to decrease gate times is a trade-off with the requirement of still being in the weak-coupling limit where $J \ll |\omega_2 - \omega_1| = \Delta_{12}$. Lastly, the gate fidelity can be improved by correcting for the imperfect selectivity. By applying a cancellation pulse to the target qubit, the unwanted rotation of the target qubit due to bad selectivity can be cancelled out. The needed amplitude is decreased by the selectivity $S$ compared to the CR pulse amplitude. This in turn, again leads to unwanted influence on the target qubit. However, this second-order effect now is only proportional to $S^2$. In the best case, this cancellation pulse is applied simultaneously to the CR gate itself to keep the control qubit corrected at all times and to not increase the overall gate time.

The gate simulation using the superoperator formalism to solve the Master Equation works well. For finite lifetimes and imperfect selectivities, the gate and its fidelity can be simulated and further optimised. However, optimising the fidelity including cancellation and other optimisation pulses cannot be easily simulated in this way. These techniques require simultaneous pulses at different frequencies such that the total gate time does not increase resulting in a decrease of fidelity due to decoherence. Further, it is the best to correct for the imperfect selectivity simultaneously to prevent error propagation. To do so, time-dependent Hamiltonian would need to be simulated.

## 5.3 The Coupled Coaxmon Design

The advantage of having the 2D plane free on the chip can now be exploited to couple to a second qubit. Naively, the first idea is to simply copy a second coaxmon next to the first one. However, simulations show that even at the closest possible separation of

(a)

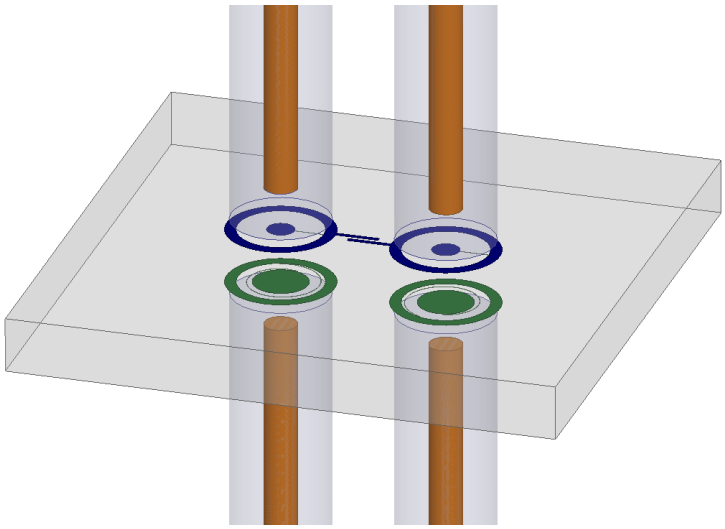

(b)

| | Aim |
|---|---|
| $f^1_{res}$ [GHz] | 9.5 |
| $f^2_{res}$ [GHz] | 10.5 |
| $f^1_{01}$ [GHz] | 7.0 |
| $f^2_{01}$ [GHz] | 7.5 |
| $\Delta$ [MHz] | 500 |
| g [MHz] | $\approx 300$ |
| J [MHz] | $\approx 18$ |
| J/$\Delta$ | 0.04 |

Figure 5.7: (a) Design of the two coupled coaxmons. Additional capacitance arms give the necessary coupling. (b) Aimed coupled coaxmons parameters.

$a = 1.5\,\mathrm{mm}$, which is limited by the wiring on top of the sample holder, the qubits do not couple strongly enough. This is why the capacitance between the qubits is increased by introducing arms to the qubits. The double coaxmon design including these arms is shown in Figure 5.7 (a). This picture again is taken from the HFSS simulations. Of course, the qubit frequencies and resonator frequencies are adjusted as well to give non-degenerate frequencies. This is simply done by adjusting the Josephson junction area as well as the resonator inductor length.

The aimed parameters fulfilling all requirements for the CR gate are listed in Figure 5.7 (b). The resonator frequencies are aimed to be within the range of the $8\,\mathrm{GHz}$ to $12\,\mathrm{GHz}$ band pass filter on the output line in the experiment. The qubit frequencies are chosen to be smaller than the resonator such that the higher levels of the qubit are even smaller in frequency and not interfere with the resonators. The qubit-qubit coupling $J$ and detuning $\Delta_{12}$ are chosen to have a ratio of $0.04$, following a previous successfull realisation of the CR gate in (Chow et al. [2011]). At last, the qubit-resonator coupling $g$ is not changed from the single coaxmon device since it proved to exhibit a good coupling. The exact way of adjusting the capacitance arms to result in the aimed qubit-qubit coupling is explained in Section 5.3.2. At first, the lumped element model is extended to two qubits and then

(a)

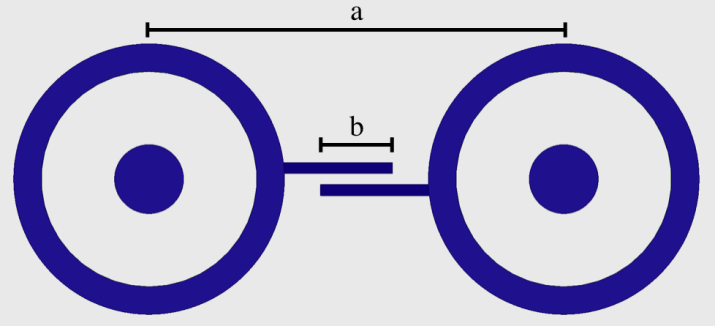


(b)

| b [mm] | J [MHz] | S [%] |
|---|---|---|
| no arms | 0.4 | 0.11 |
| -0.4 | 0.5 | 0.14 |
| -0.2 | 1.3 | 0.25 |
| 0.0 | 3.5 | 0.51 |
| 0.15 | 7.7 | 0.98 |
| 0.24 | 9.5 | 1.16 |
| 0.36 | 12.8 | 1.48 |
| 0.44 | 15.9 | 1.73 |
| 0.5 | 19.2 | 2.00 |

Figure 5.8: a) The coupling capacitance is characterised as a function of the overlap b of the two arms. The arms are $0.04\,\mathrm{mm}$ wide and the qubit-qubit distance is a. b) The coupling capacitance affects the qubit-qubit coupling strength J and the selectivity S, here $a = 1.5\,\mathrm{mm}$.

the capacitance is adjusted iteratively by simulating the capacitances and calculating the coupling via the lumped element model.

As presented in Section 3.7, HFSS and the black-box quantisation model is theoretically also able to calculate the parameters of interest for multi-qubit devices. However, it turns out, that already for the two-qubit case, HFSS exceeds the available calculation power. Therefore, the lumped element model is used in the following. Nevertheless, if computing power is available, HFSS is expected to give good results as comparison of HFSS and the lumped element model already showed good agreement in the case of a single coaxmon.

### 5.3.1 The Lumped Element Model for the Coupled Coaxmon

The lumped element model introduced in Section 4.7 can also be applied to the coupled coaxmons. To do so, the extended electric circuit for two coaxmons has to be considered. The single coaxmon circuit, as shown in Figure 4.12 has to be duplicated such that all islands are capacitively coupled with each other. Analogously to the single device, the Hamiltonian of the coupled coaxmons can be derived allowing to determine the qubit-qubit coupling from the capacitance matrix of the system. This is used to adjust in qubit-qubit coupling strength in the following Section.

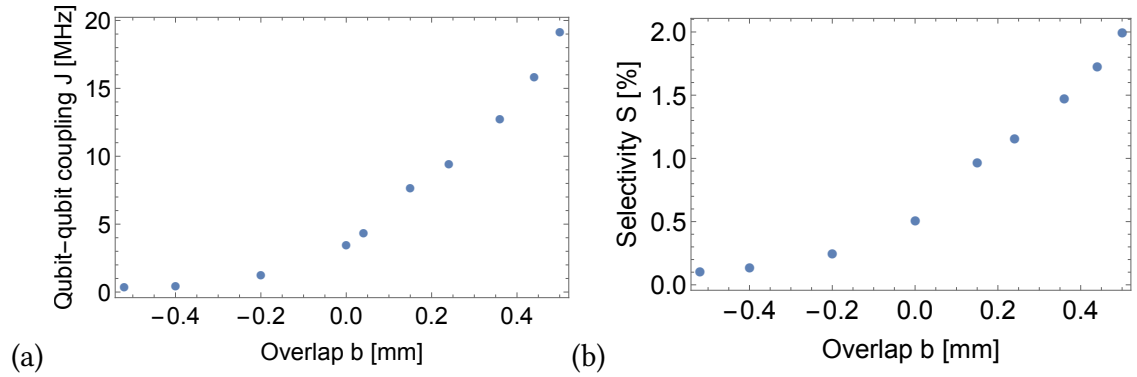


Figure 5.9: (a) The qubit-qubit coupling strength $J$ as a function of the overlap b. (b) The selectivity S as a function of the overlap $b$.

### 5.3.2 The Qubit-Qubit Coupling Strength

In order to obtain the desired qubit-qubit coupling strength the additional capacitance arm lengths are adjusted iteratively. The capacitances are simulated with Maxwell and the qubit-qubit coupling $J$ is calculated with the lumped element model. The aim for the qubit-qubit coupling is $J \approx 18\,\mathrm{MHz}$ in order to maintain the aimed ratio $J/\Delta_{12} \approx 0.04$ together with $\Delta_{12} = 250\,\mathrm{MHz}$. The arms are adjusted such that the aimed coupling strength is realised. Figure 5.8 (a) shows the qubits from the top. Distance $a$ equals $1.5\,\mathrm{mm}$ and is the closest distance possible due to the wiring constraints outside the sample holder. Length b represents the overlap of the additional capacitance arms which is varied. A negative value means that the arms are not yet overlapping. Both arms are $0.04\,\mathrm{mm}$ wide. The results for the qubit-qubit coupling strengths are listed in Figure 5.8 (b) and the values are plotted in Figure 5.9 (a). To obtain the desired coupling strength of about $18\,\mathrm{MHz}$, an overlap of $0.47\,\mathrm{mm}$ is estimated.

## 5.4 Selectivity

The selectivity of a multi qubit device represents how well one qubit can be addressed without interfering with the others at the same time. In this thesis, the selectivity is defined as the ratio of amplitude drop across the target qubit when a voltage is applied

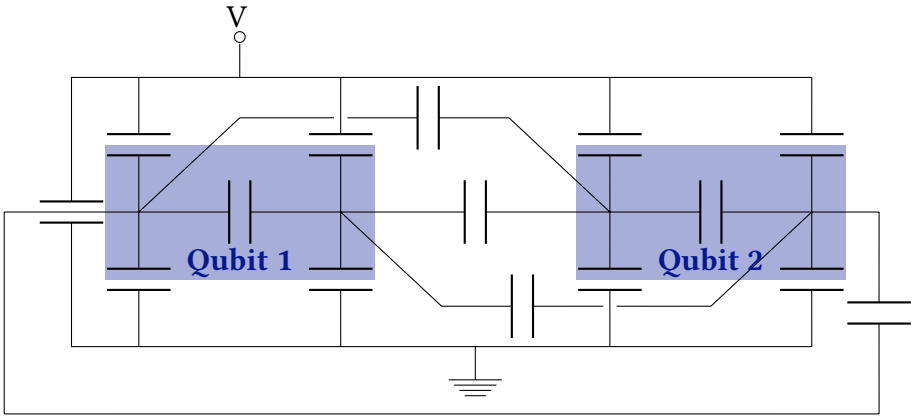


Figure 5.10: The simplified circuit of two coupled coaxmons for the selectivity estimation. A voltage is applied to the qubit pin of qubit one, and the capacitances in between the two qubits are taken into account in order to estimate the selectivity corresponding to the ratio of voltage drop across qubit two and across qubit one.

to the control qubit. This means that a small number S stands for a well selective setup and its range goes from zero to one. The selectivity is important due to the fact that a non-selective drive disturbs the perfect gate Hamiltonian as described in Section 5.2.2. This is why, the selectivity of the coupled coaxmons is simulated using the network analysis introduced in Section 4.8 for the network presented in Figure 5.10. To estimate the selectivity, the double coaxmon circuit is simplified to only consider the qubit islands and the control pin of qubit one as well as the ground represented by the sample holder. A whole circuit analysis would require taking into account thirteen islands resulting into 78 capacitances and a corresponding number of coupled equations. With the assumption, that the main contribution to the selectivity comes from the just introduced additional capacitance, only the qubits, the control pin of qubit one and the ground are considered here.

The resulting values for the qubit selectivity are listed in Figure 5.8 (b) and plotted in Figure 5.9 (b). No arms allow a selective addressing of $0.11\,\%$ and even with the additional capacitance to achieve a qubit-qubit coupling strength of $18\,\mathrm{MHz}$, only a selectivity of $S = 2\%$ is estimated. Thus, the design is chosen to be as presented in Figure 5.8 (b) with an overlap of $b = 0.47\,\mathrm{mm}$. The device can now be fabricated with confidence on the estimated parameters.

# 6 Experiments on the Coupled Coaxmons

In this Chapter, the experiments on the first coupled coaxmons are presented. First of all, a description of their fabrication procedure is given in Chapter 6.1 and the measurement setup is described in Section 6.2. The first measurements on the coupled coaxmon device are a basic characterisation of each coaxmon performed by treating each of them as a single coaxmon. This gives an overview of the device parameters as presented in Chapter 6.3. Following this, the qubit-qubit interactions are investigated. A coupling strength measurement is presented in Section 6.4 and the result is compared to simulation. Afterwards in Section 6.5, the selectivities of the coupled and uncoupled coaxmons are measured and compared to simulation. Finally, a conclusion on the experiments of the first coupled coaxmons is given in Section 6.6.

## 6.1 Fabrication

Fabrication of all devices is carried out by another member of the group. A detailed description can be found in (Peterer [2016]) or (Rahamim [2016]). Here, only a short summary is given. The coaxmon is fabricated in two steps using electron-beam lithography. At first, the whole resonator is fabricated on one side of a sapphire chip with a straight, one-angle evaporation of aluminium. After flipping the chip, the qubit is fabricated on the other side of the chip. In contrast to the resonator, the qubit is fabricated with a double-angle evaporation using the Dolan-bridge technique in order to create the Josephson junction.

Fabricating the qubit and resonator on each side follows a similar recipe. First of all, the chip is cleaned with acetone and dimethyl sulfoxide (DMSO). While the resonator can be cleaned with accetone in an ultrasonic bath, this is not possible for the qubit side anymore

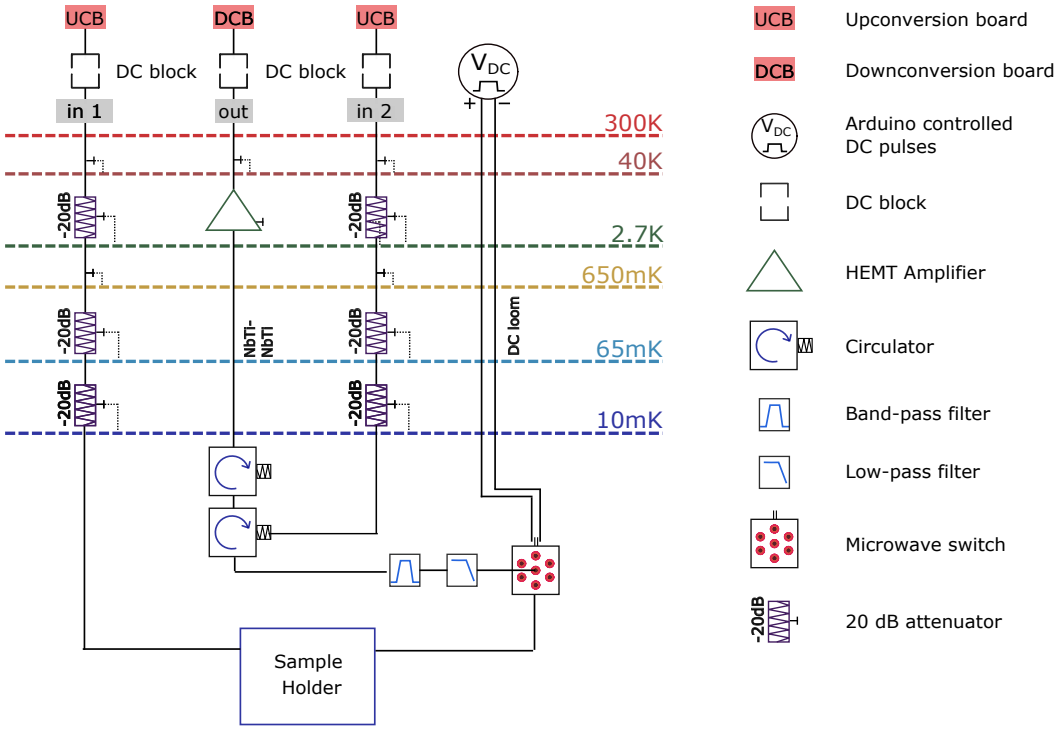


Figure 6.1: The experiment setup. Figure adapted from (Peterer [2016]). The input signal is attenuated by 60 dB before reaching the sample to prevent room-temperature noise getting to the device. The output signal is filtered and amplified at the 3 K stage. Measuring in transmission means sending the signal through input line 1, whereas reflection measurements are performed with the input line 2. The drawing shows the setup for a single qubit measurement. For the four qubit sample, four input lines 'in1' are implemented. Two output lines 'out' and two input lines 'in2' allow one to measure two qubits simultaneously. A microwave switch on each of the output lines allows one to choose all four qubits, coupled pairs are placed on separate output lines to allow simultanous measurement.

since at that point the resonator is already on the chip and a sonictron would damage the circuit. Afterwards, the chip is spin-coated with two layers, one of copolymer and one of polymethyl methacrylate (PMMA) photoresist. Next, the electron-beam lithography is carried out to pattern the chip with the circuit. In the development, the exposed resist is then removed with a 1:3 mixture of methyl isobutyl ketone (MIBK) and isopropyl alcohol (IPA) and then pure IPA. An evaporation of $80\,\mathrm{nm}$ aluminium onto the whole chip follows to create the circuit layer. A following lift-off step with hot acetone removes all remaining photoresist including the aluminium on top. Only where the aluminium is sitting directly on the chip, the aluminium stays. Since this is exactly where the e-beam patterned the circuit, only the latter remains. In order to not damage the already fabricated resonator while fabricating the qubit, the chip is sitting on top of washers or specially designed sample holders to protect the bottom side.

## 6.2 The Measurement Setup

All experiments are carried out in a dilution refrigerator at about $10\,\mathrm{mK}$. This low temperature is not only needed to reach the superconducting phase of aluminium, which is below $T_c = 1.2\,\mathrm{K}$, but it is also required to reduce the thermal noise below the frequency of the qubit's ground to excited state transition, namely $\hbar\omega \gg k_B T$. For a qubit with $\omega \approx 2\pi \times 10\,\mathrm{GHz}$ this gives $\frac{\hbar\omega}{k_B} \approx 0.5\,\mathrm{K}$, which is one order of magnitude larger than the fridge temperature of $10\,\mathrm{mK}$. The experimental setup is illustrated in Figure 6.2. All drives and pulses are generated by signal generators modulated by a field programmable gate array (FPGA). Through coaxial cables they are then connected to the devices inside the dilution refrigerator. To prevent room-temperature noise reaching the qubit, the signal is attenuated by about $60\,\mathrm{dB}$. On the way out, bandpass filters and circulators cut off noise and amplifiers at the cryogenic and room temperature amplify the signal by about $70\,\mathrm{dB}$. The signal is then measured by an analogue to digital converter (ADC). Experiments can be performed in either transmission or reflection. In the first case the qubit and resonator pulse both are applied to input line 1 and the resonator is read out via the output line. For reflection measurements, line 2 is used as input for the resonator

(a) 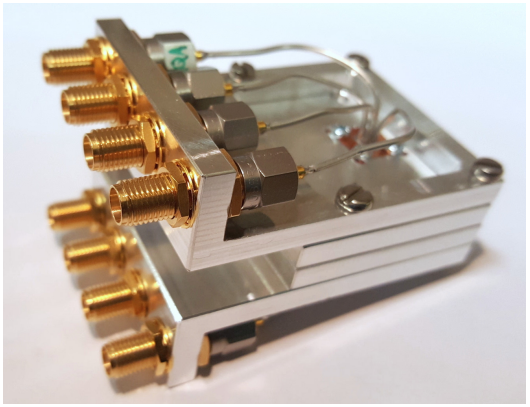 (b) 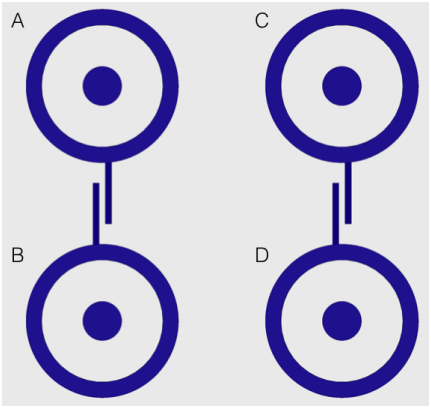


Figure 6.2: The coupled coaxmon (a) sample holder and (b) chip. A and B form a coupled pair, same as C and D. A and C have the same centre-to-centre distance as C and D but are not intentionally coupled, same holds true for B and D.

pulse and a circulator allows one to also read out via the output line. The qubit pulse is still applied to the input line 1 in reflection measurements.

## 6.3 Basic Characterisation of the Coupled Coaxmons

Two pairs of coupled coaxmons were fabricated onto one sapphire chip. As depicted in Figure 6.2, A and B form an intentionally coupled pair, same as for C and D. The estimated selectivity of $S = 0.1\%$ and qubit-qubit coupling of $J = 0.4\,\mathrm{MHz}$ for uncoupled pairs allows one to put two coupled pairs on one chip. Furthermore, this experiment allows one to experimentally verify the simulated numbers for selectivity and qubit-qubit coupling for the coupled and uncoupled case. The centre-to-centre distance is $a = 1.5\,\mathrm{mm}$ as defined in Figure 5.8 for both coupled and also uncoupled pairs A-C and B-D. In the following, a basic characterisation of coaxmons C and D is presented, as A and B turn out to be only detuned by $129\,\mathrm{MHz}$ whereas the goal was $500\,\mathrm{MHz}$. Furthermore, the qubit lifetimes are only of the order of $1.5\,\mu\mathrm{s}$. For the basic characterisation both coaxmons are measured by treating them as a single qubit-resonator device. All coaxmon parameters gained through the following measurements are listed in Table 6.1.

First of all, a resonator sweep is performed to determine the resonator frequency and its quality factor. A single continous drive from a microwave signal generator is applied and

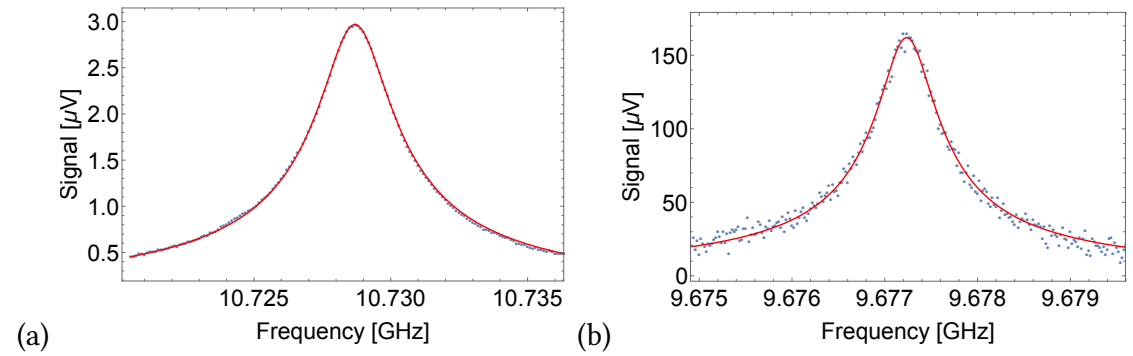


Figure 6.3: Resonator frequency sweep for (a) coaxmon C at a drive power of $-35\,\mathrm{dBm}$. A Lorentzian fit (red) gives $f_R^C = 10.7278\,\mathrm{GHz}$ and a quality factor of $Q = 4102$. (b) Resonator sweep for coaxmon D at a drive power of $-60\,\mathrm{dBm}$. The Lorentzian fit (red) gives $f_R^D = 9.6772\,\mathrm{GHz}$ and a quality factor of $Q = 15500$.

swept while the transmission signal is measured. Figure 6.3 shows the resonator sweeps of coaxmon C and D in transmission. Each point is an average of many experiments. Fitting a Lorentzian allows one to find the resonator frequencies to be $f_R^C = 10.7278\,\mathrm{GHz}$ and $f_R^D = 9.6772\,\mathrm{GHz}$ with quality factors $Q_C = 4102$ and $Q_D = 15500$ respectively. A linear response of the resonator for coaxmon C is possible at -35dBm, whereas coaxmon D needs a lower power of -60dBm. Linearity of the resonator response ensures to be in the small drive regime. Due to the lower power measurement of resonator D, the noise is higher even though the number of averages is increased relative to C.

In the following measurements, the dispersive readout of the qubit is used. The dispersive readout allows one to measure the state of the qubit by measuring the resonator frequency. In the dispersive regime (Equation 3.9), the resonator shifts by $-2\chi$ when the qubit is excited in comparison to when it is in the ground state. Exploiting this, qubit spectroscopy of each coaxmon is performed. While a single tone is sent to read out the resonator, the second drive close to the frequency of the qubit is swept. This allows spectroscopy of the qubit transitions. From this measurement onwards, the resonators are measured in reflection. In the setup this means, that the resonator drive is applied through the resonator pin from which it is also read out, without interfering with the qubit. And the qubit drive is directly applied to the qubit pin. The spectroscopy of qubit C is shown in Figure 6.4. Figure 6.4 (a) presents the qubit spectroscopy at varying qubit

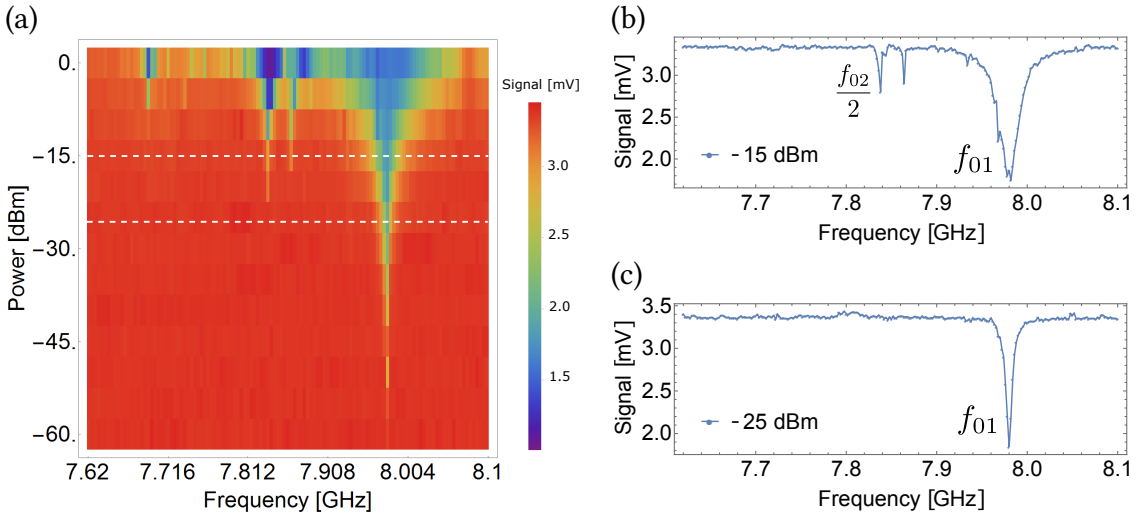


Figure 6.4: Qubit spectroscopy of coaxmon C. (a) Power-dependent spectroscopy. (b) Single trace at $-15\,\mathrm{dBm}$ showing the $f_{01}$ and $\frac{f_{02}}{2}$ transition. (c) Low power trace at $-25\,\mathrm{dBm}$ showing only the ground to first excited state transition $f_{01}$.

drive powers. For low drive powers, only the ground to first excited state transition $f_{01}^C$ is driven as can be seen in the extracted single trace at $-25\,\mathrm{dBm}$ in Figure 6.4 (c). For higher powers, the two photon transition $\frac{f_{02}^C}{2}$ is additionally driven as it can be seen in Figure 6.4 (b) for $-15\,\mathrm{dBm}$. At even higher powers at $0\,\mathrm{dBm}$, a third dip arises on the left of $\frac{f_{02}^C}{2}$, which refers to the three-photon transition $\frac{f_{03}^C}{3}$. From these measurements, the mentioned transition frequencies can be determined as they are listed in Table 6.1. Furthermore, as $-\alpha_C = f_{01}^C - f_{12}^C = 2(f_{01}^C - \frac{f_{02}^C}{2})$, the anharmonicity of the qubit can be determined to be $-285.8\,\mathrm{MHz}$.

An interesting observation in the spectroscopy is the additional dip at $f_X = 7.864\,\mathrm{GHz}$, $26\,\mathrm{MHz}$ (at $-15\,\mathrm{dBm}$) above the $\frac{f_{02}^C}{2}$ dip. As the frequency of a qubit does not shift with qubit drive power, it can be excluded to be the $\frac{f_{02}^C}{2}$ transition. Apart from that, the two-photon transition $\frac{f_{02}^C}{2}$ arises about half way between the $f_{01}^C$ and $\frac{f_{03}^C}{3}$ transition. This holds true for the already identified $\frac{f_{02}^C}{2}$ peak. Missing so far is an explanation for this additional dip at frequency $f_X$. Presumably, it refers to a two qubit interaction.

Qubit spectroscopy is performed also for coaxmon D and is shown in Figure 6.5. Figure 6.5 (a) is the power-dependent qubit spectroscopy. Two traces for high ($-15\,\mathrm{dBm}$) and low

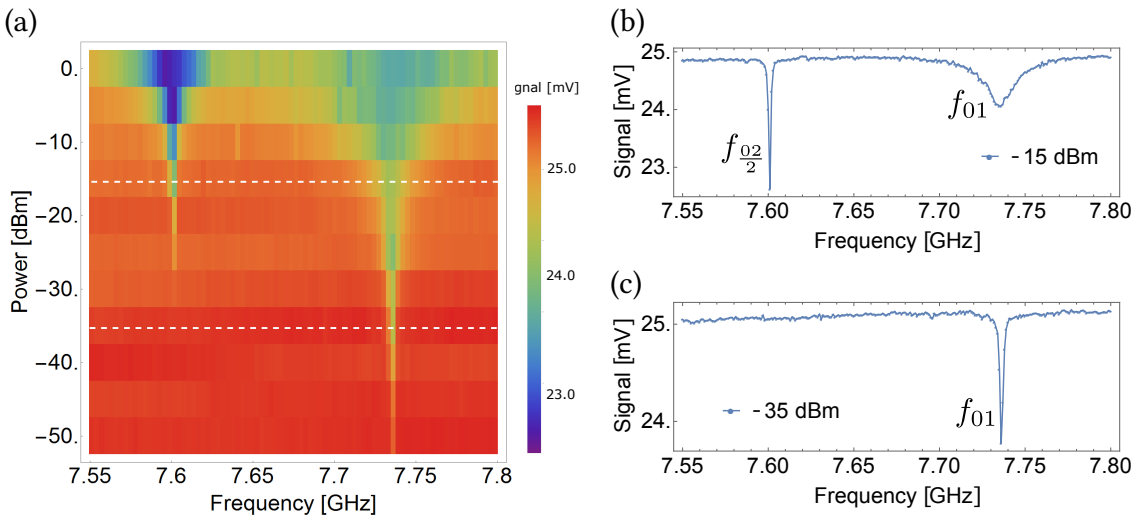


Figure 6.5: Qubit spectroscopy of coaxmon D. (a) Power-dependent spectroscopy. (b) single trace at $-15\,\mathrm{dBm}$ showing the $f_{01}$ and $\frac{f_{02}}{2}$ transition. (c) Low power trace at $-35\,\mathrm{dBm}$ showing only the ground to first excited state transition.

($-35\,\mathrm{dBm}$) power are plotted in Figures 6.5 (b) and (c). For low power, only the ground to first excited state transition $f_{01}^D$ is driven. Higher power also excites the two-photon transition $\frac{f_{02}^D}{2}$. this gives an anharmonicity of $\alpha_D = -270\,\mathrm{MHz}$ for coaxmon D.

In order to understand the presence of the dip in the spectroscopy of coaxmon C, it is useful to draw the level diagram of the two qubits as illustrated in Figure 6.6. The frequency $f_X$ does not match a frequency of the coupled qubit D. However, the spectroscopy of D shows, that $f_{01}^D$ differs only by $40\,\mathrm{MHz}$ from $f_{12}^C$. A possible explanation for the unidentified dip could be that for high driving powers the two-photon transition at $(f_{01}^D + f_{01}^C)/2 = 7.858\,\mathrm{GHz}$ can be driven. However, in this calculation the airising shift in the qubit frequency due to the coupling to another qubit is neglected. To clarify the nature of $f_X$ to experiments could be performed. First, a two tone spectroscopy would allow one to identify if the transition is a two-photon process. In this case, two qubit drives of the same frequency are applied to the qubit. Sweeping these qubit frequencies simultaneously allows one to assign all transitions to single-, two- or more photon processes. Alternatively, the qubit spectroscopy in Figure 6.5 could be repeated including frequencies up to $f_X$. If $f_X = (f_{01}^D + f_{01}^C)/2$, then the transition must be visible

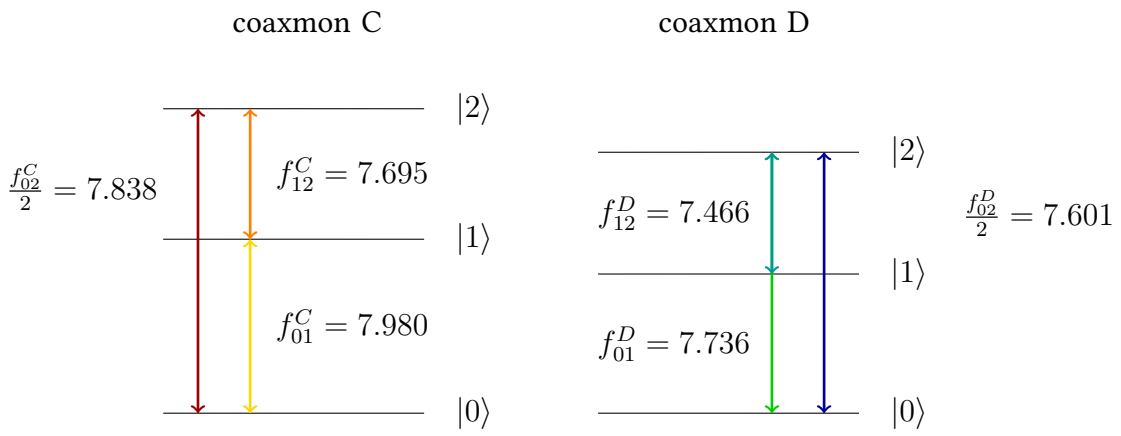


Figure 6.6: Energy level diagram for the coupled coaxmons C and D. All frequencies in GHz. Note, that $f_{12}^C$ and $f_{01}^D$ are only detuned by $41.4\,\mathrm{MHz}$.

in both qubit spectroscopies, coaxmon C and D. However, due to the fact that the nature of the additional dip $f_X$ is not important in the following, these measurements are not performed at this point.

With the knowledge of the qubit frequencies it is possible to measure the $\chi$-shift because the resonator frequency shifts by $-2\chi$ when the qubit is excited to its first excited state. Hence, by measuring the resonator, the qubit state can be concluded. The measurements of the $\chi$-shifts are presented in Figure 6.7. Figure 6.7 (a) shows the $\chi$-shift of qubit C. In this case, the qubit is excited continuously. A continuous drive saturates the excited qubit state with a maximum of 50% probability, while the rest remains in the ground state, hence two resonator peaks are visible, separated by $2\chi_C = 8.78\,\mathrm{MHz}$. The different depths of the dips mean that the ground and first excited state are not populated by the same amount. This is due to not fast enough driving of the qubit; as while driving, the qubit is already decaying.

Alternatively, the $\chi$-shift can be measured once the $\pi$-pulse length is known after a Rabi-experiment. In this case, the qubit can be fully excited such that the resonator peak appears shifted completely for many averaged data points. This is how the $\chi$-shift is measured for coaxmon D in Figure 6.7 (b) resulting in $2\chi_D = 14.37\,\mathrm{MHz}$.

As the Hamiltonian in Equation 3.9 shows, the qubit frequency also shifts linearly with the number of photons in the resonator. Each extra photon $n = a^\dagger a$ in the resonator

| | Coaxmon C | Error on C | Coaxmon D | Error on D |
|---|---|---|---|---|
| $f_{res}$ [GHz] | 10.7288 | 0.0001 | 9.6772 | 0.0001 |
| $f_{01}$ [GHz] | 7.980 | 0.001 | 7.736 | 0.001 |
| $\Delta/(2\pi) = (f_{01} - f_{res})$ [GHz] | 2.749 | 0.001 | 1.941 | 0.01 |
| $f_{12}$ [GHz] | 7.695 | 0.001 | 7.466 | 0.001 |
| $\frac{f_{02}}{2}$ [GHz] | 7.838 | 0.001 | 7.601 | 0.001 |
| $E_C$ [MHz] | 285.8 | 1.4 | 270.0 | 1.4 |
| $2\chi/(2\pi)$ [MHz] | 8.78 | 0.36 | 14.37 | 2.9 |
| $g/(2\pi)$ [MHz] | 356 | 7 | 338 | 7 |
| $T_1$ [µs] | 4.73 | 0.08 | 7.27 | 0.08 |

Table 6.1: Experimental parameters of the coupled coaxmon C and D.

shifts the qubit frequency by $-2\chi$ and this is referred to as number splitting. This kind of $\chi$-shift measurement is performed for coaxmon D and it is shown in Figure 6.7 (c), yielding the same value for $\chi_D$ as from b).

With the knowledge of the qubit frequencies, Rabi oscillation can be measured to first of all show the two level dynamics and to further determine the $\pi$-pulse length. The Rabi pulse sequence is a qubit pulse of varying length directly followed by a measurement pulse of the resonator. The measured Rabi oscillations are presented in Figure 6.8 with a damped sinusoidal fit in red. Driving coaxmon C at $-5\,\mathrm{dBm}$ results in a Rabi frequency of $33.96\,\mathrm{MHz}$. And driving coaxmon D at $0\,\mathrm{dBm}$ gives a Rabi frequency of $68.84\,\mathrm{MHz}$.

A $\pi$-pulse now allows one to measure the lifetime $T_1$ of the qubits. At first, the qubit is fully excited and after a variable length of waiting time, the measurement pulse follows. With an increase of the delay of the measurement pulse, the probability of the qubit to decay to its ground state increases. This $T_1$ measurement for both qubits C and D is presented in Figure 6.9. The data is fitted with an exponential decay as shown by the red line in the plots. The lifetime of coaxmon C is determined to be $T_1^C = 4.7\,\mu\mathrm{s}$ and $T_1^D = 7.3\,\mu\mathrm{s}$ for coaxmon D.

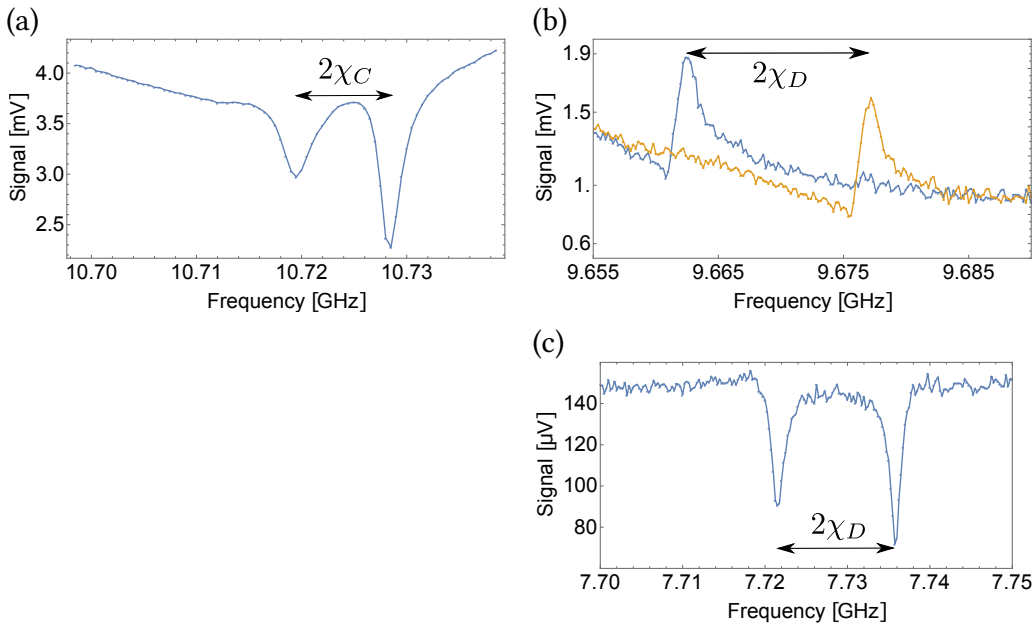


Figure 6.7: $\chi$-shift measurements for coaxmon C and D. (a) Continuously driving coaxmon C shifts the resonator by $2\chi$ and two peaks appear. Measurement in reflection. (b) $\pi$-pulsed excitation of qubit D shifts the resonator by $2\chi$ (blue) compared to when it is in its ground state (yellow). Measurement in reflection. (c) Number splitting of coaxmon D, in transmission.

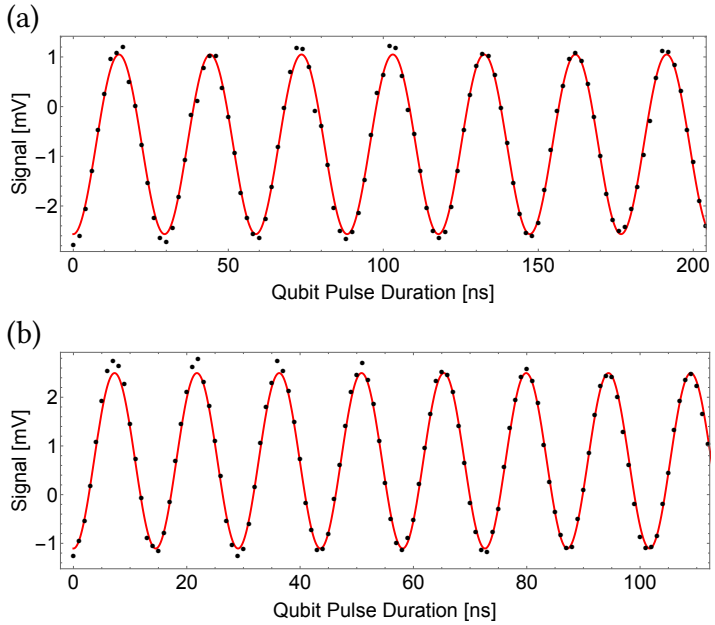


Figure 6.8: Rabi oscillations for coaxmon C and D. (a) Driving coaxmon C at $-5\,\mathrm{dBm}$ results in a Rabi frequency of $33.96\,\mathrm{MHz}$. (b) Driving coaxmon D at $0\,\mathrm{dBm}$ results in a Rabi frequency of $68.84\,\mathrm{MHz}$. The points represent the data while the red line is a damped sinusoidal fit.

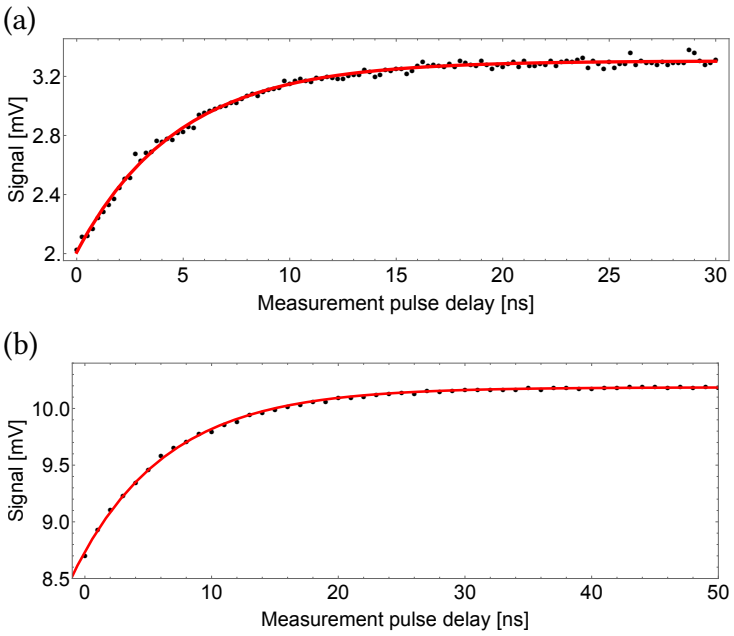


Figure 6.9: Qubit lifetime of coaxmon C and D. Dots represent the experimental data, the red line is an exponential fit. (a) coaxmon C exhibits a lifetime of $T_1^C = 4.7\,\mu\mathrm{s}$. (b) coaxmon D shows a qubit lifetime of $T_1^D = 7.3\,\mu\mathrm{s}$.

## 6.4 Qubit-Qubit Coupling Strength

Having characterised each single coaxmon on its own, the interaction is to be investigated. The coupling strength of the qubits is characterised through a Rabi measurement for different detunings and is shown in Section 6.4.1. A comparison to simulation follows in Section 6.4.2.

### 6.4.1 Measurements

To measure the strength of the qubit-qubit coupling, the frequency of qubit C is measured in two cases: qubit D is in its ground or excited state. This is achieved by measuring Rabi oscillations of qubit C as a function of the detuning $\Delta_C$ as it is shown in Figure 6.10. Since the effective Rabi frequency is $\Omega'_C = \sqrt{\Omega_C^2 + \Delta_C^2}$ with the Rabi frequency $\Omega_C$, the qubit's frequency is the value with the slowest Rabi oscillations. This frequency is marked in Figure 6.10 by a white dotted line. Figure 6.10 (a) shows Rabi oscillations on qubit C is in its ground state. Figure 6.10 (b) shows the case for D in its first excited state. It is clear, that the qubit frequency shifts by $\Delta f = 9.5\,\mathrm{MHz}$ when D is excited.

In order to calculate the qubit-qubit coupling strength from the shift $\Delta f$, the complete two-qubit Hamiltonian is needed:

$$\hat{H} = \hat{H}_C + \hat{H}_D + \hat{H}_{int}. \tag{6.1}$$

$\hat{H}$ consists of each single qubit-resonator Hamiltonian for coaxmon C and D plus the interaction term $\hat{H}_{int}$, that includes the qubit-qubit interaction as well as potential resonator-resonator and cross qubit-resonator interactions. Here, only the qubit-qubit interaction is considered, which is

$$\hat{H}_{int} = J\hbar(\hat{\sigma}_C^+\hat{\sigma}_D^- + \hat{\sigma}_C^-\hat{\sigma}_D^+) \tag{6.2}$$

with the qubit-qubit interaction strength J. Analogously to Equation 3.8, diagonalizing and applying rotating wave approximation allows one to rewrite this Hamiltonian

$$\hat{H}' = \frac{\omega'_C}{2}\hat{\sigma}_C^z\mathbb{I} + \frac{\omega'_D}{2}\mathbb{I}\hat{\sigma}_D^z + \frac{J^2}{\Delta_{CD}}\hat{\sigma}_C^z\hat{\sigma}_D^z \tag{6.3}$$

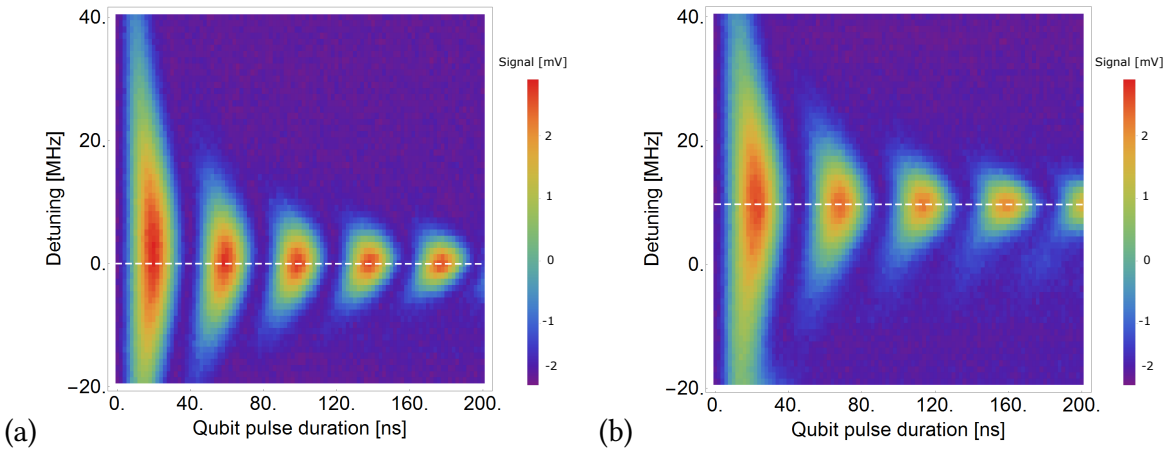


Figure 6.10: Rabi measurements on coaxmon C for different detunings $\Delta_C$ to qubit C with a) qubit D in its ground state b) qubits D excited. The qubit's frequency shifts by $9.5\,\mathrm{MHz}$.

with the two renormalized qubit frequencies $\omega_i'$, their coupling J and the qubit-qubit detuning $\Delta_{CD}$. Here, the first operator in each term acts on the first qubit and the second on qubit two respectively. Analogue to the $\chi$-shift measurement of the resonator, the frequency of qubit one shifts by $2J^2/\Delta_{CD}$ when the the second qubit is excited in contrast to when it is in its ground state. This refers to the measurement presented in Figure 6.10 where a shift of $\Delta f = 9.5\,\mathrm{MHz}$ in the Rabi frequency. Given that $\Delta_{CD} = 244\,\mathrm{MHz}$ the corresponding qubit-qubit coupling strength results in $J = \sqrt{(\Delta_{CD}\Delta f)/2} = 34\,\mathrm{MHz}$.

Another aspect that should be mentioned in this context is the drastic damping in the measurement signal for increasing detunings. This is unusual and so far this is the only device exhibiting this behaviour. No explanation has been found yet.

### 6.4.2 Comparison to Simulation

Comparing the experimental value for the qubit-qubit coupling of $J = 34\,\mathrm{MHz}$ to the aimed value of $18\,\mathrm{MHz}$ shows, that in the experiment the coupling is about twice as strong. The discrepancy could result from an inaccuracy of the capacitance values used in the lumped element model to calculate J. Since the capacitances are simulated to an accuracy of 1% and since the resonator-qubit coupling strength in the network analysis in Section 4.8 gives a result of only 5.5% off the experimental value, the estimation of

capacitance values are assumed to not be the source of this error. Another error source could be the Lumped Element Model (LEM) itself. The model calculates all values solely based on static field simulations. In this model, any inductive couplings that increase the real value for J are neglected. However, when comparing the lumped element model for the single coaxmon in Section 4.9, the resonator-qubit coupling is indeed smaller than the experimental one but only by 10% and not 50% as it is the case for J here. Nevertheless, it is possible that the qubit-qubit inductive coupling is underestimated and are comparable to the capacitive coupling. However, this is still an assumption. At the moment a second set of coupled coaxmons on a new chip is currently being measured. Here, the same geometry of capacitances results in a J of $11\,\mathrm{MHz}$. The question is what the difference between this new device and the first device with coaxmon C and D is. Apart from slightly different frequencies and a different detuning, the qubit transitions in the new device are further apart. Due to this, the hypothesis is that the experimental measured J for coaxmon C and D is increased because that transitions are close. When driving Rabi on coaxmon C while D is excited, indeed D can decay and excite $f_{12}^{C}$ and thus couple both coaxmons. The same is true the other way around. When coaxmon C is excited, and Rabi oscillations are driven on coaxmon D at high enough power, coaxmon C might be driven simultaneously into its second excited state. This additional coupling could explain the discrepancy in J between simulation and experiment. In future experiments, where all qubit frequencies are well separated, this deviation should not be a problem anymore.

## 6.5 Selectivity

The selectivity $S$ of a multi-qubit device refers to how well one qubit can be driven through its own port without driving the surrounding qubits as well. The ratio of the voltage drop across the neighbouring qubit divided by the drop across the intentionally driven qubit is the selectivity. Hence, the lower S the better a qubit can be driven without interfering with the others. In this Section, the selectivities of the coupled as well as the uncoupled qubits on the sapphire chip as depicted in Figure 6.2 are measured and compared to simulation results.

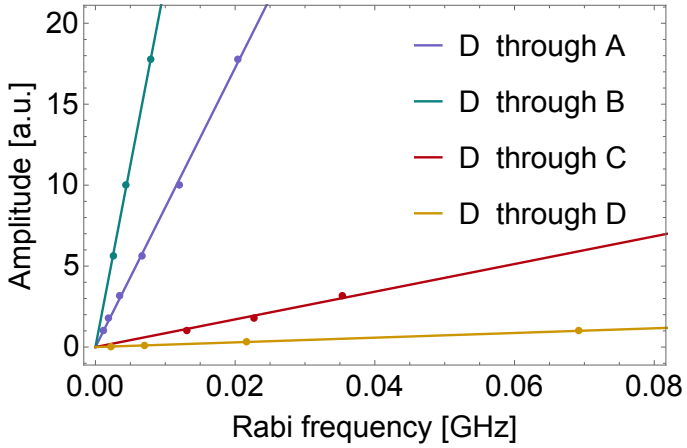


Figure 6.11: Rabi oscillation amplitude as a function of Rabi frequency on qubit D through the different qubit ports A, B, C and D.

### 6.5.1 The Experiment

To determine the selectivity for the four qubit device as shown in Figure 6.2, Rabi oscillations on each qubit were driven through all qubit ports at different drive strengths. For example, qubit D was driven through its own qubit port with a driving strength ranging from $-40\,\mathrm{dBm}$ to $0\,\mathrm{dBm}$ in steps of $10\,\mathrm{dBm}$. Since the Rabi frequency is $\Omega = \vec{E} \cdot \vec{d}/\hbar$, where $\vec{E}$ is the applied electric field and $\vec{d}$ the qubit dipole moment, $\Omega$ is proportional to the amplitude of the driving field. The Rabi frequency is measured for driving qubit D through all four ports as a function of amplitude and the result is plotted in Figure 6.11. The data is fitted to the model $A = k \cdot f_{Rabi}$ and results in a Table for $k_{ij}$:

| $k_{ij}$ | A | B | C | D |
|---|---|---|---|---|
| A | 12.9 | 1030 | 1810 | 1260 |
| B | 99.0 | 11.3 | 931 | 2510 |
| C | 1780 | 905 | 14.4 | 422 |
| D | 862 | 2250 | 85.5 | 14.5 |

(6.4)

where $i$ is the driven qubit and $j$ is the driving qubit port with $i, j =$ A,B,C,D. Ratios of these determined $k$-values refer to the ratio of amplitudes to drive the same Rabi oscillations on the driven qubit. This is exactly, what selectivity means. Defining the drive

of one qubit through its own port as $100\%$ selectivity, the ratio of $k$-values $S_{ij} = k_{ii}/k_{ij}$ then refers to the percentage of amplitude that is needed to achieve the same Rabi oscillations frequency.

| $S_{ij}$ | A | B | C | D |
|---|---|---|---|---|
| A | 100 | 1.3 | 0.72 | 1.00 |
| B | 11 | 100 | 1.2 | 0.45 |
| C | 0.81 | 1.6 | 100 | 3.4 |
| D | 1.70 | 0.64 | 17 | 100 |

(6.5)

Partially, the selectivity might depend on the fact that the ports couple with different strengths to their own port. Their distance to the qubits is critical and their distances might not be set very accurate. Therefore, the coupling $C_{ij}$ of each port to any qubit can be calculated as $C_{ij} = k_{jj}/k_{ii}$ where the coupling to the own port is normalized to 1. This can then be taken into account into the selectivity calculation.

| $C_{ij}$ | A | B | C | D |
|---|---|---|---|---|
| A | 1.00 | 0.88 | 1.11 | 1.12 |
| B | 1.14 | 1.00 | 1.27 | 1.28 |
| C | 0.90 | 0.79 | 1.00 | 1.01 |
| D | 0.89 | 0.78 | 0.99 | 1.00 |

(6.6)

Now, the port coupling can be taken into account when calculating the scaled selectivity with $S_{ij}^{\text{scaled}} = C_{ij} \cdot S_{ij}$

| $S_{ij}^{\text{scaled}}$ | A | B | C | D |
|---|---|---|---|---|
| A | 100 | 1.10 | 0.79 | 1.20 |
| B | 13 | 100 | 1.50 | 0.58 |
| C | 0.73 | 1.3 | 100 | 3.4 |
| D | 1.5 | 0.5 | 17 | 100 |

(6.7)

From this, it can for example be concluded that the uncoupled pair AC(CA) exhibits a selectivity of 0.79% (0.73%) and the pair BD(DB) 0.5%(0.58%). Strangely, the diagonal pairs,

which are separated further apart, show a slightly higher selectivity of 1.2-1.5%. The coupled pairs AB(BA) and CD(DC) show a asymmetric selectivity behaviour of 1.10%(13%) and CD(DC) even 3.4%(17%). These results are discussed in comparison to experiment in the following Section.

### 6.5.2 Comparison to Simulation

The simulation predictions to compare to the selectivity Table 6.7 are listed in Table 5.8. In all cases, the measured selectivity is greater than in simulation. Whereas all uncoupled pairs show a relative symmetric behaviour, the coupled pairs cleary do not. For example, the pair CD in one way exhibits a selectivity of 17% and in the other only 3.4%. This strongly leads to the conclusion, that the selectivity measurement is affected by the Cross-Resonance drive. Indeed, when measuring the Rabi oscillations on one qubit driven through another qubit's port, this exactly equals driving of the Cross-Resonance gate. Therefore, the second qubit's frequency has to be applied to the first qubit. Hence, when performing the selectivity measurements, the CR gate is driven and this obviously increases the measured selectivity. To get the corrected value for the selectivity which is only caused by the (non) selective qubit ports, the CR drive would have to be subtracted from these measured values. This could be done, once the CR gate is driven and characterised. Until then, the measured values for selectivity only give an upper bound and do not mean that simulation values are underestimated.

## 6.6 Conclusion on the Experiments

At this point, a conclusion on the experiments performed on the coaxmons CD can be made. The characterisation of the coupled coaxmon shows similar behaviour to the first single coaxmon device as published in (Rahamim et al. [2017]) and appended to this thesis. This shows that the fabrication of the coaxmon design is stable and well repeatable. The first coupled measurements on intentionally coupled coaxmons are performed and discussed. Unfortunately, it is impossible to realise the CR gate on the presented device,

as the qubit transitions $f_{12}^C$ and $f_{01}^D$ are too close in frequency. A second set of coupled coaxmons on a new chip is already fabricated, promises to exhibit the aimed value for qubit-qubit detuning of $500\,\mathrm{MHz}$ and is currently being measured. As measurements of this new device exceed the period of this Master's thesis, the realisation of the CR gate on a coupled coaxmon device cannot be demonstrated here. However, everything indicates that a successful experiment can be performed if fabrication successfully realises the design with the aimed parameters.

# 7 Conclusion and Outlook

This thesis presents simulation and measurement of both single and coupled coaxial superconducting qubits. The work has been carried out on the new coaxmon architecture, which is simple to fabricate, exploits only capacitive coupling and implements qubit control and readout entirely out of the plane of the qubit.

At first, the single coaxmon design is optimised and the corresponding single coaxmon is fabricated, measured and the results are published in (Rahamim et al. [2017]) (see appendix). Good agreement between HFSS simulations and experiments is achieved and demonstrates the power of the black-box quantisation method. Using this theory, predictions about device parameters before fabrication are possible, allowing for devices with target parameters to be fabricated with confidence. However, it must be said that simulations are very time consuming. Many mesh refinements are necessary to simulate the resonator frequency and even when using the external cluster, the smallest possible mesh is not enough to obtain the correct resonator frequency. Once the knowledge is gained on how to use the mesh refinements and on how to calibrate the simulation to correct for this error, this method offers reliable predictions for optimising the device properties. The second presented method, the lumped element model, allows one to overcome the problem of long simulations since Ansys Maxwell solves static fields relatively fast. Comparison with experiment is found to be good, but not as accurate as for the HFSS method. This is due to the solely static simulation and neglection of any high frequency related interactions.

Following the single coaxmon characterisation, the thesis then focuses on the coupling of two coaxmons. For this reason, a review on two-qubit gates is performed and the Cross-Resonance (CR) gate is chosen as a suitable candidate. In order to gain knowledge on how to realise the CR gate experimentally, simulations of this gate are performed.

This enables choosing a set of desired qubit and resonator parameters. Exploiting the lumped element model allows adjusting the additional qubit-qubit capacitance needed to achieve the desired qubit-qubit coupling. Estimation of the selectivity below 2% for the coupled coaxmon device confirms the suitability of such a design for individual control of qubits.

In addition, the very first coupled coaxmon is realised and measured. Measurements show that this first device exhibits a problematic qubit energy level spacing to realise the Cross-Resonance gate as both qubits have a transition similar to the same frequency. Moreover, only an upper bound for the selectivity can be measured. A second coupled coaxmon has subsequently been fabricated and still needs to be measured completely. If fabrication has achieved the aimed qubit and resonator parameters on this device, the Cross-Resonance gate should be demonstrated soon. Once realised, the gate can also be optimised by applying cancellation pulses. The recent publications on the CR gate, namely (Sheldon et al. [2016]) and (Kirchhoff et al. [2017]), present several optimisation procedures that can be tested in the future.

After a two-qubit gate is implemented in the coaxmon architecture, the next step is to realise gates on more than two-qubit devices. In order to achieve this, several challenges have to be faced. First of all, qubit lifetimes have to be increased with improvement in fabrication and progress in material research. Secondly, a better control in fabrication is needed to attain the desired qubit and resonator parameters. Lastly, when it comes to large number of coupled coaxmons, the accidental degeneracy of qubit and resonator frequencies becomes likely. As a long-term goal, the implementation of a tunable coupling, for example using a tunable bus resonator as done in (McKay et al. [2016]), might come of importance. Since the field of superconducting qubits is rapidly progressing, one may expect that the stated difficulties to realise multi-coaxmon devices are overcome within the next couple of years. In this context, this thesis provides two powerful tools that not only can be exploited to design and optimise single- and two-qubit devices, but can also be extended to design multi-qubit devices in the future.

# Acknowledgements

I hereby would like to thank all of those who supported me during my Master's thesis. First of all, many thanks to Dr. Peter Leek who let me write this thesis in his group. His passion about superconducting qubits has always fascinated and motivated me to study the field as much as I could this last year.
At least as many thanks go to Prof. Fred Jendrzejewski supporting my thesis from my home university and who first of all introduced me to the field of superconducting qubits. Thank you for allowing me to write my thesis at another university enriching my studies even further with lots of experiences in another country.
Of course, I also want to say thank you to the whole LeekLab group to welcome me so warmly. Thank you for teaching me so much by working with you on this project. I always appreciated the atmosphere and to be able to come to anyone with any question at any time. Thank you Joseph, for the fabrication of all devices and publishing our both very first paper together. Andy, thank you for enabling any measurements with your work on the optimal control setup as well as for having answers to absolutely any question. Thank you Giovanna, especially for proof reading my thesis. Thank you Riccardo, Michael, Peter, Takahiro, Patrik, Martina, Matthias and Arjan for being such a great (extended) group, having tired but fun late night fridge-closing sessions as well as having many rowing and running discussions motivating each other every day.
A very big thank you also goes to my parents and my sister. They supported not only my Master thesis but my whole studies from the very first day. Thank you for correcting my drafts and motivating me at any time.

# Appendix:
# Publication

# Double-sided coaxial circuit QED with out-of-plane wiring

J. Rahamim, T. Behrle, M. J. Peterer, A. Patterson, P. A. Spring, T. Tsunoda, R. Manenti, G. Tancredi, and P. J. Leek
*Clarendon Laboratory, Department of Physics, University of Oxford, Parks Road, Oxford OX1 3PU, United Kingdom*

(Received 23 March 2017; accepted 16 May 2017; published online 30 May 2017)

Superconducting circuits are well established as a strong candidate platform for the development of quantum computing. In order to advance to a practically useful level, architectures are needed which combine arrays of many qubits with selective qubit control and readout, without compromising on coherence. Here, we present a coaxial circuit quantum electrodynamics architecture in which qubit and resonator are fabricated on opposing sides of a single chip, and control and readout wiring are provided by coaxial wiring running perpendicular to the chip plane. We present characterization measurements of a fabricated device in good agreement with simulated parameters and demonstrating energy relaxation and dephasing times of $T_1 = 4.1\ \mu s$ and $T_2 = 5.7\ \mu s$, respectively. The architecture allows for scaling to large arrays of selectively controlled and measured qubits with the advantage of all wiring being out of the plane. *Published by AIP Publishing.* [http://dx.doi.org/10.1063/1.4984299]

The realization of technological devices that harness quantum superposition and entanglement to perform computational tasks that are difficult with classical computers is a major research goal that may revolutionize computing.[1] Superconducting circuits have advanced to become a strong candidate platform for building such quantum computers,[2] with recent demonstrations of circuit operation at the threshold for fault tolerance,[3] quantum error detection[4,5] and correction,[6] and rudimentary quantum simulations.[7–9] While the scale required for full fault tolerant universal quantum computation is still far away,[10] current devices are not far from the complexity required for a demonstration of computation that is beyond the reach of the best classical supercomputers.[11] To reach beyond this scale (of order 50 qubits) in a single monolithic quantum circuit, it is desirable to develop circuit architectures that implement good connectivity among arrays of many qubits, along with selective control and readout wiring, without compromising on qubit coherence. This is difficult to achieve if the circuit is constrained to a single 2D plane, since the number of control and readout connections scales linearly with the number of qubits $N$, while the edges of a 2D array scale as $\sqrt{N}$. This problem can only be overcome by incorporating 3D connectivity.

The challenge of incorporating control wiring out of the plane of a superconducting quantum circuit has been approached so far from several directions. A recent proposal suggests the use of through-chip microwave silicon vias, as part of a monolithic architecture to implement the surface code.[12] Bump bonding between multiple circuit layers,[13] and spring-loaded microwave contacts[14] are also under development. Pursuing a modular (as opposed to monolithic) quantum computing architecture is an alternative route, and some promising steps have been made in this direction with superconducting circuits, through integration with high quality 3D microwave resonators.[15–17]

In this letter, we present a single unit cell of an architecture for quantum computing with superconducting circuits that is simple to fabricate, requires no bonds, exploits only capacitive couplings, and implements qubit control and readout entirely out of the plane of the qubit, without relying on complex through-chip fabrication.[18]

By virtue of the out-of-plane readout and wiring elements, the device may be physically scaled to large 2D qubit arrays without any alteration to the wiring design. Additionally, the double-sided structure and absence of wiring elements in the circuit design avoids crowding on the chip, hence reducing sources of crosstalk.

The device is depicted in Fig. 1. It consists of a superconducting charge qubit in the transmon regime[19] with

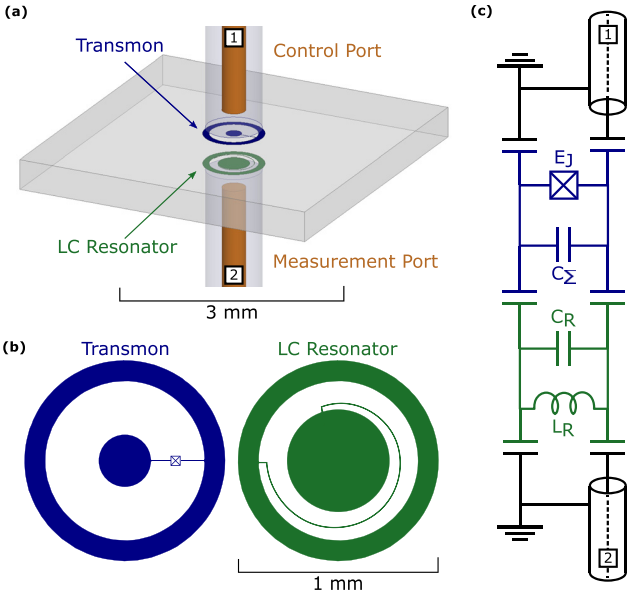


FIG. 1. (a) CAD design of the unit cell, with transmon qubit and lumped element resonator on opposing sides of a substrate, and control and measurement ports perpendicular to the chip plane. (b) Designs of the transmon and resonator. In the transmon, the two electrodes are connected by a single Josephson junction, whereas the electrodes of the resonator are connected by an inductor line. (c) Equivalent circuit of the device, showing the resonator inductance and capacitance, $L_R$ and $C_R$, the junction Josephson energy $E_J$, and effective capacitance over the junction $C_\Sigma$.

coaxial electrodes, which we call the coaxmon (similar to the concentric[20] and aperture[16] transmons) coupled to a lumped element LC microwave resonator fabricated on the opposite side of the chip, realising dispersive circuit quantum electrodynamics[21] (QED). The device is controlled and measured via coaxial ports, perpendicular to the plane of the chip [see Fig. 1(a)], whose distance from the chip can be modified to change the external quality factor of the circuits. These ports can be used for independent control of the qubit and measurement of the resonator in reflection, or to measure the device in transmission.

The device is fabricated through two stages of electron beam lithography, patterning either side of a 0.5 mm thick sapphire chip with an aluminum LC resonator and coaxmon. During fabrication, the bottom of the chip is protected with a spin-coated layer of polymer resist, and chip holders are used to ensure the bottom of the device is suspended throughout. The process could be further improved in the future by producing the LC resonators with photolithography, thus enabling batch production of devices that only require one electron-beam step. The device is then mounted in an aluminum sample holder and thermally anchored to the 10 mK base plate of a dilution refrigerator. The control and measurement ports consist of copper-beryllium wire passing through a cylindrical hole in the sample holder, soldered to the center conductor of a microwave connector in order to connect to external microwave wiring. In this experiment, the distance from the qubit(resonator) to the control(measurement) port is 0.6(0.4) mm. The device is embedded in a standard circuit QED measurement setup, in which input signals are heavily cryogenically attenuated (by approximately 70 dB) to reduce thermal noise, and measurements are made via cryogenic circulators and a low noise HEMT amplifier, the signal finally being recorded as a voltage $V_{ADC}$ with an analog-to-digital converter (ADC).

We first measure the device transmission spectrum $S_{21}$ at a low drive power of $P_r = -50$ dBm, finding the Lorentzian response of the LC resonator[22] at $f_{r0} = 10.23$ GHz, with quality factor $Q = 2080$ [see Fig. 2(a)]. Far from resonance, $S_{21}$ remains 30 dB below the LC resonance over the 8–12 GHz measurement bandwidth. We next fix the measurement drive at the LC resonance, and add an additional drive at frequency $f_{dq}$ to port 1, to carry out spectroscopy of the qubit using the dispersive qubit state-dependent frequency shift of the LC resonator.[23] The spectroscopy is carried out with an 8 $\mu$s drive pulse immediately followed by an 8 $\mu$s measurement pulse at frequency $f_{r0}$ and power $P_r = -35$ dBm, averaging the data $10^6$ times. In Fig. 2(b), we show such spectroscopy at two different drive powers. At low drive power $P_L = -45$ dBm, we observe only the qubit transition at $f_{01} = 7.23$ GHz, whereas at higher power $P_H = -5$ dBm, we observe two additional spectral lines below $f_{01}$, as expected of a transmon qubit. We observe a two-photon transition at $f_{02}/2 = 7.08$ GHz and a three-photon transition at $f_{03}/3 = 6.93$ GHz to higher energy levels of the transmon, as illustrated in the inset of Fig. 2(b). Note that the broadening of the $f_{01}$ peak at the higher drive power originates from strong Rabi driving of the transition. From these parameters, we calculate a detuning between qubit and resonator of $\Delta_0/(2\pi) = -3.00$ GHz, Josephson energy $E_J/h = 24.1$ GHz, charging energy $E_C/h = 294$ MHz, and $E_J/E_C = 81.8$.

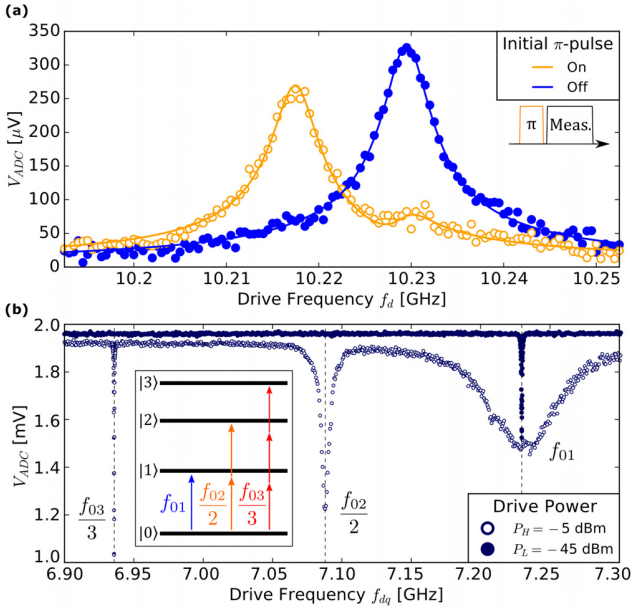


FIG. 2. (a) Resonator spectroscopy in the low photon number limit $\bar{n} \ll 1$. Transmitted signal amplitude at the ADC measured with a 1 $\mu$s pulse at $f_d$, with (orange) and without (blue) a $\pi$-pulse applied to the qubit immediately prior to the measurement pulse (pulse scheme inset). The data (circles) are fitted (solid lines) as described in the main text. (b) Pulsed qubit spectroscopy for two different qubit drive powers. At –45 dBm only the $f_{01} = 7.23$ GHz transition is visible. At a drive of –5 dBm, two multi-photon transition frequencies $f_{02}/2$ and $f_{03}/3$ become visible and the $f_{01}$ is broadened. Inset: the energy level diagram of a transmon qubit illustrating the multi-photon transitions.

We next characterize the interaction between qubit and resonator by measuring the qubit-state-dependent resonator frequency shift $\chi$. In order to do this, we repeat the transmission measurement of the LC resonance after preparing the qubit in its first excited state prior to a measurement pulse [see Fig. 2(a), orange curve]. The resonance is seen to shift from $f_{r0}$ to $f_{r1} = 10.217$ GHz. In addition to the shifted peak at $f_{r1}$, a residual peak at $f_{r0}$ is also visible due to the excited state population partly decaying during the measurement pulse. The response is fitted to the weighted sum of two Lorentzians in the complex plane, from which we extract the dispersive shift of the resonator $2\chi/(2\pi) = f_{r0} - f_{r1} = -12.68$ MHz. We then use this to derive the qubit-resonator coupling $g/(2\pi) = 462$ MHz from the relation

$$\chi \approx -\frac{g^2(E_C/\hbar)}{\Delta_0(\Delta_0 - (E_C/\hbar))}, \tag{1}$$

valid for a transmon in the dispersive regime.[19] Since our implementation of cQED consists entirely of lumped elements, we can calculate the expected parameters using a finite element electrostatic simulation (Ansys Maxwell) of the circuit. The circuit representation can be quantized to give expressions for the qubit and resonator frequencies, $f_{01}$ and $f_{r0}$, and the coupling $g$ between them, as a function of the capacitance network, as well as the resonator inductance $L_R$ and Josephson energy $E_J$ which we match to the experimentally measured values. Such a simulation predicts a coupling $g/2\pi \approx 420$ MHz. The discrepancy between the estimated and measured value may be due to the use of a static solver, which neglects any inductive coupling in the circuit. We have

also used this model to simulate the coupling between control (measurement) port and qubit (resonator), and its dependence on the displacement of the port axis from the qubit and resonator centers. We find that for the circuit geometry presented here, the coupling falls to ∼5% at a displacement of 1 mm, indicating that good selectivity should be achievable between control and measurement signals in adjacent cells in a grid of multiple qubits.

We now move on to time resolved qubit measurements which are performed by measuring the resonator in reflection on port 2 and applying qubit drive pulses to port 1. In Fig. 3(a) we first show Rabi oscillations of the qubit state, measured by first applying a short microwave pulse of length $\tau$ to the qubit in its ground state at frequency $f_{01}$, followed by a resonator readout pulse of length 16 $\mu$s and frequency $f_{r0}$ at a low photon number. The population $P_1$ of the qubit excited state $|1\rangle$ is recovered from the weighted integral of the resonator response by comparing it to the integral of simulated Cavity-Bloch traces[24] using parameters independently determined by the other characterization experiments, and including a correction to take into account interference with the directly reflected measurement pulse.

We determine the qubit relaxation time $T_1 = 4.10$ $\mu$s and phase coherence time $T_2 = 5.65$ $\mu$s using standard techniques [see Figs. 3(b) and 3(c)]. A spin echo pulse sequence reveals an extended $T_{2E} = 6.67$ $\mu$s. To further evaluate the performance of the device, we perform Clifford-based randomized benchmarking and find the average fidelities of primitive gates to be 99.5% using half-DRAG pulses.[25] We also determine an upper bound for the qubit temperature by measuring the amplitude of Rabi oscillations on the $f_{12}$ transition both

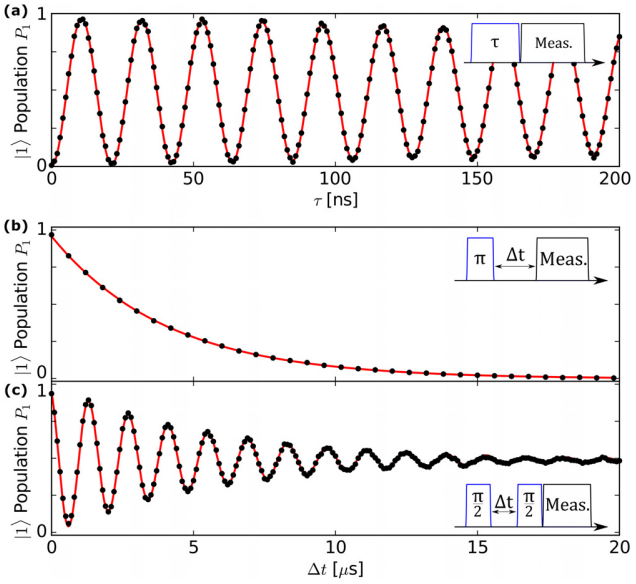


FIG. 3. Time-resolved qubit measurements with data points in black and fits as solid red lines. The pulse schemes of the measurements are shown in the insets. (a) Rabi oscillations of 47 MHz performed on the device at a qubit drive power of –20 dBm. An exponentially decaying oscillation $P_1 = A\cos(\omega t)e^{-t/T_{\text{Rabi}}}$ is fitted to the data. (b) Qubit energy relaxation fitted to an exponential decay $P_1 = Ae^{-t/T_1}$ reveals a $T_1 = 4.10$ $\mu$s. (c) Ramsey oscillations performed with the qubit drive detuned 4.5 MHz from $f_{01}$ reveals a $T_2 = 5.65$ $\mu$s from the fitted oscillating decay $P_1 = A\cos(\omega t + \phi)e^{-t/T_2}$. In all cases, $P_1$ is extracted from the pulsed resonator response by fitting to Cavity-Bloch equations.

TABLE I. Device parameters.

| Parameter | Value |
|---|---|
| Resonator frequency $f_{r0}$ (GHz) | 10.23 |
| Resonator quality factor | 2080 |
| Qubit $f_{01}$ (GHz) | 7.23 |
| Dispersive shift $\chi/2\pi$ (MHz) | −6.34 |
| $E_C/h$ (MHz) | 294 |
| $E_J/E_C$ | 81.8 |
| Coupling $g/2\pi$ (MHz) | 462 |
| $T_1$ ($\mu$s) | 4.10 |
| $T_2$ ($\mu$s) | 5.65 |
| $T_2$ Echo ($\mu$s) | 6.67 |

with and without an initial $\pi$-pulse on the $f_{01}$ transition.[26] We find the qubit temperature to be $T_q \leq 70$ mK corresponding to an initial ground state population of $P_0 \geq 99.3\%$. Hence, our single-qubit unit cell displays promising performance for an initial demonstration.

We have presented a double-sided coaxial implementation of circuit QED. We summarize the device parameters in Table I. We anticipate this architecture to be easily extendable to arrays of nearest-neighbor coupled qubits by virtue of the out-of-plane readout and control wiring, and so will be a good candidate architecture for the next generation of multi-qubit devices for quantum simulation and computation.

This work has received funding from the UK Engineering and Physical Sciences Research Council under Grant Nos. EP/J001821/1, EP/J013501/1 and EP/M013243/1. A.P. and T.T. acknowledge Oxford Instruments Nanoscience and the Nakajima Foundation, respectively, for financial support. Aspects of this work are currently covered by an international patent application.

[1]T. D. Ladd, F. Jelezko, R. Laflamme, Y. Nakamura, C. Monroe, and J. L. O'Brien, Nature **464**, 45–53 (2010).
[2]M. H. Devoret and R. J. Schoelkopf, Science **339**, 1169–1174 (2013).
[3]R. Barends, J. Kelly, A. Megrant, A. Veitia, D. Sank, E. Jeffrey, T. C. White, J. Mutus, A. G. Fowler, B. Campbell, Y. Chen, Z. Chen, B. Chiaro, A. Dunsworth, C. Neill, P. O'Malley, P. Roushan, A. Vainsencher, J. Wenner, A. N. Korotkov, A. N. Cleland, and J. M. Martinis, Nature **508**, 500–503 (2014).
[4]D. Ristè, S. Poletto, M. Z. Huang, A. Bruno, V. Vesterinen, O. P. Saira, and L. DiCarlo, Nat. Commun. **6**, 6983 (2015).
[5]J. Kelly, R. Barends, A. G. Fowler, A. Megrant, E. Jeffrey, T. C. White, D. Sank, J. Y. Mutus, B. Campbell, Y. Chen, Z. Chen, B. Chiaro, A. Dunsworth, I. C. Hoi, C. Neill, P. J. J. O'Malley, C. Quintana, P. Roushan, A. Vainsencher, J. Wenner, A. N. Cleland, and J. M. Martinis, Nature **519**, 66–69 (2015).
[6]N. Ofek, A. Petrenko, R. Heeres, P. Reinhold, Z. Leghtas, B. Vlastakis, Y. Liu, L. Frunzio, S. M. Girvin, L. Jiang, M. Mirrahimi, M. H. Devoret, and R. J. Schoelkopf, Nature **536**, 441–445 (2016).
[7]Y. Salathé, M. Mondal, M. Oppliger, J. Heinsoo, P. Kurpiers, A. Potočnik, A. Mezzacapo, U. Las Heras, L. Lamata, E. Solano, S. Filipp, and A. Wallraff, Phys. Rev. X **5**, 021027 (2015).
[8]R. Barends, L. Lamata, J. Kelly, L. García-Álvarez, A. G. Fowler, A. Megrant, E. Jeffrey, T. C. White, D. Sank, J. Y. Mutus, B. Campbell, Y. Chen, Z. Chen, B. Chiaro, A. Dunsworth, I. C. Hoi, C. Neill, P. J. J. O'Malley, C. Quintana, P. Roushan, A. Vainsencher, J. Wenner, E. Solano, and J. M. Martinis, Nat. Commun. **6**, 7654 (2015).
[9]P. J. J. O'Malley, R. Babbush, I. D. Kivlichan, J. Romero, J. R. McClean, R. Barends, J. Kelly, P. Roushan, A. Tranter, N. Ding, B. Campbell, Y. Chen, Z. Chen, B. Chiaro, A. Dunsworth, A. G. Fowler, E. Jeffrey, E. Lucero, A. Megrant, J. Y. Mutus, M. Neeley, C. Neill, C. Quintana, D. Sank, A.

Vainsencher, J. Wenner, T. C. White, P. V. Coveney, P. J. Love, H. Neven, A. Aspuru-Guzik, and J. M. Martinis, Phys. Rev. X **6**, 031007 (2016).
[10]A. G. Fowler, M. Mariantoni, J. M. Martinis, and A. N. Cleland, Phys. Rev. A **86**, 032324 (2012).
[11]S. Boixo, S. V. Isakov, V. N. Smelyanskiy, R. Babbush, N. Ding, Z. Jiang, J. M. Martinis, and H. Neven, e-print arXiv:1608.00263.
[12]R. Versluis, S. Poletto, N. Khammassi, N. Haider, D. J. Michalak, A. Bruno, K. Bertels, and L. DiCarlo, e-print arXiv:1612.08208.
[13]J. Mutus, B. Foxen, E. Lucero, J. Kelly, Y. Yang, A. Yu, M. Baldwinson, Z. Chen, B. Chiaro, A. Dunsworth, C. Neill, C. Quintana, J. Wenner, and J. M. Martinis, in H46.00006: APS March Meeting (2017).
[14]J. H. Béjanin, T. G. McConkey, J. R. Rinehart, C. T. Earnest, C. R. H. McRae, D. Shiri, J. D. Bateman, Y. Rohanizadegan, B. Penava, P. Breul, S. Royak, M. Zapatka, A. G. Fowler, and M. Mariantoni, Phys. Rev. Appl. **6**, 044010 (2016).
[15]C. Axline, M. Reagor, R. Heeres, P. Reinhold, C. Wang, K. Shain, W. Pfaff, Y. Chu, L. Frunzio, and R. J. Schoelkopf, Appl. Phys. Lett. **109**, 042601 (2016).
[16]T. Brecht, Y. Chu, C. Axline, W. Pfaff, J. Z. Blumoff, K. Chou, L. Krayzman, L. Frunzio, and R. J. Schoelkopf, Phys. Rev. Applied **7**, 044018 (2017).
[17]A. Narla, S. Shankar, M. Hatridge, Z. Leghtas, K. M. Sliwa, E. Zalys-Geller, S. O. Mundhada, W. Pfaff, L. Frunzio, R. J. Schoelkopf, and M. H. Devoret, Phys. Rev. X **6**, 031036 (2016).
[18]S. K. Tolpygo, Low Temp. Phys. **42**, 361–379 (2016).
[19]J. Koch, T. M. Yu, J. Gambetta, A. A. Houck, D. I. Schuster, J. Majer, A. Blais, M. H. Devoret, S. M. Girvin, and R. J. Schoelkopf, Phys. Rev. A **76**, 042319 (2007).
[20]J. Braumüller, M. Sandberg, M. R. Vissers, A. Schneider, S. Schlör, L. Grünhaupt, H. Rotzinger, M. Marthaler, A. Lukashenko, A. Dieter, A. V. Ustinov, M. Weides, and D. P. Pappas, Appl. Phys. Lett. **108**, 032601 (2016).
[21]A. Wallraff, D. I. Schuster, A. Blais, L. Frunzio, R.-S. Huang, J. Majer, S. Kumar, S. M. Girvin, and R. J. Schoelkopf, Nature **431**, 162–167 (2004).
[22]In order to rule out the possibility that this resonance is a mode of the sample holder, we have performed high frequency simulations of the device predicting the LC resonance at 10.5 GHz and the lowest frequency mode of the sample holder at 20.5 GHz.
[23]A. Wallraff, D. I. Schuster, A. Blais, L. Frunzio, J. Majer, M. H. Devoret, S. M. Girvin, and R. J. Schoelkopf, Phys. Rev. Lett. **95**, 060501 (2005).
[24]R. Bianchetti, S. Filipp, M. Baur, J. M. Fink, M. Göppl, P. J. Leek, L. Steffen, A. Blais, and A. Wallraff, Phys. Rev. A **80**, 043840 (2009).
[25]E. Lucero, J. Kelly, R. C. Bialczak, M. Lenander, M. Mariantoni, M. Neeley, A. D. O'Connell, D. Sank, H. Wang, M. Weides, J. Wenner, T. Yamamoto, A. N. Cleland, and J. M. Martinis, Phys. Rev. A **82**, 042339 (2010).
[26]K. Geerlings, Z. Leghtas, I. M. Pop, S. Shankar, L. Frunzio, R. J. Schoelkopf, M. Mirrahimi, and M. H. Devoret, Phys. Rev. Lett. **110**, 120501 (2013).

# Lists

## List of Figures


2.1 Advantages of the transmon regime and the coaxial geometry combined in the scalable coaxmon architecture. . . . . 6
2.2 State of the art transmon architectures. . . . . 9

3.1 Josephson junction. . . . . 13
3.2 The Cooper-Pair box electric circuit and energy level diagram. . . . . 15
3.3 The transmon regime. Eigenenergies versus the effective offset charge for different ratios of $E_C/E_J$ . . . . . 16
3.4 The black-box quantisation model. . . . . 20

4.1 Single coaxmon design. Illustration from the HFSS simulation. . . . . 26
4.2 The single coaxmon dimensions. . . . . 26
4.3 The simplified electric circuit representing the single coaxmon. . . . . 28
4.4 Single coaxmon with sample holder and a sketch of the mesh created by Ansys. . . . . 29
4.5 Resonator with and without mesh. . . . . 31
4.6 Transmission spectrum for different maximal mesh size restrictions on the resonator. The smaller the mesh, the more the transmission peak shifts towards smaller frequencies. It seems as if the peaks converges to a frequency below $10\,\mathrm{GHz}$. Due to the fact that a mesh restriction of $1\,\mu\mathrm{m}$ is the minimum, the simulated resonator frequency is bigger than in experiment for the same resonator length. . . . . 33
4.7 Transmission and reflection spectra of the single coaxmon. . . . . 34

4.8 Admittance spectra at the Josephson junction. . . . . 35
4.9 Resonator length variation. . . . . 39
4.10 Qubit lifetime $T_1$ as a function of qubit pin distance. . . . . 41
4.11 Simple circuit example for network analysis. . . . . 49
4.12 The coaxmon electric circuit for the network analysis. . . . . 50

5.1 The MAP gate working principle. . . . . 55
5.2 The Cross-Resonance gate working principle . . . . . 56
5.3 CR gate simulation results without any dissipation and perfect selectivity. 61
5.4 CR gate simulation including dissipation and imperfect selectivity. . . . . 63
5.5 Simulated CR gate fidelity for the four input states $|00\rangle$, $|01\rangle$, $|10\rangle$ and $|11\rangle$ as a function of gate time for infinite qubit lifetimes and perfect selectivity $S = 0$. . . . . 64
5.6 Simulated CR gate fidelity for the input states $|00\rangle$, $|01\rangle$, $|10\rangle$ and $|11\rangle$ as a function of gate time with imperfect selectivity and finite qubit lifetimes. 65
5.7 Design of the coupled coaxmon with aimed values. . . . . 67
5.8 The coupling capacitance and their effect on the qubit-qubit coupling strength J and the selectivity S. . . . . 68
5.9 (a) The qubit-qubit coupling strength $J$ as a function of the overlap b. (b) The selectivity S as a function of the overlap $b$. . . . . 69
5.10 The coupled coaxmon circuit for the selectivity estimation. . . . . 70

6.1 The experiment setup. . . . . 72
6.2 The coupled coaxmon chip and sample holder. . . . . 74
6.3 Resonator frequency sweep for coaxmon C and D. . . . . 75
6.4 Qubit spectroscopy of coaxmon C. . . . . 76
6.5 Qubit spectroscopy of coaxmon D. . . . . 77
6.6 Energy level diagram for the coupled coaxmons C and D. . . . . 78
6.7 $\chi$-shift measurements for coaxmon C and D. . . . . 80
6.8 Rabi oscillations for coaxmon C and D. . . . . 81
6.9 Qubit lifetime of coaxmon C and D. . . . . 81

6.10 Rabi measurements on coaxmon C for different detunings $\Delta_C$ to qubit C with a) qubit D in its ground state b) qubits D excited. . . . . 83
6.11 Rabi on D through different ports. . . . . 85

# List of Tables

4.1 Single coaxmon parameters. . . . . 37
4.2 Resonator width variations for two resonator spiral lengths. . . . . 38
4.3 Qubit pin distance $d_1$ variation and the effect on the qubit-resonator parameters. . . . . 40
4.4 Resonator pin distance variation and the effect on the qubit-resonator parameters. . . . . 41
4.5 Sample holder optimisation. . . . . 43
4.6 Statistical error on pin distance variations. . . . . 44
4.7 Systemtaic error derivation of the single coaxmon simulation. . . . . 45
4.8 Capacitance matrix for the single coaxmon. . . . . 48
4.9 Comparison of experiment to HFSS simulation and the lumped element model values. . . . . 52

6.1 Experimental parameters of the coupled coaxmon C and D. . . . . 79

# Bibliography

J. Antula. Temperature dependence of dielectric constant of al2o3. *Physics Letters A*, 25(4):308 –, 1967. ISSN 0375-9601. doi: http://dx.doi.org/10.1016/0375-9601(67)90666-4. URL http://www.sciencedirect.com/science/article/pii/0375960167906664.

C. Axline, M. Reagor, R. Heeres, P. Reinhold, C. Wang, K. Shain, W. Pfaff, Y. Chu, L. Frunzio, and R. J. Schoelkopf. An architecture for integrating planar and 3d cqed devices. *Applied Physics Letters*, 109(4):042601, 2016. doi: 10.1063/1.4959241. URL http://dx.doi.org/10.1063/1.4959241.

R. Bianchetti, S. Filipp, M. Baur, J. M. Fink, M. Göppl, P. J. Leek, L. Steffen, A. Blais, and A. Wallraff. Dynamics of dispersive single-qubit readout in circuit quantum electrodynamics. *Phys. Rev. A*, 80:043840, Oct 2009. doi: 10.1103/PhysRevA.80.043840. URL https://link.aps.org/doi/10.1103/PhysRevA.80.043840.

J. Z. Blumoff, K. Chou, C. Shen, M. Reagor, C. Axline, R. T. Brierley, M. P. Silveri, C. Wang, B. Vlastakis, S. E. Nigg, L. Frunzio, M. H. Devoret, L. Jiang, S. M. Girvin, and R. J. Schoelkopf. Implementing and characterizing precise multiqubit measurements. *Phys. Rev. X*, 6:031041, Sep 2016. doi: 10.1103/PhysRevX.6.031041. URL https://link.aps.org/doi/10.1103/PhysRevX.6.031041.

J. Braumüller, M. Sandberg, M. R. Vissers, A. Schneider, S. Schlör, L. Grünhaupt, H. Rotzinger, M. Marthaler, A. Lukashenko, A. Dieter, A. V. Ustinov, M. Weides, and D. P. Pappas. Concentric transmon qubit featuring fast tunability and an anisotropic magnetic dipole moment. *Applied Physics Letters*, 108(3):032601, 2016. doi: 10.1063/1.4940230. URL http://dx.doi.org/10.1063/1.4940230.

T. Brecht, Y. Chu, C. Axline, W. Pfaff, J. Z. Blumoff, K. Chou, L. Krayzman, L. Frunzio, and R. J. Schoelkopf. Micromachined integrated quantum circuit containing a superconducting qubit. *Phys. Rev. Applied*, 7:044018, Apr 2017. doi: 10.1103/PhysRevApplied.7.044018. URL https://link.aps.org/doi/10.1103/PhysRevApplied.7.044018.

Prof. Paola Cappellar. QUANTUM THEORY of RADIATION INTERACTIONS, 2012.

J. M. Chow, J. M. Gambetta, A. W. Cross, S. T. Merkel, C. Rigetti, and M. Steffen. Microwave-activated conditional-phase gate for superconducting qubits. *New Journal of Physics*, 15(11):115012, November 2013. doi: 10.1088/1367-2630/15/11/115012.

J.M. Chow, A. D. Córcoles, J. M. Gambetta, C. Rigetti, B. R. Johnson, John A. Smolin, J. R. Rozen, G.A. Keefe, M.B. Rothwell, M. B. Ketchen, and M. Steffen. Simple all-microwave entangling gate for fixed-frequency superconducting qubits. *Phys. Rev. Lett.*, 107:080502, Aug 2011. doi: 10.1103/PhysRevLett.107.080502. URL https://link.aps.org/doi/10.1103/PhysRevLett.107.080502.

D. Deutsch and R. Jozsa. Rapid Solution of Problems by Quantum Computation. *Proceedings of the Royal Society of London Series A*, 439:553–558, December 1992. doi: 10.1098/rspa.1992.0167.

R. P. Feynman. Simulating physics with computers. *International Journal of Theoretical Physics*, 21(6):467–488, 1982. ISSN 1572-9575. doi: 10.1007/BF02650179.

A. G. Fowler, M. Mariantoni, J. M. Martinis, and A. N. Cleland. Surface codes: Towards practical large-scale quantum computation. *Phys. Rev. A*, 86:032324, Sep 2012. doi: 10.1103/PhysRevA.86.032324. URL https://link.aps.org/doi/10.1103/PhysRevA.86.032324.

J. Kelly, R. Barends, A. G. Fowler, A. Megrant, E. Jeffrey, T. C. White, D. Sank, J. Y. Mutus, B. Campbell, Yu Chen, Z. Chen, B. Chiaro, A. Dunsworth, I.-C. Hoi, C. Neill, P. J. J. O/'Malley, C. Quintana, P. Roushan, A. Vainsencher, J. Wenner, A. N. Cleland, and John M. Martinis. State preservation by repetitive error detection in a superconducting

quantum circuit. *Nature*, 519(7541):66–69, Mar 2015. ISSN 0028-0836. URL http://dx.doi.org/10.1038/nature14270. Letter.

S. Kirchhoff, T. Keßler, P. J. Liebermann, E. Assémat, S. Machnes, F. Motzoi, and F. K. Wilhelm. Optimized cross-resonance gate for coupled transmon systems. *ArXiv e-prints*, January 2017.

J. Koch, T. M. Yu, J. Gambetta, A. A. Houck, D. I. Schuster, J. Majer, A. Blais, M. H. Devoret, S. M. Girvin, and R. J. Schoelkopf. Charge-insensitive qubit design derived from the cooper pair box. *Phys. Rev. A*, 76:042319, Oct 2007. doi: 10.1103/PhysRevA.76.042319. URL http://link.aps.org/doi/10.1103/PhysRevA.76.042319.

M. Kusunoki, M. Inadomaru, S. Ohshima, K. Aizawa, M. Mukaida, M. Lorenz, and H. Hochmuth. Dielectric loss tangent of sapphire single crystal produced by edge-defined film-fed growth method. *Physica C: Superconductivity*, 377(3): 313 – 318, 2002. ISSN 0921-4534. doi: https://doi.org/10.1016/S0921-4534(01)01282-5. URL http://www.sciencedirect.com/science/article/pii/S0921453401012825.

E. Martin-Lopez, A. Laing, T. Lawson, R. Alvarez, X. Q. Zhou, and Jeremy L. O'Brien. Experimental realization of shor's quantum factoring algorithm using qubit recycling. *Nat Photon*, 6(11):773–776, Nov 2012. ISSN 1749-4885. doi: 10.1038/nphoton.2012.259. URL http://dx.doi.org/10.1038/nphoton.2012.259.

D. C. McKay, S. Filipp, A. Mezzacapo, E. Magesan, J. M. Chow, and J. M. Gambetta. Universal gate for fixed-frequency qubits via a tunable bus. *Phys. Rev. Applied*, 6: 064007, Dec 2016. doi: 10.1103/PhysRevApplied.6.064007. URL https://link.aps.org/doi/10.1103/PhysRevApplied.6.064007.

Z. K. Minev, K. Serniak, I. M. Pop, Z. Leghtas, K. Sliwa, M. Hatridge, L. Frunzio, R. J. Schoelkopf, and M. H. Devoret. Planar multilayer circuit quantum electrodynamics. *Phys Rev Applied*, 5:044021, 2016.

Y. Nakamura, Yu A. Pashkin, and J. S. Tsai. Coherent control of macroscopic quantum states in a single-cooper-pair box. *Nature*, 398(6730):786–788, Apr 1999. ISSN 0028-0836. doi: 10.1038/19718. URL http://dx.doi.org/10.1038/19718.

S. E. Nigg, H. Paik, B. Vlastakis, G. Kirchmair, S. Shankar, L. Frunzio, M. H. Devoret, R. J. Schoelkopf, and S. M. Girvin. Black-box superconducting circuit quantization. *Phys. Rev. Lett.*, 108:240502, Jun 2012. doi: 10.1103/PhysRevLett.108.240502. URL http://link.aps.org/doi/10.1103/PhysRevLett.108.240502.

N. Ofek, A. Petrenko, R. Heeres, P. Reinhold, Z. Leghtas, B. Vlastakis, Y. Liu, L. Frunzio, S. M. Girvin, L. Jiang, M. Mirrahimi, M. H. Devoret, and R. J. Schoelkopf. Extending the lifetime of a quantum bit with error correction in superconducting circuits. *Nature*, 536(7617):441–445, Aug 2016. ISSN 0028-0836. URL http://dx.doi.org/10.1038/nature18949. Letter.

H. Paik, A. Mezzacapo, M. Sandberg, D. T. McClure, B. Abdo, A. D. Córcoles, O. Dial, D. F. Bogorin, B. L. T. Plourde, M. Steffen, A. W. Cross, J. M. Gambetta, and Jerry M. Chow. Experimental demonstration of a resonator-induced phase gate in a multiqubit circuit-qed system. *Phys. Rev. Lett.*, 117:250502, Dec 2016. doi: 10.1103/PhysRevLett.117.250502. URL https://link.aps.org/doi/10.1103/PhysRevLett.117.250502.

Andrew Patterson. *Optimal Control of Supercodnucting Qubits*. PhD thesis, University of Oxford, 2018.

Michael J. Peterer. *Experiments on Multi-Level Superconducting Qubits and Coaxial Circuit QED*. PhD thesis, University of Oxford, 2016.

J. Rahamim, T. Behrle, M. J. Peterer, A. Patterson, P. A. Spring, T. Tsunoda, R. Manenti, G. Tancredi, and P. J. Leek. Double-sided coaxial circuit qed with out-of-plane wiring. *Applied Physics Letters*, 110(22):222602, 2017. doi: 10.1063/1.4984299. URL http://dx.doi.org/10.1063/1.4984299.

Joseph Rahamim. Developing A Coaxial Geometry for Circuit QED. First year report, University of Oxford, 2016.

C. Rigetti and M. Devoret. Fully microwave-tunable universal gates in superconducting qubits with linear couplings and fixed transition frequencies. *Phys. Rev. B*, 81:134507, Apr 2010. doi: 10.1103/PhysRevB.81.134507. URL https://link.aps.org/doi/10.1103/PhysRevB.81.134507.

C. Rigetti, J. M. Gambetta, S. Poletto, B. L. T. Plourde, J. M. Chow, A. D. Córcoles, J. A. Smolin, S. T. Merkel, J. R. Rozen, G. A. Keefe, M. B. Rothwell, M. B. Ketchen, and M. Steffen. Superconducting qubit in a waveguide cavity with a coherence time approaching 0.1 ms. 86(10), sep 2012. doi: 10.1103/PhysRevB.86.100506.

C. Rigetti, J. M. Gambetta, S. Poletto, B. L. T. Plourde, J. M. Chow, A. D. Córcoles, J. A. Smolin, S. T. Merkel, J. R. Rozen, G. A. Keefe, M. B. Rothwell, M. B. Ketchen, and M. Steffen. Superconducting qubit in a waveguide cavity with a coherence time approaching 0.1 ms. *Phys. Rev. B*, 86:100506, Sep 2012. doi: 10.1103/PhysRevB.86.100506. URL https://link.aps.org/doi/10.1103/PhysRevB.86.100506.

Chad Tyler Rigettir. *Quantum Gates for Superconducting Qubits*. PhD thesis, Yale University, 2009.

S. Sheldon, E. Magesan, J. M. Chow, and J. M. Gambetta. Procedure for systematically tuning up cross-talk in the cross-resonance gate. *Phys. Rev. A*, 93:060302, Jun 2016. doi: 10.1103/PhysRevA.93.060302. URL https://link.aps.org/doi/10.1103/PhysRevA.93.060302.

P. W. Shor. Polynomial-Time Algorithms for Prime Factorization and Discrete Logarithms on a Quantum Computer. *SIAM Review*, 41:303–332, January 1999. doi: 10.1137/S0036144598347011.

Mika A. Sillanpaa, J. I. Park, and R. W. Simmonds. Coherent quantum state storage and transfer between two phase qubits via a resonant cavity. *Nature*, 449(7161):438–442,

Sep 2007. ISSN 0028-0836. doi: 10.1038/nature06124. URL http://dx.doi.org/10.1038/nature06124.

T. Simonite. Chemists are first in line for quantum computings benefits. Technical report, MIT Technolgy Review.

Peter Spring. Modelling A Novel Scalable Superconducting Qubit Architecture. Master's thesis, University of Oxford, United Kingdom, 2016.

Kyocera The New Value Frontier. *Single Crystal Sapphire*. 2016. URL http://global.kyocera.com/prdct/fc/product/pdf/s_c_sapphire.pdf.

R. Versluis, S. Poletto, N. Khammassi, N. Haider, D. J. Michalak, A. Bruno, K. Bertels, and L. DiCarlo. Scalable quantum circuit and control for a superconducting surface code. *ArXiv e-prints*, December 2016.

B. C. Wadell. *Transmission Line Design Handbook*. Artech House Microwave Library, 1991.

A. Wallraff, D. I. Schuster, A. Blais, L. Frunzio, R.-S. Huang, J. Majer, S. Kumar, S. M. Girvin, and R. J. Schoelkopf. Strong coupling of a single photon to a superconducting qubit using circuit quantum electrodynamics. *Nature*, 431(7005):162–167, Sep 2004. ISSN 0028-0836. doi: 10.1038/nature02851. URL http://dx.doi.org/10.1038/nature02851.

D. F. Walls and G. J. Milburn. *Quantum Optics*. Springer, 2008.

J. Q. You and F. Nori. Superconducting Circuits and Quantum Information. *Physics Today*, 58(11):42–47, November 2005. doi: 10.1063/1.2155757.

A. M. Zagoskin. *Quantum Engineering: Theory and Design of Quantum Coherent Structures*. Cambridge University Press, 2011.

# Deposition

Ich versichere, dass ich diese Arbeit selbstständig verfasst habe und keine anderen als die angegebenen Quellen und Hilfsmittel benutzt habe.

Oxford, den 7. Juni 2017